Practical Applications of Delta Winglets in Compact Heat Exchangers with Louvered Fins

Michael J. Lawson

Thesis submitted to the faculty of Virginia Polytechnic Institute and State University in partial fulfillment of the requirements for the degree of

Masters of Science
in
Mechanical Engineering

Dr. Karen A. Thole, Chair
Dr. Brian Vick
Dr. Mark Paul

July 19, 2006
Blacksburg, Virginia

Keywords: Louvered Fin, Compact Heat Exchanger, Tube Wall, Vortex Generator, Delta Winglet

Practical Applications of Delta Winglet Vortex Generators in Compact Heat Exchangers with Louvered Fins

Michael Lawson

Thesis Abstract

Compact heat exchangers are widely used by the automotive industry in systems that cool engine components. Louvered fin heat exchangers are used over their continuous fin counterparts because of the significant advantages they provide in heat transfer efficiency, while only causing small increases in overall pressure losses. With the recent emphasis that has been placed on reducing fuel consumption, decreasing the size of the compact heat exchanger has become an important concern. With reduction in size comes not only weight savings, but also a decrease in frontal area in a vehicle that must be dedicated to the heat exchanger, allowing for more aerodynamic vehicle designs.

Air-side resistance on the tube wall and louvered fin surfaces comprises over 85% of total resistance to heat transfer in louvered fin heat exchangers. The tube wall surface is considered the primary surface for heat transfer, where the temperature between the working fluid and convecting air is at a maximum. Recent studies have shown that implementing delta winglets on louvered fins along the tube wall is an effective method of augmenting tube wall heat transfer. In this thesis, the effect of delta winglets is investigated in both two- and three-dimensional louvered fin arrays. For both geometries, winglets are simulated in a manufacturable configuration, where piercings in the louvered fins that would result from the winglet manufacturing process are modeled.

Using the two-dimensional geometry to model tube wall heat transfer was shown not to accurately predict heat transfer coefficients. In a two-dimensional geometry, winglets were found not to be an effective means for augmenting tube wall heat transfer and caused only 8% augmentation. Using the three-dimensional geometry, winglets with simulated piercings were observed to cause up to 24% tube wall heat transfer augmentation, with a corresponding increase in pressure losses of only 10%.

Acknowledgements

I would first like to thank my Mother, Father, and Brother. Only through their love and support was I able to complete this thesis.

There are several people at Virginia Tech I wish to recognize for the support they have given me over the past year. I would like to thank Dr. Karen Thole. She provided me with guidance and counsel through my research, and only through her encouragement was the following work possible. Dr. Thole has taught me about work ethic and the type of dedication that is needed to be successful, I will carry those lessons with me through the rest of my career. Thank you to Dr. Mark Paul and Dr. Brian Vick, although my contact with them relating directly to my research was limited, the instruction they provided in and out of the classroom was invaluable. Their classes drove me to learn and without their efforts the academic gains I made during my masters coursework would not have been possible. I sincerely appreciate everything they have done for me.

To all the members of VTExCCL, I couldn't have asked for a better group to work with. Special thanks go out to Alan, Seth, and Cam, you made this last year fun and I don't know if I would have been able to get through it without you. Jeff, someone had to catch my spelling errors and I know it wasn't going to be me. Thank you for the help, putting up with me, and all the good times. Finally, I have to thank Casey, Justin, and Andrew (in spirit) who gave me an escape from Blacksburg a mere four hours up 81. You guys were always there with support and advice when I needed it most, I can't begin to explain how much that has meant.

Attributions

The following work contains contributions form two other authors. Dr. Karen Thole is the co-author of Chapters 1 and 2. As my advisor, she provided technical advice on the work presented in these chapters. Paul Sanders assisted with Chapter 1 and the appendices by contributing relevant data for comparison.

Table of Contents

Abstract ii
Acknowledgements iii
Attributions iv
List of Figures viii
List of Tables xv

1. Computational and Experimental Comparisons of Tube Wall Heat Transfer Augmented by Winglets in Louvered Fin Heat Exchangers 1
   Abstract 1
   Nomenclature 2
   Introduction 3
   Past Studies of Relevance 4
   Louver and Winglet Geometry 6
   Computational Methodology 7
   Experimental Facilities and Instrumentation 8
   Computational Model Validation 9
   Effects of Winglets without Piercings 10
   Effects of Winglets with Piercings 12
   Conclusions 14
   Acknowledgements 15
   References 15

2. Heat Transfer Augmentation along the Tube Wall of a Compact Louvered Fin Heat Exchanger Using Delta Winglets with Simulated 33
   Abstract 33
   Nomenclature 34
   Introduction 35
   Past Studies of Relevance 36

Louvered Fin Geometry 38
Winglet and Piercing Geometries 39
Experimental Facilities and Instrumentation 40
Data Analysis and Uncertainty 42
Baseline Measurements for Two- and Three-Dimensional Solid Louvered Fins 43
Winglet Augmentations for Two- and Three-Dimensional Solid Louvered Fins 45
Mirrored Winglet Configurations for Three-Dimensional Solid Louvered Fins 46
Winglet Geometry Effects on Three-Dimensional Solid Louvered Fins 48
Effects of Simulated Piercings on Three-Dimensional Louvered Fins 49
Conclusions 51
Acknowledgements 53
References 53

Appendix A Introduction 74
A.1 Nomenclature 75

Appendix B Experimental Facilities and Data Analysis Techniques 78
B.1 Louver Geometry and Modifications 78
B.2 Winglet and Piercing Geometries 79
B.3 Wind Tunnel Design 79
B.4 Test Section Design 80
B.5 Instrumentation 81
B.6 Data Acquisition Hardware and Techniques 82
B.7 Data Reduction 83
B.8 Experimental Uncertainty Estimates 86

Appendix C Additional Experimental Results 99
C.1 Winglet and Piercing Configurations 99
C.2 Baseline Data 100
C.3 Thin Winglet Testing using Solid Louvered Fins 100
C.4 Thick Winglet Testing using Solid Louvered Fins 100

C.5 Pierced Louvered Fin Testing 101
C.6 Best Pierced Louver Winglet Configurations 102

Appendix D Summary of Findings and Recommendations for Future Work 122
D.1 Summary of Findings 122
D.2 Recommendations and Future Work 123

Appendix E References 128

List of Figures

Figure 1.1 Compact louvered fin heat exchanger illustrating the tube-wall juncture 18

Figure 1.2 A delta winglet vortex generator placed along the tube wall. Aspect ratio is defined with respect to b/2 and c..... 19

Figure 1.3 Piercing orientation that would result from the stamping process during manufacturing of the louvers. Louver (a) has the piercing on the suction side where (b) has it on the pressure side 20

Figure 1.4 Louver geometry used for all experimental and computational models showing locations where Nusselt tube wall data was sampled..... 20

Figure 1.5 Illustration of the alternating delta winglet configuration used in the present study. Side, top, and bottom views are shown respectively. The dashed red lines represent lines of symmetry for CFD..... 21

Figure 1.6 Computational domain for the louver array showing the constant heat flux boundary condition on the tube wall..... 21

Figure 1.7 Diagram of experimental facility whereby the tube wall heat transfer measurements were conducted 22

Figure 1.8 (a) – Comparison of experimental and computational results for Nusselt number along $y/F_p = 0.5$ at Re = 230 and 1016 for the baseline geometry (no winglets). (b) – Variations of Nusselt number in the streamwise direction at several different heights along the tube wall for the baseline geometry at Re = 1016..... 23

Figure 1.9 Comparisons of friction factor data for the baseline configuration to that measured by a compact heat exchanger manufacturer on an actual louvered fin heat exchanger..... 24

Figure 1.10 Comparison of measured and predicted Nusselt numbers along $y/F_p = 0.5$ for the baseline and for winglets with a solid louver (no piercings)..... 25

Figure 1.11 Contours of Nusselt number along the tube wall for Re = 230, 615 and 1016, in that order, for the baseline geometry 26

Figure 1.12 Nusselt number augmentation contours at Re = 230, 615, and 1016, in that order, for the (a) solid louvers and (b) pierced louvers..... 26

Figure 1.13 Contours of non-dimensional temperature in regions for observing the effect of winglets angled away from the wall and towards the wall at Re = 1016. (a) – away from the wall, (b) – towards the wall. Louvers 3-6 are shown in order from left to right. Flow is from left to right and the planes are numbered from I-VIII 27

Figure 1.14 Louver 5 and 6 contours of non-dimensional temperature and secondary flow vectors for the solid fin case with winglets angled away from the wall at Re = 1016 28

Figure 1.15 Louver 6 contours of non-dimensional temperature and secondary flow vectors for the solid fin case with winglets angled towards the wall at Re = 1016..... 29

Figure 1.16 Louver 5 and 6 contours of non-dimensional temperature and secondary flow for the baseline at Re = 1016 30

Figure 1.17 Louver 5 and 6 contours of non-dimensional temperature and secondary flow for pierced louvers with winglets angled away from the wall at Re = 1016..... 31

Figure 1.18 Louver 6 contours of non-dimensional temperature and secondary flow for pierced louvers with winglets angled towards the wall at Re = 1016..... 32

Figure 2.1 Louvered fin heat exchanger showing the location of the tube-wall junction 55

Figure 2.2 Diagram of a delta winglet vortex generator 56

Figure 2.3 Actual louvered fin geometry used in testing, (a) – picture of the top view, (b) – side view, and (c) – front view. Note that the fin was molded in two pieces as seen in (a)..... 57

Figure 2.4 (a) – Plexiglas winglet and insert used to simulate piercings and (b) – Cutouts milled into a realistic three-dimensional louvered fin..... 58

Figure 2.5 (a) – Mirrored and (b) – non-mirrored winglet configurations. The red dotted line passing through the turnover louver is the plane across which the winglet setup must be mirrored..... 59

Figure 2.6 Schematic of the open loop wind tunnel used for all experiments 60

Figure 2.7 (a) – Front view, and (b) – isometric view of the test section used. The solid outlined areas indicate the region through which louver directed flow traveled. The dotted outlined areas indicated the region of flows over the flat landings at the edge of the fins. 61

Figure 2.8 Two- and three-dimensional baseline heat transfer results. Also shown are baseline measurements made by Sanders [5] using the same louvered fin geometry. X = 0 corresponds to the entrance of the louvered fin array..... 62

Figure 2.9 Baseline friction factors measured between $0.73L_p$ up and downstream of the louvered fin array compared to a manufacturer's data (Nino [14]) 63

Figure 2.10 Comparison of heat transfer performance using two- and three-dimensional solid louvered fin geometries. $t_w = 0.03t$ for the two-dimensional louvered fins, $t_w = t$ for the three-dimensional louvered fins 64

Figure 2.11 Secondary flow vectors showing a winglet forming a vortex in a two-dimensional louvered fin array. Flow is from left to right following the louver direction 65

Figure 2.12 Comparison of heat transfer performance between non-mirrored and mirrored winglet configurations. Parameters for these tests were: $\alpha = 40°$, $\Lambda = 1.5$, $t_w = t$ using 28 winglets. For the non-mirrored test Z = 0.22, and for the mirrored test Z = 0.15. Note that the winglet setup shown is for the mirrored configuration. 66

Figure 2.13 Nusselt number augmentations along the tube wall for non-mirrored and mirrored winglet configurations at Re = 955. Parameters for the tests were the same as Figure 2.12..... 67

Figure 2.14 Comparison of heat transfer performance between winglets configurations of different aspect ratios. Parameters for the tests were: $\alpha = 40°$, Z = 0.22, $t_w = 0.03t$, using 16 winglets..... 68

Figure 2.15 Comparison of heat transfer performance between winglet configurations having different distances from the tube wall. Parameters for the tests were: $\alpha = 40°$, $\Lambda = 1.5$, $t_w = 0.03t$, using 16 winglets 69

Figure 2.16 Comparison of heat transfer performance between winglet configurations having different winglet thicknesses. Parameters for tests were: $\alpha = 40°$, $\Lambda = 1.5$, $Z = 0.15$, using 16 winglets 70
Figure 2.17 Comparison of heat transfer performance between 28 and 16 winglet configurations. Parameters for the tests were: $\alpha = 40°$, $\Lambda = 1.5$, $Z = 0.15$, and $t_w = t$. Note that the winglet configuration diagram shown is for the 16 winglet configuration 71
Figure 2.18 Comparison of heat transfer performance between pierced and solid fin winglet configurations. Parameters for the tests were: $\alpha = 30°$, $Z = 0.15$, $t_w = t$, using 28 winglets 72
Figure 2.19 Nusselt number augmentations for pierced and solid louvered fin configurations at Re = 955. Parameters for the tests were: $\alpha = 30°$, $Z = 0.15$, $t_w = t$, using 28 winglets 73
Figure A.1 Louvered fin heat exchanger showing the location of the tube-wall junction 77
Figure B.1 Top view, side view, and drawing of realistic molded fin 89
Figure B.2 Louver geometry and definitions used in this study 90
Figure B.3 Comparison of different louver lengths and definitions of louvered fin geometries 90
Figure B.4 Figure B4. Modifications made to (a) – the Ll/Fh = 70% louvered fins, dimensions are measured form the uncut edge of the louvered fin, and (b) – the Ll/Fh = 82% louvered fins, dimensions are measured from the cut edge of the louvered fins 91
Figure B.5 Illustration of a delta winglet vortex generator in the VG-F orientation angled towards the wall with a piercing on the downstream side 92
Figure B.6 The definition of vortex generators placed in the backwards (VG-B) and forwards (VG-F) orientations 93
Figure B.7 Insert for simulating a VG-F winglet with a downstream piercing 93
Figure B.8 Test facility components 94
Figure B.9 Exploded view of the $L_l/F_h = 70\%$ and $L_l/F_h = 82\%$ test section 95
Figure B.10 Custom kapton and inconel constant heat flux heater 95

Figure B.11 L_l/F_h = 70% and L_l/F_h = 82% test section side view showing fin brackets and rubber seals 96
Figure B.12 View of test section inlet showing slots for easy fin removal 96
Figure B.13 Diagrams showing geometric features of the bottom wall and surrounding fins 97
Figure B.14 Diagram of bottom wall side piece additions for converting from L_l/F_h = 70% to L_l/F_h = 82% louver lengths 97
Figure B.15 Diagram showing blocked off channel flow in top wall area 98
Figure B.16 Thermocouple setup for the L_l/F_h = 70% and L_l/F_h = 82% test section 98
Figure C.1 Illustration of a delta winglet vortex generator in the VG-F orientation angled towards the wall with a piercing on the downstream side 106
Figure C.2 The definition of vortex generators placed in the backwards (VG-B) and forwards (VG-F) orientations 107
Figure C.3 (a) – the 28 and (b) the 14 winglet configurations with all winglets angled towards the wall. (c) – the 28 and (d) the 16 winglet configurations with winglets angled towards the wall before the turnover louver and away from the wall after the turnover louver. Note the dark red line represents the heated tube wall and that only configurations (c) and (d) are mirrored 107
Figure C.4 Different winglet placement locations tested: (1) – all winglets on top of the louvered fins, (2) – all winglets on the bottom of the louvered fins, (3) winglets on the top before the turnover louver and on the bottom after the turnover louver, (4) winglets on the bottom before the turnover louver and on the top after the turnover louver, and (5) – winglets alternating between placement on the top and bottom of the louvered fins. Note that only configurations (1), (2), and (5) are mirrored 108
Figure C.5 (a) – Mirrored and (b) – non-mirrored winglet configurations. The red dotted line passing through the turnover louver is the plane across which the winglet setup must be mirrored 108
Figure C.6 Different louvered fin geometries used in this study 109
Figure C.7 Comparison of heat transfer performance between winglets of different aspect ratios using solid louvered fins 110

Figure C.8 Comparison of heat transfer performance between winglets having different distances from the tube wall using solid louvered fins 111
Figure C.9 Comparison of heat transfer performance between non-mirrored and mirrored winglet configurations using solid louvered fins. Note the winglet configuration shown is for the mirrored test..... 112
Figure C.10 Comparison of heat transfer performance between non-mirrored winglets configurations of VG-B and VG-F using solid louvered fins..... 113
Figure C.11 Comparison of heat transfer performance between 28 and 16 winglet configurations using solid louvered fins. Note the winglet configuration is shown for the 16 winglet test..... 114
Figure C.12 Comparison of heat transfer performance between winglet configurations having different winglet thicknesses using solid louvered fins 115
Figure C.13 Comparison of heat transfer performance between pierced and solid fin winglet configurations. Also shown is the comparison of aspect ratio for the pierced louvered fin configurations 116
Figure C.14 Comparison of heat transfer performance between VG-B and VG-F in a mirrored winglet configurations using pierced louvered fins. Note the winglet orientation labeled "VG-B" has VG-B before the turnover louver and VG-F after the turnover louver. The orientation labeled "VG-F" has VG-F before the turnover louver and VG-B after the turnover louver..... 117
Figure C.15 Comparison of heat transfer performance between winglets configurations having different piercing placements. Note that the tests labeled "downstream" had downstream piercings before the turnover louver and upstream piercings after it. The test labeled "upstream" had upstream piercings before the turnover louver and downstream piercings after the turnover louver..... 118
Figure C.16 Comparison of heat transfer performance between winglets configurations having different winglet placements using pierced louvered fins. Note that no winglet configuration diagram is shown because the tests had several different configurations..... 119

Figure C.17 Comparison of heat transfer performance between winglets configurations on fins with different louver lengths using pierced louvered fins 120
Figure C.18 Best mirrored winglet configuration tested with simulated winglet piercings 121
Figure D.1 Secondary flow vectors for the two-dimensional louvered fin case with a winglet angled away from the tube wall. The winglet can be seen forming a vortex, but the vortex breaks as it encounters the next louver in the streamwise direction. Flow is from left to right aligned with the louvers 125
Figure D.2 Best mirrored pierced louvered fin winglet configuration tested using the three-dimensional louvered fins 126
Figure D.3 Recommended non-mirrored pierced louvered fin winglet configuration to augment heat transfer using the three-dimensional louvered fins 127

List of Tables

Table 1.1 Line-Averaged Augmentations of Nusselt Number along y/Fp = 0.5 17
Table 1.2 Area-Averaged Augmentations of Nusselt Number along the Tube Wall 17
Table B.1 Representative Uncertainty Estimates for Calculated Values 88
Table C.1 Experimental Data for all Winglet Configurations Tested 103

Computational and Experimental Comparisons of Tube Wall Heat Transfer Augmented by Winglets in Louvered Fin Heat Exchangers

Michael J. Lawson, Paul A. Sanders, and Karen A. Thole
Mechanical Engineering Department
Virginia Tech
Blacksburg, VA 24061

Abstract

Louvered fins are used in compact heat exchangers to increase heat transfer by interrupting thermal boundary layer growth thereby increasing the convective heat transfer coefficients and reducing the air side resistance. Recently, it has been experimentally shown that heat transfer along the tube wall can be augmented by the placement of delta winglets on the louvers at an angle to the flow.

The focus of this combined experimental and computational study is to determine the effect of realistic winglets on tube wall heat transfer. Comparisons of the computational simulations were made to the experimental results, which were obtained using a twenty times scaled model. Winglet performance characteristics were studied on solid louvers and pierced louvers whereby the latter simulates what would occur for a manufactured louver having a winglet. For a solid louver having a winglet, the tube wall heat transfer augmentation was found to be as high as 5.4%. Pierced louver cases were observed to produce slightly higher heat transfer augmentations than solid louver cases. Computational results suggest that the mechanism behind tube wall heat transfer augmentation is flow redirection and not winglet induced vortices.

Nomenclature

A	Heater surface area
b	Two times winglet height
c	Winglet chord
C_p	Specific heat of air
f_o	Baseline Fanning friction factor with no winglets
F_d	Fin depth
F_p	Fin pitch
h	Convection coefficient, $h = q''/(T_w - T_{in})$
k	Thermal conductivity
L_p	Louver pitch
$\dot{m}$	Mass flow through the louver array
Nu	Nusselt number, $Nu = h\ L_p / k$
Nu_o	Baseline Nusselt number
q''	Convective heat flux at heated wall
Re	Reynolds number based on louver pitch, $Re = U_{ff} L_p/\nu$
t	Louver thickness
T_b	Bulk temperature at entrance to specific louver, $T_b = T_{in} + q''A(x)/\dot{m}C_p$
T_w	Temperature measured on heated wall
U_{ff}	Maximum free flow velocity
U_{in}	Inlet velocity
x	Streamwise coordinate through the louver array
X	Non-dimensional fin depth, $X = x/F_d$

Greek symbols

α	Winglet angle of attack
Λ	Delta winglet aspect ratio, $\Lambda = 2b/c$
θ	Non dimensional fluid temperature, $\theta = (T - T_{in})/(T_b - T_{in})$
θ_L	Louver angle
ΔP	Pressure drop through louvered array
ρ_{air}	Density of air
ν	Kinematic viscosity

Introduction

In the automotive industry, louvered fins are used to reduce the size and weight of the compact heat exchanger (radiator) while ensuring the required heat transfer occurs for the engine. A louvered fin heat exchanger typical of those used in automotive applications is shown in Figure 1.1. Over 85% of the thermal resistance to heat transfer is on the air-side and for this reason most research has been aimed at determining methods to reduce air-side resistance. This research has primarily entailed optimizing the geometric parameters of current louver designs to promote convective heat transfer. To date, little work has been published on new methods for augmenting heat transfer along the tube wall of the compact heat exchanger; however, the tube wall is considered the primary surface where the temperature difference from the bulk air temperature and the tube wall is at its maximum.

There are three primary mechanisms influencing heat transfer along the louvered surfaces: (1) the quality of louver directed flow [1.1 and 1.2], (2) the continual initiation of the thermal boundary layer resulting from the louver interruptions [1.3], and (3) the intensity of vorticity near the louvered fins [1.4]. Given that these mechanisms have been shown to have a positive effect on heat transfer along the louver surface, it would be expected that if these same conditions could be induced along the tube wall, augmentations of convective heat transfer would be possible. A recent experimental study published by Sanders and Thole [1.5] demonstrates that it is possible to increase tube wall heat transfer augmentation by altering the juncture geometry between the louvered fin and the tube wall. The alteration consists of delta winglets (shown in Figure 1.2) placed on the louver surface at an angle to the flow near the tube wall. As of yet, the specific mechanism behind the observed increase in tube wall heat transfer is undetermined.

Louvered fins are generally manufactured using a stamping process whereby the fin is made from one large sheet of sheet metal. It is expected that a louvered fin heat exchanger implementing delta winglets would have winglets with the same thickness as the louvers along with voids or piercings where the winglets were stamped into the finned surface. Figure 1.3 illustrates where piercings would be left during the stamping process. Note that the work previously presented by Sanders and Thole [1.5] did not experimentally simulate the piercings but rather simulated solid louvers with delta winglets.

To determine whether the implementation of winglets in a practical manner still provides augmentations in tube wall heat transfer, two different winglet cases were studied. For the first case, winglets having a thickness of the louver were placed on solid louvers, using the same technique as described by Sanders and Thole [1.5]. For the second case, the same winglet geometry was used only with simulated piercings. For this second case, the piercings were placed in the louvers at locations that would result from the stamping process. This paper outlines the experimental and computational methods used to study the effects of winglets and simulated piercings on tube wall heat transfer and the near wall flow field in a compact louvered fin heat exchanger.

Past Studies of Relevance

For several decades, compact heat exchangers with louvered fins, as shown in Figure 1.1, have been used over continuous fins because they provide a substantial advantage in heat transfer, with acceptable increases in pressure losses. Beauvais [1.6] was one of the first to show that louvers redirect the flow in the direction of the louvers. Prior to Beauvais' work, it had been thought that louvers provided heat transfer increases by disrupting duct directed flow. Much of the published research has been aimed at determining the optimal geometry for louvered fins in order to most effectively reduce air-side resistance (see Chang et al. [1.7 and 1.8] and Kays and London [1.9]).

Three-dimensional effects resulting from the louver-tube wall junction were studied by Atkinson et al. [1.10] who performed computational studies of two- and three-dimensional louvered fin arrays. Three-dimensional geometries, whereby the louver-tube wall juncture was modeled, indicated lower heat transfer than the corresponding two-dimensional geometries which ignored edge effects from the tube wall. Tafti and Cui's [1.11] computational study agreed with the results of Atkinson et al. [1.10]. In addition, Tafti and Cui [1.11] demonstrated that the cause of the lower observed heat transfer in the three-dimensional junctures was due to the thick thermal boundary layer present on the tube wall.

It has been established that delta wings and winglets (delta winglet shown in Figure 1.2) placed on a flat surface increase surface heat transfer by forming streamwise vortices. Gentry and Jacobi [1.12] placed delta wings on a flat plate and measured increases in heat transfer between 20% and 50% at Reynolds numbers (based on hydraulic diameter) ranging between 400

and 2000. Circulation and heat transfer were observed to increase with angle of attack (α), aspect ratio (Λ) and Reynolds number. In a continuation of this work, Joardar and Jacobi [1.13] implemented delta wings at the inlet to a louvered fin heat exchanger. Approximately 1500 delta wings were placed along the leading edge of the entrance louvers of an actual heat exchanger. Increases in heat transfer for wet and dry conditions were found to be 21% and 23%, respectively, while the maximum increase in aerodynamic losses was only 6%.

Sanders and Thole [1.5] tested the effects of triangular delta winglets placed on the louvers along the tube wall over the length of the louver array. Delta winglets are not to be confused with delta wings. While both are vortex generators that cause the formation of streamwise vortices, the geometries are significantly different. Sanders and Thole [1.5] found that delta winglets resulted in augmentations that were as high as 35% for heat transfer accompanied by augmentations of 13% for pressure drop. It is important to note that these high augmentations were measured using very thin winglets that were not representative of what would be stamped from louvered fins. Their study also reported that using winglets matching the thickness of the louvers resulted in much lower augmentations (Sanders [1.14]). The work reported in this paper is for a winglet thickness that would be consistent with the manufacturing process.

As previously noted, louvered fin heat exchangers are manufactured using a stamping process. If delta wings or winglets are introduced into current heat exchanger designs there will be piercings that will remain where the winglets were stamped out as shown in Figure 1.3. One of the few studies that looked at the effect delta winglets with piercings have on heat transfer is that of Vasudevan et al. [1.15]. The effect of delta winglets with and without piercings on heat transfer was simulated for a parallel plate heat exchanger with triangular channels, which is significantly different than the geometry studied in our paper. Vasudevan et al. [1.15] computationally predicted that the length of a continuous fin in a compact heat exchanger could be reduced by up to 20% while maintaining the same overall heat transfer rate through the use of delta winglets. When the heat transfer performances of channels with and without piercings were compared, piercings were shown to only have a small negative effect on overall heat transfer.

Data presented in the literature clearly indicates that heat transfer augmentation results from the use of winglets in a louvered fin compact heat exchanger. There is however, a need to

understand the mechanism that causes augmentation of tube wall heat transfer using realistic winglets with piercings. This paper is a continuation of the work of Sanders and Thole [1.5] where a realistic winglet geometry resulting from the manufacturing processes has been considered.

Louver and Winglet Geometry

The louver geometry used was the same as that considered in studies by Sanders and Thole [1.5] and Ebeling and Thole[1.16]. The louver geometry had a louver angle of $\theta_L = 27^\circ$, a fin pitch over louver pitch of $F_p/L_p = 0.76$, and louver thickness over louver pitch of $t/L_p = 0.079$. The louver pattern was composed of an entrance louver followed by seven louvers leading to the turnover louver, as shown in Figure 1.4. Following the turnover louver there are seven more streamwise louvers prior to the exit louver. For the computational and experimental simulations, the louvered fin was simulated by considering a louver that spanned the entire width of the heat exchanger with a 90 degree juncture between the louver and tube wall.

The delta winglet design used for this study was chosen based on experimental work by Sanders and Thole [1.5]. The winglet setup is presented in Figure 1.5 and consists of delta winglets placed in a backward-facing (tall end of the triangular winglet facing upstream) configuration. Delta winglet direction was alternated between winglets angled towards and away from the wall, starting with the first winglet being angled towards the wall. For the pierced case, piercings were placed on the suction side (downstream side) of winglets angled towards the wall and placed on the pressure side (upstream side) of winglets angled away from the wall. This choice was made to keep the pierced section of the louver as far away from the tube wall as possible to maximize the thermal contact with the tube wall. All winglets had an aspect ratio of $\Lambda = 1.5$ with an angle of attack of $\alpha = 40^\circ$ and were placed at a distance from the tube wall of $0.15L_p$.

Two different variations of the winglet setup described above were tested: (1) winglets placed on the louvers as described with no simulated piercings; and (2) winglets placed on the louvers with simulated piercings (shown in Figure 1.3) that would result from winglet stamping in the manufacturing process. These two winglet setups will be referred to as solid louver cases and pierced louver cases. For comparison and validation purposes a baseline case with no winglets was also simulated.

Computational Methodology

Three-dimensional simulations using computational fluid dynamics (CFD) were performed using the commercial code Fluent (version 6.2.16). Fluent uses a pressure-based solver that can be used with unstructured meshes. The solution is obtained by solving incompressible equations for continuity, momentum, and energy. Flow through the louver array was assumed to be laminar and steady up to the highest tested Reynolds number tested of 1016. This assumption has been shown to be valid by Kajino et al. [1.17]. Approximately 750 iterations were required for convergence, the solution was judged to be converged when the residuals were four orders of magnitude below that which occurred initially.

Meshes were generated using Gambit and consisted of between three and six million cells depending on the complexity of the geometry being simulated. The baseline case had the simplest and smallest mesh while the louvers with the piercings had the largest mesh. Mesh quality was checked by evaluating element skewness, for all meshes the skewness was less than the maximum allowable for use with the Fluent solver. To be sure the mesh accurately captured all important physics, grid adaptation based on velocity and temperature gradients was performed in Fluent. The grid was refined through adaptations and increasing mesh size. The grid was considered insensitive as the mesh size was increased by 30% resulting in less than a 1.5% difference in area averaged heat transfer.

The computational domain, shown in Figure 1.6, extended from the tube wall to the centerline of the louver array. The entire louver array is simulated by applying a symmetry boundary condition across the plane at the centerline of the array. Assuming that the flow was pitch-wise periodic, only one row of louvers was simulated. Velocity boundary conditions were set at the inlet to the domain, which was three louver pitches upstream of the entrance louver, while an outflow boundary condition was set at the exit, which was 6.5 pitches downstream of the last louver (Ebeling and Thole [1.16]). Louvers and the tube wall surface were set with no slip boundary conditions. To accurately represent the experimental conditions of Sanders and Thole [1.5], louver junctures at the wall were assumed to be adiabatic surfaces ($q'' = 0$). The tube wall itself was given a constant heat flux boundary condition spanning from the entrance to the exit louvers.

Experimental Facilities and Instrumentation

All tests were carried out in a twenty times scaled version of a louvered fin heat exchanger. Figure 1.7 shows the test facility used in this study, which was an open loop wind tunnel consisting of an inlet nozzle, a test section, a laminar flow element, and a motor-controlled blower. All of the major components in the test facility were the same used in the studies of Lyman et al. [1.18], Stephan and Thole [1.19], and Ebeling and Thole [1.16], with the exception of the actual test section which was modified to account for the heat transfer measurements. The contraction, which had a 16:1 area reduction, was designed to provide a uniform inlet flow to the test section,. Air was pulled through the test rig with a 1.5 hp motor powering the centrifugal fan, which was controlled with an AC inverter. Flow rates through the test section were measured by the laminar flow element.

The test section was composed of the bounded flow path through the louvered fin array, an instrumented heated wall, and a conduction guard heater assembly. The top and bottom walls bounding the flow path replicated the louver angles to simulate louver directed flow. The test section simulated 12 louver rows, which based on studies by Springer and Thole [1.20] was adequate to model an infinite stack of louvers.

The instrumented wall, which had a constant heat flux boundary condition, simulated the tube wall of a heat exchanger. It was constructed from strip heaters arranged in series that were adhered to a sheet of lexan. A guard heater was placed behind the lexan to minimize any conduction losses from the heated wall. Current through the heater circuit was measured along with the heater resistance and surface area to calculate the surface heat flux. Thermocouples embedded in the lexan directly behind the heater were used to measure wall temperatures, thereby allowing for convective heat transfer coefficients to be calculated. Losses due to radiation from the heater were also accounted for when calculating the resulting convective heat flux.

To compare the increases in frictional losses caused by the winglets, pressure drop measurements were made across the louver array. These pressure losses were converted to Fanning friction factors. Losses due to the sudden contraction and expansion associated with the air entering and leaving the finned array were accounted for.

The uncertainty estimates of Nusselt numbers, Reynolds numbers, and friction factors were calculated using the method described by Moffat [1.21], which are based on the chain rule of differentiation. Uncertainties in Nusselt numbers for the majority of the louvered array were 4.4% at Re = 230 and were 2.8% at Re = 1016. Higher values occurred at the first louver position, but as stated above, these values were not used in augmentation calculations. Uncertainties in the baseline friction factor for Re=230 were a high 51%, due to the very low pressure differences, and were 8.2% at Re = 1016.

Computational Model Validation

To validate the computational simulations, comparisons were made to the experimentally measured baseline results for a louver array without winglets. Figure 1.8a shows the experimentally measured and computationally predicted tube wall Nusselt numbers mid-way between two louver passages ($y/F_p = 0.5$ in Figure 1.4). Note that the experimental data is a discrete representation as single thermocouples were used while the computational data is continuous. The data given in Figure 1.8a is plotted against non-dimensional streamwise distance normalized by the fin depth for Re = 230 and 1016. Figure 1.8a shows relatively good agreement between the measured and predicted values with a maximum difference between the predicted and measured of 5.3% for Re = 615.

As shown by previous experiments and as Figure 1.8a indicates, there is a strong Reynolds number influence on the alignment of the flow with the louvers. While the Re = 230 data indicates what one might predict for a channel flow with little augmentation resulting from the entrance and turnover louvers, the Re = 1016 data indicates large augmentations at the entrance and turnover regions. Streamlines verify that flow is better aligned at the higher Reynolds number. The sudden direction change for Re = 1016 at the turnover coupled with the high flow momentum results in larger augmentations than for Re = 230. At Re = 230 the relative momentum of the fluid is much less and causes the flow to be less sensitive to the sudden direction change at the turnover louver.

Figure 1.8b presents Nusselt number predictions for Re = 1016 at different positions along the tube wall relative to the louvers. These relative positions are shown in Figure 1.4. In Figure 1.8b, the predictions indicated large variations in the Nusselt numbers at $y/F_p = 0.72$ in the upstream half of the louver array and at $y/F_p = 0.28$ in the downstream half of the louver

array. The high Nusselt number peaks for $y/F_p = 0.28$ and 0.72 correspond to the locations where the boundary layer along the wall is disrupted by the louvers.

Comparisons were also made between experimentally measured pressure drops and those predicted using CFD. As an additional check, data measured by a compact heat exchanger manufacturer was also compared to both CFD and experimental data sets (Nino [22]). It is important to note that the data provided by the manufacturer is for an actual louvered fin heat exchanger having the same louver geometry, but additionally having a flat transitional landing between the tube wall and the louver. As seen in Figure 1.9, there is good agreement between all three data sets over a range of Reynolds numbers.

Effects of Winglets without Piercings

Sanders and Thole [1.5] measured the winglet performance based on Nusselt number augmentations over the baseline without any winglets along $y/F_p = 0.5$ for the solid louver case. Similarly, Figure 1.10 shows the Nusselt data at Re = 230 and 1016 along $y/F_p = 0.5$ for both experimental and computational results. Winglets are seen to increase the heat transfer coefficient before the transition; however, starting with the turnover louver, little if any augmentation is indicated.

Table 1.1 presents the augmentations based on the single streamwise line averages along $y/F_p = 0.5$. Note that the augmentations for the CFD results are based on the CFD predictions for the baseline, while the experimental augmentations use the experimental baseline. Results from CFD and experiments agreed reasonably well and showed augmentations predicted to be as high as 5.13% for Re = 615 (CFD data). As was shown in Figure 1.8b, there are strong variations in the Nusselt numbers at different pitchwise locations on the tube wall. The Nusselt numbers calculated along $y/F_p = 0.5$ represents a fraction of the data that determines the overall heat transfer coefficient on the tube wall.

To be complete in evaluating the performance of the winglets, the predicted data for the solid louver was used to calculate area averages over the entire tube wall, these averages are reported in Table 1.2. As the data in Table 1.2 indicates, the area-average augmentations are higher than the line averages calculated along $y/F_p = 0.5$. The maximum area-averaged augmentation was 5.36% at Re = 615 and was minimum at Re = 230 having a value of 2.99%.

Overall, winglets having a thickness that is the same as the louver placed on a solid fin do augment the overall tube wall heat transfer. To better understand the causes of this augmentation, spatially-resolved contour maps of the tube wall Nusselt numbers for the baseline were generated and are shown in Figure 1.11. These contours can be compared with Nusselt number augmentation contours for the solid louver with winglets in Figure 1.12a. Figure 1.12a clearly illustrates that winglets augment the heat transfer between louvers 2-8 and 13-16 (louver numbers correspond to those shown in Figure 1.5). These increases in heat transfer, however, are offset by the large decrease in heat transfer indicated at the turnover louver that continues downstream to louver 12.

In Figure 1.12a, louvers before the turnover have the winglet located on the top of the louver resulting in high Nusselt augmentations along the top surface. After the turnover louver, where the winglets are on the bottom of the louver, augmentations are seen along the bottom surface. Winglets facing away from the wall (louvers 3, 4, 7, 11, 13, 15) are observed to cause higher augmentations than winglets facing towards the wall. The highest augmentations were observed at streamwise locations corresponding to where the winglets were placed on the louvers rather than being located further downstream.

Originally, it was believed that the winglets caused vortices which were augmenting the heat transfer. These contour results however indicate that winglets facing away from the wall are causing more augmentation than those angled towards the wall. To observe the effect that winglets were having on the near tube wall flow field, several planes between louvers 3 and 6 were analyzed and are shown in Figure 1.13. In Figure 1.13 the heated wall has been removed from view to allow for the louvers to be seen. Note that the tube wall would be located against the louvers on the side closest to the winglets. These planes were chosen to observe the effect of winglets because they are sufficiently far enough downstream of the entrance louver so that the flow is louver-aligned and effects of the turnover are not yet felt by the flow. Streamlines were used to verify flow alignment with the louvers in these planes. Figure 1.13 shows contours of the non-dimensional thermal field overlaid with the secondary flow (off-axis) vectors in the planes of interest.

To better see the flowfield effects illustrated in Figure 1.13 for the Re = 1016 case, Figures 1.14 and 1.15 provide expanded views of the flowfield. For comparison purposes Figure 1.16 shows the same view as Figure 1.14 only for the baseline with no winglets. Figures 1.14

and 1.15 clearly show vortices forming as the flow on the pressure side of the winglets at planes III and VI rolls over the winglets and begins to circulate. The formed vortex begins to cause hot air to be drawn away from the tube wall and towards the cooler center flow by plane IV in Figure 1.14 and VII in Figure 1.15. In plane V and VIII however, the vortices are disrupted by the leading edge of the downstream louver before the vortices can appreciably dilute the tube wall thermal boundary layer. Neither of the vortices is observed to propagate more than $0.75L_p$ downstream before being disrupted.

As mentioned above, winglets angled away from the wall have a greater effect on heat transfer augmentation than winglets angled towards the wall. It is evident from observation of plane III in Figure 1.14 and comparing it to the gradients at that same plane in Figure 1.16 that the large velocity gradient near the wall caused by the winglet results in increasing the heat transfer augmentation. In fact, as the heat transfer augmentation contour in Figure 1.12b illustrates, there is little if any augmentation in the regions where the vortices are present. The highest augmentation occurs in the region where the flow is disturbed by the winglet.

Figures 1.14 and 1.15 also give an indication as to why winglets angled towards the wall have little effect on heat transfer augmentation. Winglets angled away from the wall (Figure 1.14) produce high velocity gradients near the wall at the large end of the delta winglet. Winglets angled towards the wall (Figure 1.15) do not result in such high velocity gradients near the wall resulting less heat transfer augmentation.

To summarize, the secondary flow vectors and temperature contours of Figures 1.14 and 1.15 indicate that the vortices that are formed by the delta winglets are disrupted before there can be a significant effect on the thermal boundary layer along the tube wall. Most of the heat transfer augmentation seen in the regions near the winglets is attributed to a flow redirection.

Effects of Winglets with Piercings

The performance with winglets having piercings in the louvers was evaluated using the same methods as in the previous section with solid louvers. Area-averaged augmentation values, shown in Table 1.2, indicate slightly larger Nusselt number augmentations across all Reynolds numbers compared to solid louver cases. Maximum area-averaged augmentation levels occur at Re = 615 with increases of 2.28% over the same solid fin case and 7.64% over the baseline. The minimum augmentation over the baseline occurs at Re = 230 and is 3.86%

Nusselt number augmentation contours given in Figure 1.12b indicate that higher augmentations for the winglets occur with the presence of piercings particularly at locations where the winglets are angled away from the wall. This increased augmentation due to the effects of the piercings does not result in a significantly larger overall Nusselt number augmentation because the large positive augmentations at the winglet locations is negated by an even stronger decreased heat transfer region starting at the turnover louver and continuing downstream to louver 12.

Figures 1.17 and 1.18 show the same planes of secondary flow vectors and temperature contours as Figures 1.14 and 1.15 for the pierced louver cases. Comparing the pierced to solid louver, there is increased flow mixing for the pierced louver case. Note that the winglet angled away from the wall has the piercing on the pressure side as shown in Figure 1.3. Planes IV in Figures 1.14 and 1.17 indicate that the piercing present in Figure 1.17 has little effect on the strength of the vortex formed. Although some ingestion into the piercing from the pressure side of the winglet (seen in plane III of Figure 1.17) does take place, the negative effects of this on vortex formation appear to be minimal. While the pressure side piercing causes no noticeable effects on vortex formation, the winglet angled towards the wall with the piercing on the suction side is unable to form a vortex because of ingestion into the piercing. Air from the underside of the louver can be seen flowing upwards through the piercing in plane VI in Figure 1.18. This strong ingestion does not allow the air rolling over the top of the pressure side of the winglet to form a vortex and no vortex is present at plane VII for the pierced louver as there is for the solid louver case.

While no vortex forms for winglets angled towards the wall in the pierced fin case, the thermal fields show that this lack of vortex formation does not have an adverse effect on heat transfer. To the contrary, this lack of vortex formation enhances the amount of mixing that occurs along the tube wall in the immediate vicinity of the winglet as illustrated by the differences in planes V and VI of Figures 1.15 and 1.18. These results are also consistent in stating that it is not the vortex formation that causes increased heat transfer augmentation, but rather, it is a redirection of the flow.

Conclusions

Winglets placed on louvers along the tube wall were shown to augment the heat transfer along the tube wall both with and without piercings implemented into the louvers. For the solid louver case, the maximum measured area-averaged augmentation was 5.36% at a Reynolds number of 615. Nusselt number augmentations resulting from winglet effects were observed to be locally as high as 100% near the winglet for a winglet angled away from the wall. These high augmentations occurred at locations where no vortex had yet formed. Strong velocity gradients that resulted from flow redirection in this area suggested that large augmentations were caused by this mechanism rather than by vortex formation or propagation. Consistent with this finding was that winglets angled towards the wall showed little increase in heat transfer because the large edge of the triangular winglet that caused most flow redirection was too far from the tube wall for the effects to be felt along the wall.

Louvers with piercings produced augmentation of 7.64% at Re = 615 which was higher that the case with solid louvers. Piercings on the pressure side of the winglet angled towards the wall did not affect the formation of vortices and little difference was seen between the vortices formed in the pierced and solid louver cases. The piercings increased local augmentations because they caused stronger nearwall flow disturbances. Winglets angled towards the wall had their piercings on the suction side, which caused air ingestion that disrupted vortex formation. Because augmentation was not caused by vortices, the lack of vortex formation did not decrease heat transfer.

In conclusion, winglets placed on the louvers were shown to cause small Nusselt number augmentation along the tube wall. Winglets caused a complex flowfield where the effects of each winglet and piercing influence the function of downstream winglets and the overall flow field through the heat exchanger. High local augmentation levels seen along the tube wall due to winglet and piercing effects did not translate into a large increase in area-averaged heat transfer because of negative downstream winglet effects. It was also identified that the primary flow mechanism altering tube wall heat transfer was the redirection of the flow rather than effects of vortices that were formed.

Acknowledgements

The authors would like to acknowledge the support of Modine Manufacturing, Inc for their support on this project. In particular the authors would like to thank Drs. Victor Nino and Steve Memory who have generously provided technical feedback.

References

[1.1] Achaichia, A. and Cowell, T. A., 1988, "Heat Transfer and Pressure Drop Characteristics of Flat Tube and Louvered Plate Fin Surfaces," *Experimental Thermal and Fluid Sciences* vol. 1, pp. 147-157.

[1.2] Webb, R. L. and Trauger, P., 1991, "Flow Structures in Louvered Fin Heat Exchanger Geometry," *Experimental Thermal and Fluid Science*, vol. 4, pp.205-214.

[1.3] Zhang, X. and Tafti, D. K., 2001, "Classification and Effects of Thermal Wakes on Heat Transfer in Multilouvered Fins," *International Journal of Heat and Mass Transfer*, vol. 44, pp. 2461–2473.

[1.4] Tafti, D. K. and Zhang, X., 2001, "Geometry Effects on Flow Transition in Multilouvered Fins - Onset, Propagation, and Characteristic Frequencies," *International Journal of Heat and Mass Transfer,* vol. 44, pp. 4195–4210.

[1.5] Sanders, P. and Thole, K. A., 2006, "Effects of Winglets to Augment Tube Wall Heat Transfer in Louvered Fin Heat Exchangers," *International Journal of Heat and Mass Transfer*, (in press).

[1.6] Beauvais, F. N., 1965, "An Aerodynamic Look at Automotive Radiators," SAE Paper No. 650470.

[1.7] Yu-Juei Chang, Kuei-Chang Hsu, Yur-Tsai Lin, Chi-Chuan Wang, 2000, "A Generalized Friction Correlation for Louver Fin Geometry," *International Journal of Heat and Mass Transfer*, vol. 43, pp. 2237-2243.

[1.8] Yu-Juei Chang and Chi-Chuan Wang, 1997, "A Generalized Heat Transfer Correlation for Louver Fin Geometry," *International Journal of Heat and Mass Transfer*, vol. 40, pp. 533-544.

[1.9] Kays, W. M. and London, A. L., *Compact Heat Exchangers*, 2nd ed., McGraw-Hill, New York, 1984.

[1.10] Atkinson, K. N., Draulic, R., Heikal, M. R., Cowell, T. A., 1998, "Two- and Three-Dimensional Numerical Models of Flow and Heat Transfer Over Louvered Fin Arrays in

Compact Heat Exchangers," *International Journal of Heat and Mass Transfer*, vol. 41, pp. 4063-4080.
[1.11] Tafti, D. K. and Cui, J., 2003, "Fin–tube Junction Effects on Flow and Heat Transfer in Flat Tube Multilouvered Heat Exchangers," *International Journal of Heat and Mass Transfer*, vol. 46, pp. 2027-2038.

[1.12] Gentry, M. C. and Jacobi, A. M., 2002, "Heat Transfer Enhancement by Delta-Wing-Generated Tip Vortices in Flat Plate and Developing Channel Flows," *International Journal of Heat and Mass Transfer*, vol. 124, pp. 1158-1168.

[1.13] Joardar, A., and Jacobi, A. M., 2005 "Impact of Leading Edge Delta-Wing Vortex Generators on the Thermal Performance of a Flat Tube," Louvered Fin Heat Exchanger," *International Journal of Heat and Mass Transfer*, vol. 48, pp. 1480-1493.

[1.14] Sanders P., "Effects of Louver Length and Vortex Generators to Augment Tube Wall Heat Transfer in Louvered Fin Heat Exchangers", 2005, MSME Thesis, Virginia Tech.

[1.15] Vasudevan, R., Eswaran, V., Biswas, G., 2000, "Winglet-Type Vortex Generators for Plate Fin Heat Exchangers Using Triangular Fins," *Numerical Heat Transfer*, vol. 58 , pp. 533-555.

[1.16] Ebeling, C., and Thole, K. A., 2004, "Measurements and Predictions of the Heat Transfer at the Tube-Fin Junction for Louvered Fin Heat Exchangers," *International Journal of Compact Heat Exchangers*, vol. 5, pp. 265-286.

[1.17] Kajino, M., Hiramatsu, M., Yang, W.J., Mori, T., "Research and Development of Automotive Heat Exchangers, *Heat Transfer in High Technology and Power Engineering*, Hemisphere, Washington, DC, 1987, pp. 420-432.

[1.18] Lyman, A. C., Stephan, R. A., Thole, K. A., Zhang, L., Memory, S., 2002, "Scaling of Heat Transfer Coefficients Along Louvered Fins," *Experimental Thermal Fluid Science*, vol. 26, pp. 547-563.

[1.19] Stephan, R. A., and Thole, K. A., 2005, "Optimization Study Relevant to Louvered Fin Heat Exchangers," *International Journal of Heat Exchangers*, vol. 6, pp. 73-92.

[1.20] Springer, M. E., and Thole, K. A., 1998, "Experimental Design for Flowfield Studies of Louvered Fins," *Experimental Thermal and Fluid Science*, vol. 18, pp. 258-269.

[1.21] Moffat, R. J., 1988, "What's New in Convective Heat Transfer," *International Journal of Heal and Fluid Flow,* vol. 19, pp90-101.

[1.22] Nino, V. G., 2006, Personal communication through Modine Manufacturing.

Table 1.1. Line-Averaged Augmentations of Nusselt Number Along $y/F_p = 0.5$

Re	Louver setup	CFD $\overline{\mathbf{Nu}}$	CFD $\frac{\overline{Nu}}{Nu_o}-1$	Exp. $\overline{\mathbf{Nu}}$	Exp. $\frac{\overline{Nu}}{Nu_o}-1$
230	baseline	3.29	-	3.23	-
	solid fin	3.39	2.98%	3.07	-6.49%
	pierced fin	3.42	3.90%	-	-
615	baseline	5.89	-	5.36	-
	solid fin	6.19	5.13%	5.62	4.70%
	pierced fin	6.32	7.28%	-	-
1016	baseline	8.25	-	7.34	-
	solid fin	8.49	2.94%	7.48	1.84%
	pierced fin	8.54	3.53%	-	-

Table 1.2. Area-Averaged Augmentations of Nusselt Number Along the Tube Wall

Re	Louver setup	$\overline{\overline{\mathbf{Nu}}}$	$\frac{\overline{\overline{Nu}}}{Nu_o}-1$
230	baseline	3.56	-
	solid fin	3.66	2.99%
	pierced fin	3.70	3.86%
615	baseline	6.40	-
	solid fin	6.74	5.36%
	pierced fin	6.88	7.64%
1016	baseline	8.98	-
	solid fin	9.33	3.92%
	pierced fin	9.41	4.79%

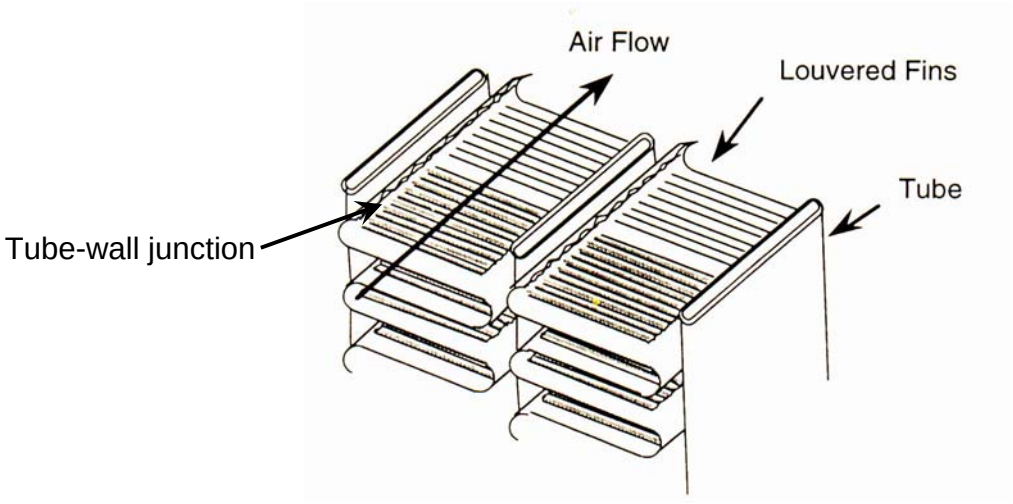

Figure 1.1. Compact louvered fin heat exchanger illustrating the tube-wall juncture.

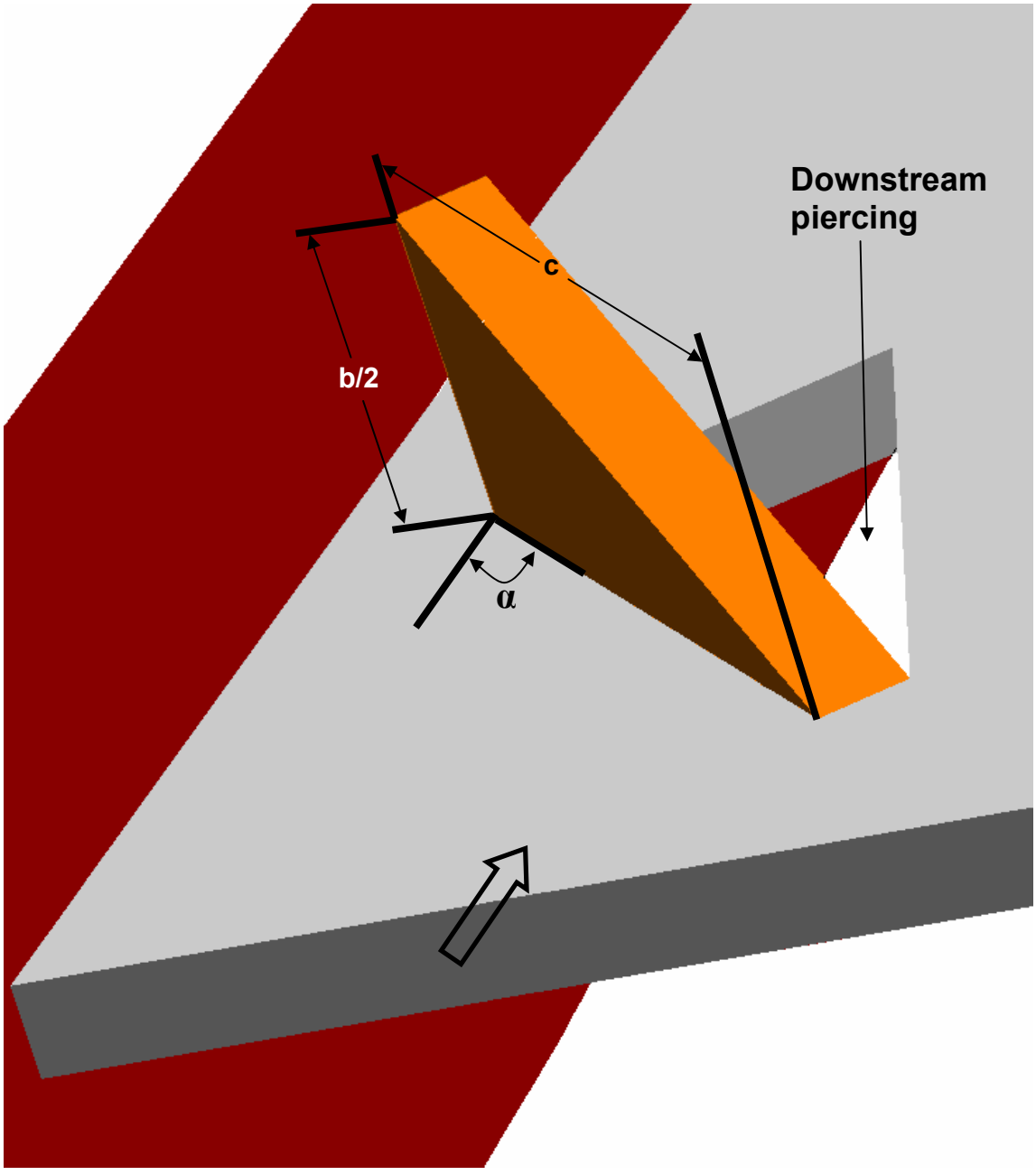

Figure 1.2. A delta winglet vortex generator placed along the tube wall. Aspect ratio is defined with respect to b/2 and c.

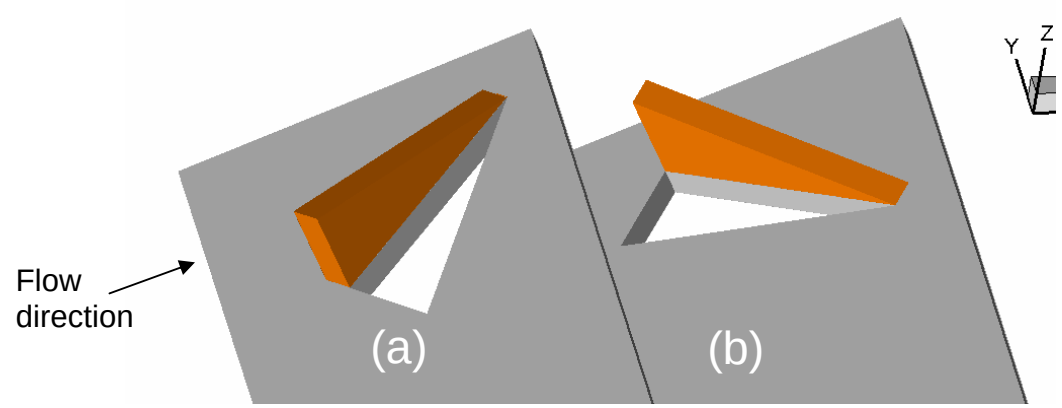

Figure 1.3. Piercing orientation that would result from the stamping process during manufacturing of the louvers. Louver (a) has the piercing on the suction side where (b) has it on the pressure side.

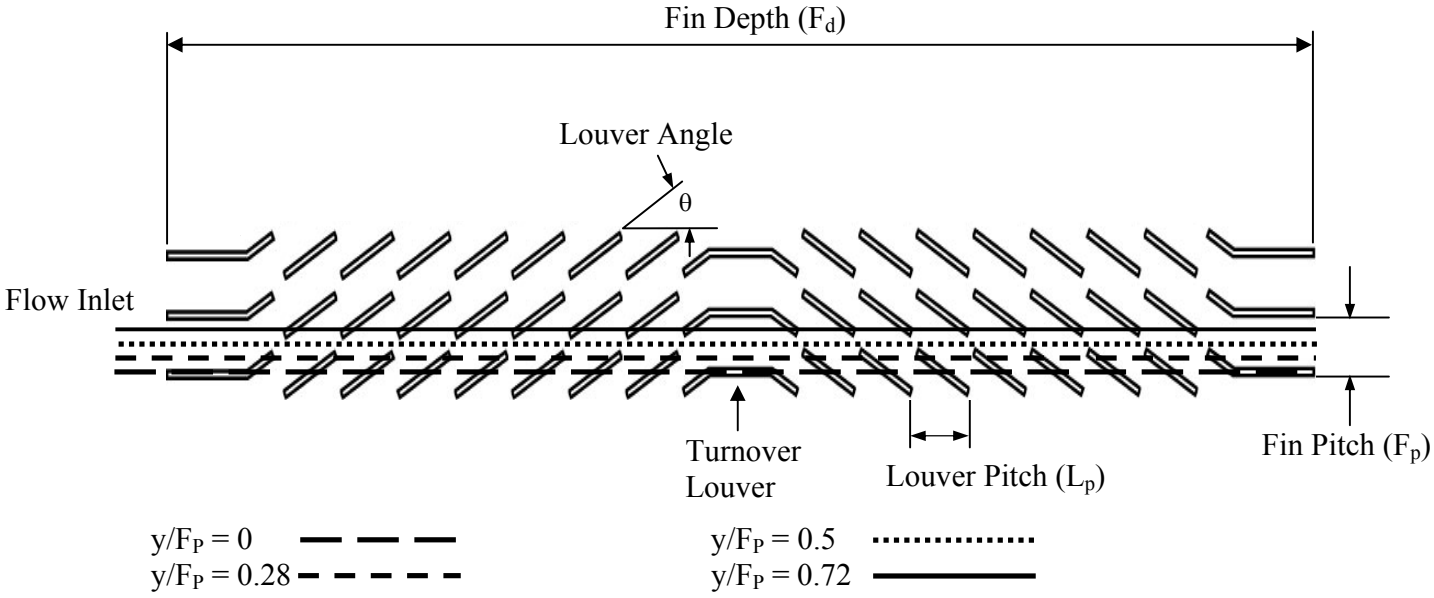

Figure 1.4. Louver geometry used for all experimental and computational models showing locations where Nusselt tube wall data was sampled.

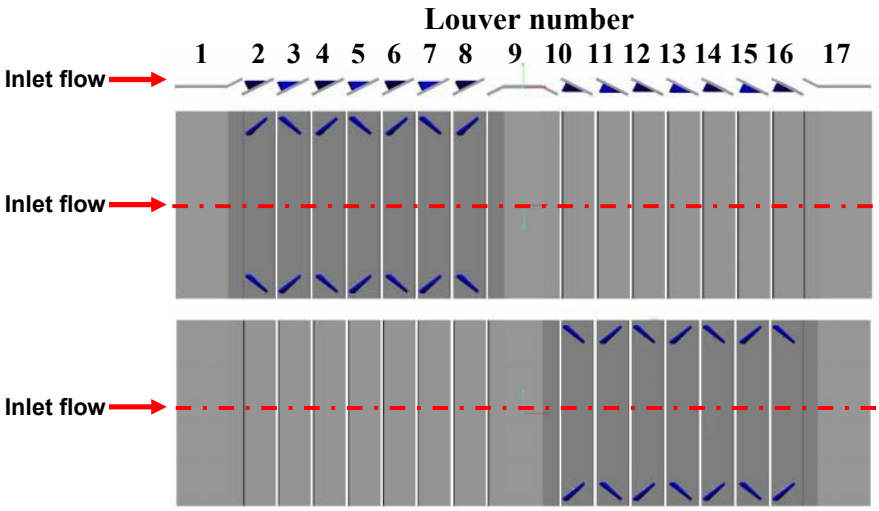

Figure 1.5. Illustration of the alternating delta winglet configuration used in the present study. Side, top, and bottom views are shown respectively. The dashed red lines represent lines of symmetry for CFD.

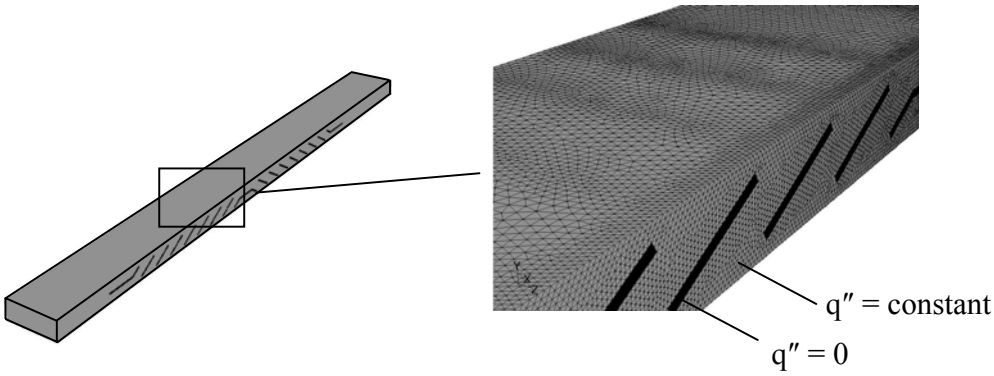

Figure 1.6. Computational domain for the louver array showing the constant heat flux boundary condition on the tube wall.

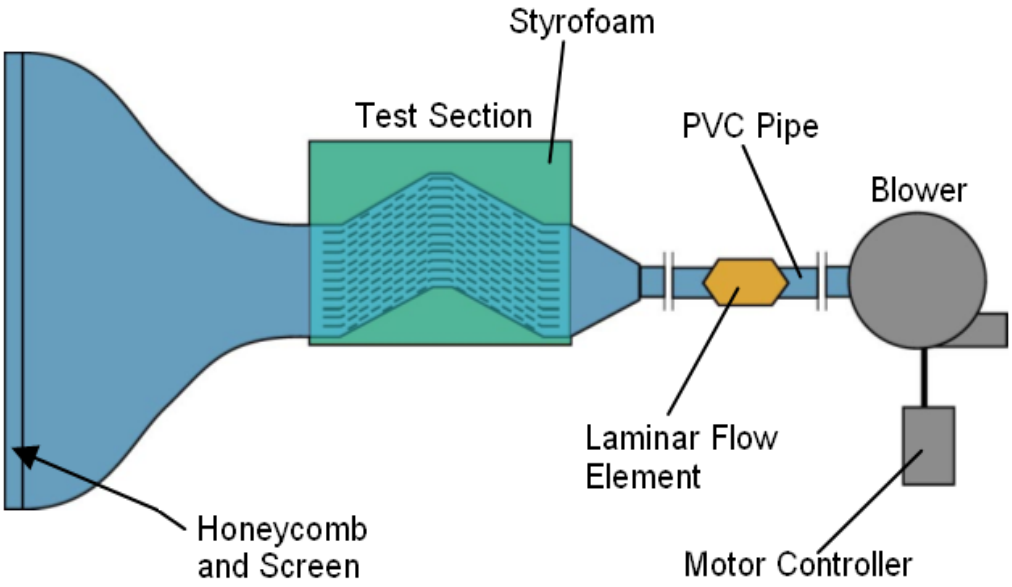

Figure 1.7. Diagram of experimental facility whereby the tube wall heat transfer measurements were conducted.

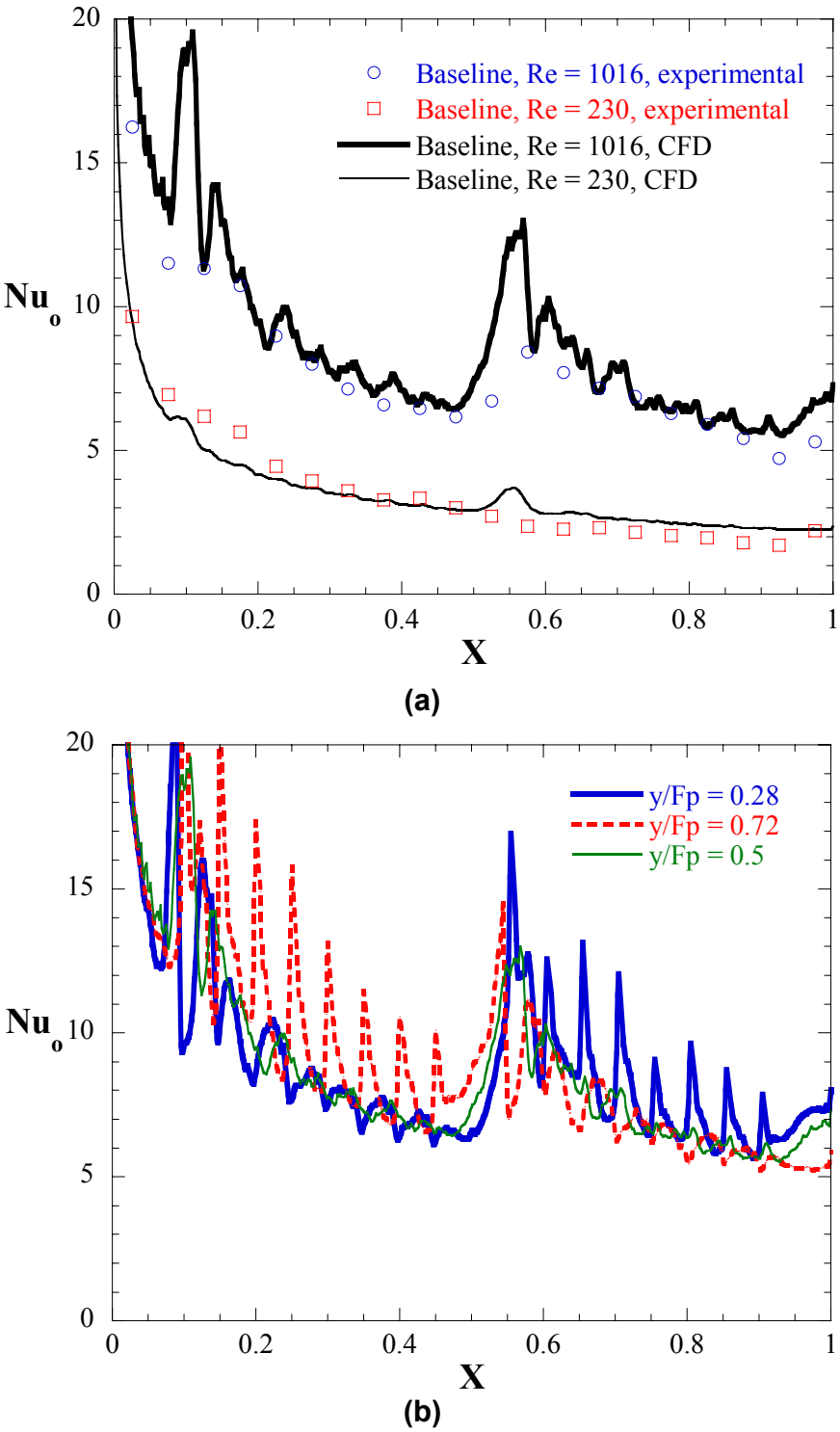

Figure 1.8. (a) – Comparison of experimental and computational results for Nusselt number along $y/F_p = 0.5$ at Re = 230 and 1016 for the baseline geometry (no winglets). (b) – Variations of Nusselt number in the streamwise direction at several different heights along the tube wall for the baseline geometry at Re = 1016.

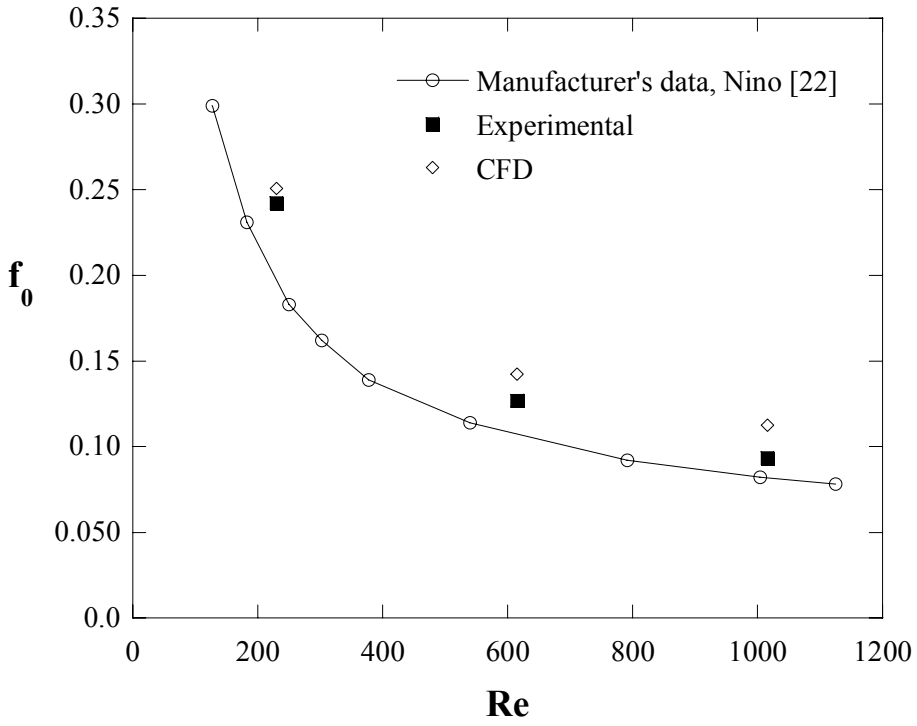

Figure 1.9. Comparisons of friction factor data for the baseline configuration to that measured by a compact heat exchanger manufacturer on an actual louvered fin heat exchanger.

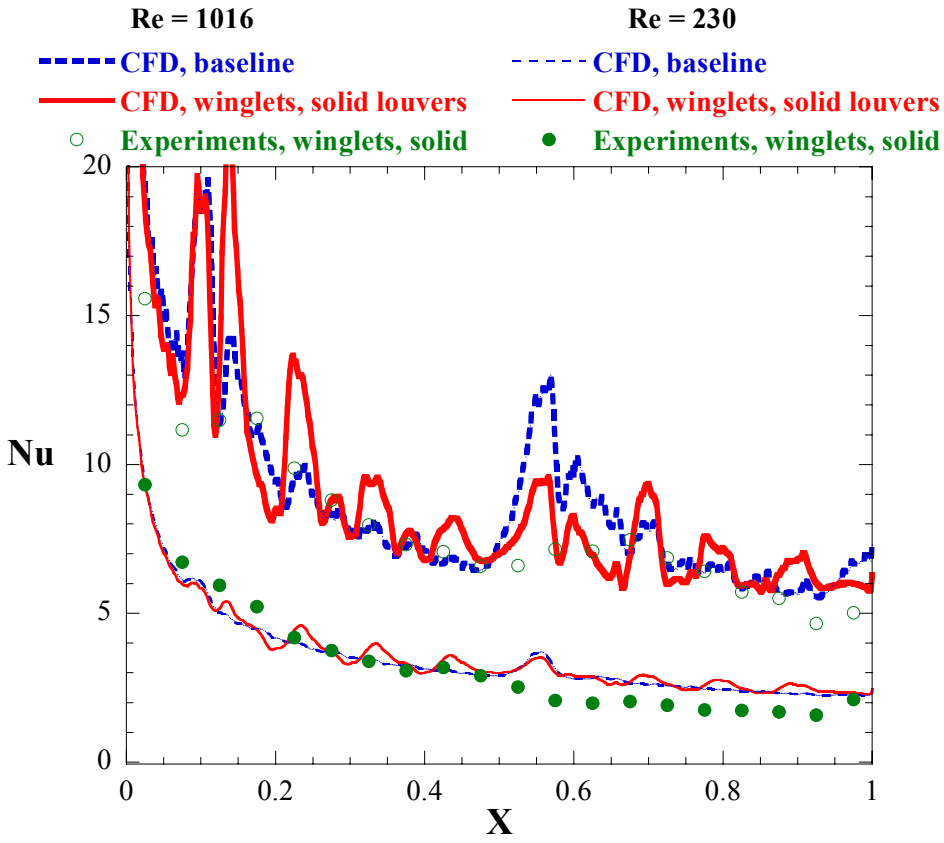

Figure 1.10. Comparison of measured and predicted Nusselt numbers along $y/F_p = 0.5$ for the baseline and for winglets with a solid louver (no piercings).

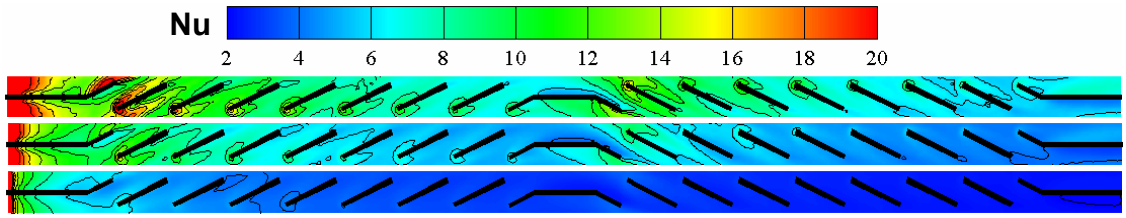

Figure 1.11. Contours of Nusselt number along the tube wall for Re = 230, 615 and 1016, in that order, for the baseline geometry.

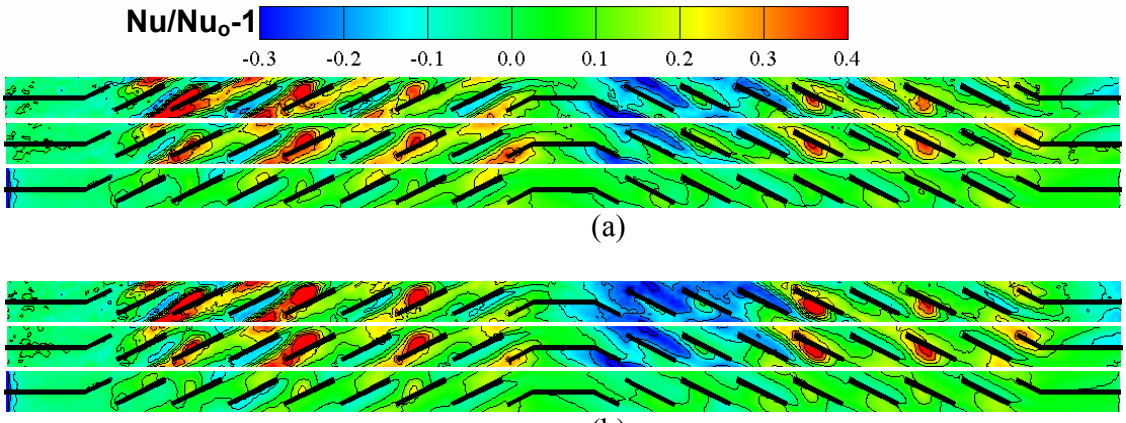

(a)

(b)

Figure 1.12. Nusselt number augmentation contours at Re = 230, 615, and 1016, in that order, for the (a) solid louvers and (b) pierced louvers.

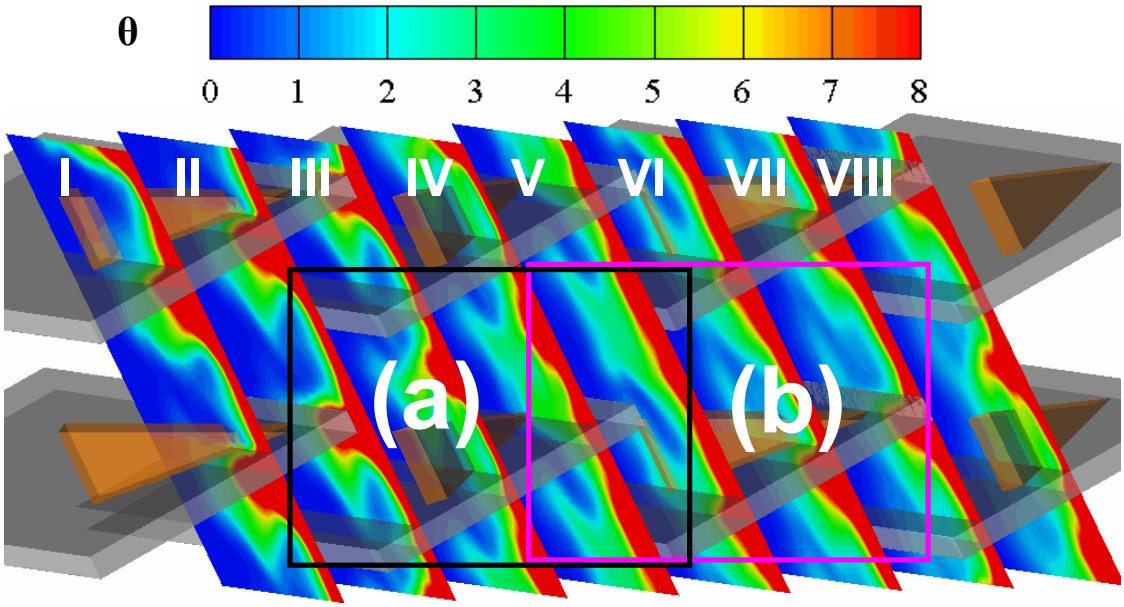

Figure 1.13. Contours of non-dimensional temperature in regions for observing the effect of winglets angled away from the wall and towards the wall at Re = 1016. (a) – away from the wall, (b) – towards the wall. Louvers 3-6 are shown in order from left to right. Flow is from left to right and the planes are numbered from I-VIII.

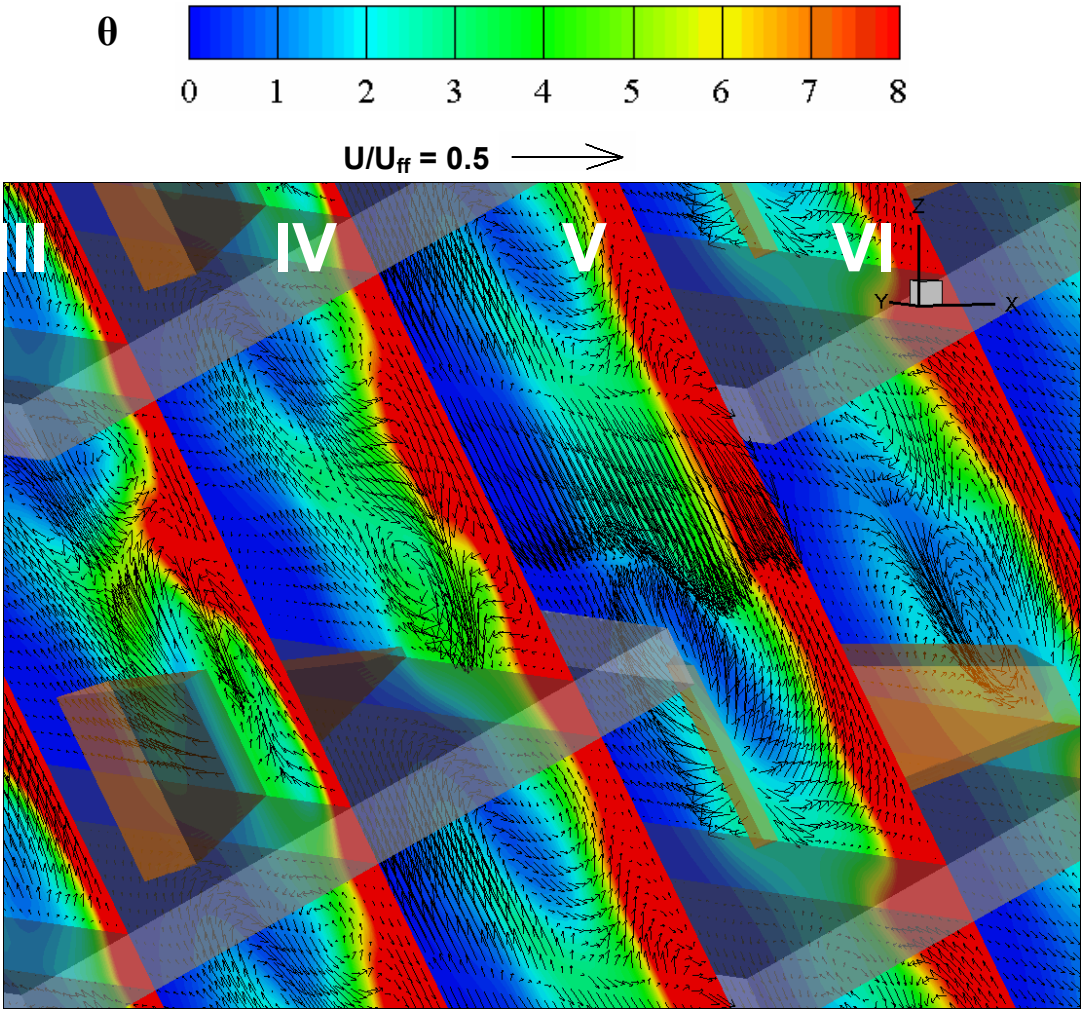

Figure 1.14. Louver 5 and 6 contours of non-dimensional temperature and secondary flow vectors for the solid fin case with winglets angled away from the wall at Re = 1016.

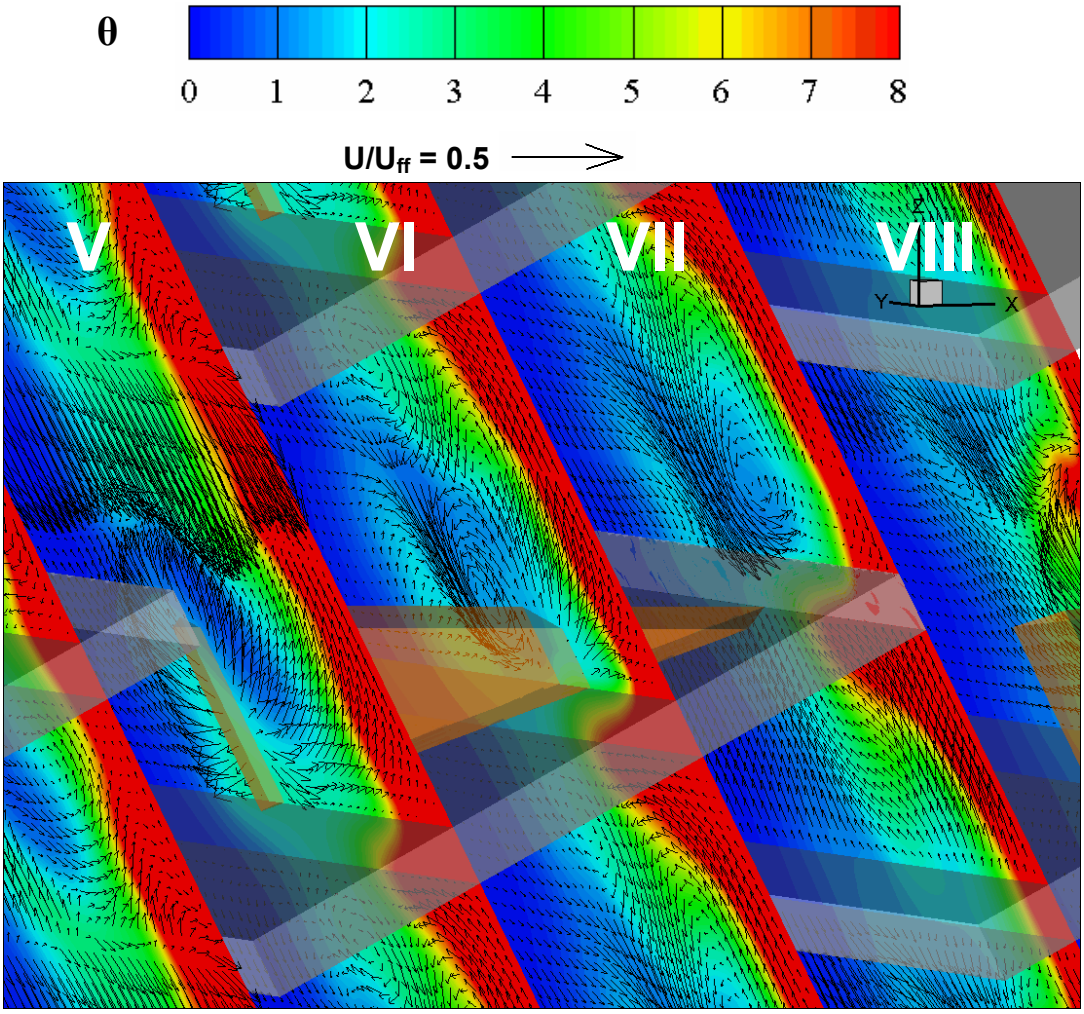

Figure 1.15. Louver 6 contours of non-dimensional temperature and secondary flow vectors for the solid fin case with winglets angled towards the wall at Re = 1016.

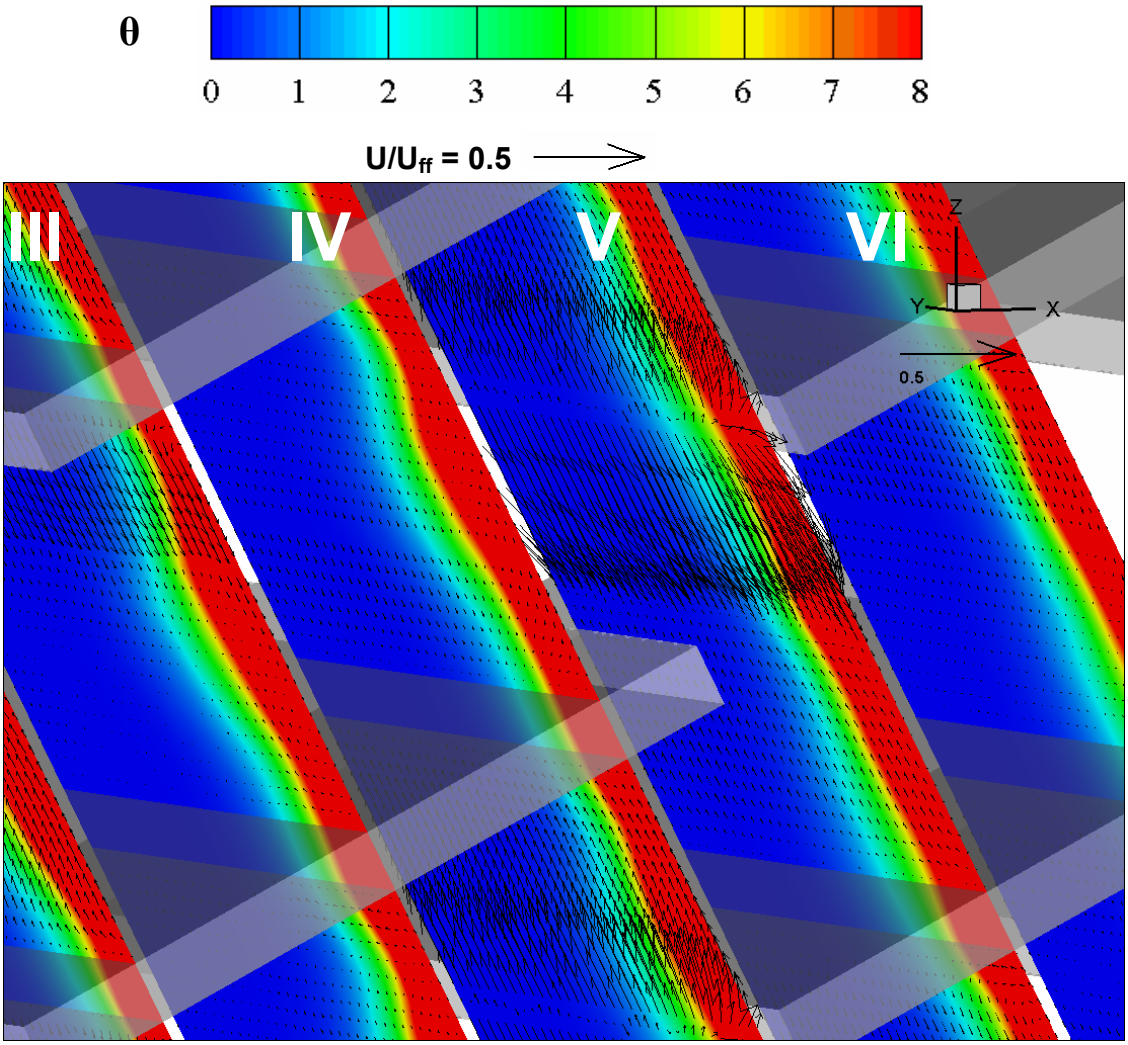

Figure 1.16. Louver 5 and 6 contours of non-dimensional temperature and secondary flow for the baseline at Re = 1016.

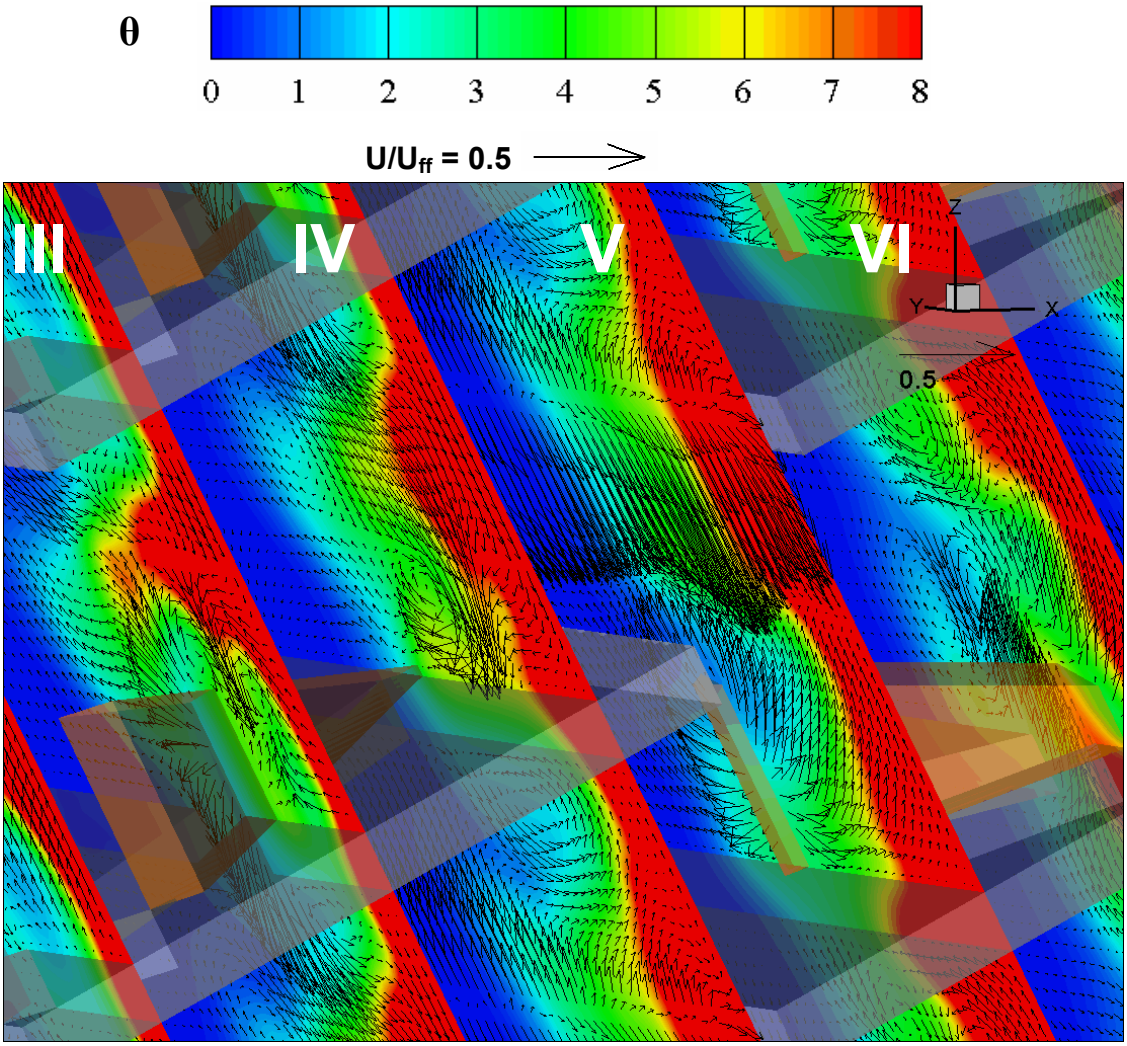

Figure 1.17. Louver 5 and 6 contours of non-dimensional temperature and secondary flow for pierced louvers with winglets angled away from the wall at Re = 1016.

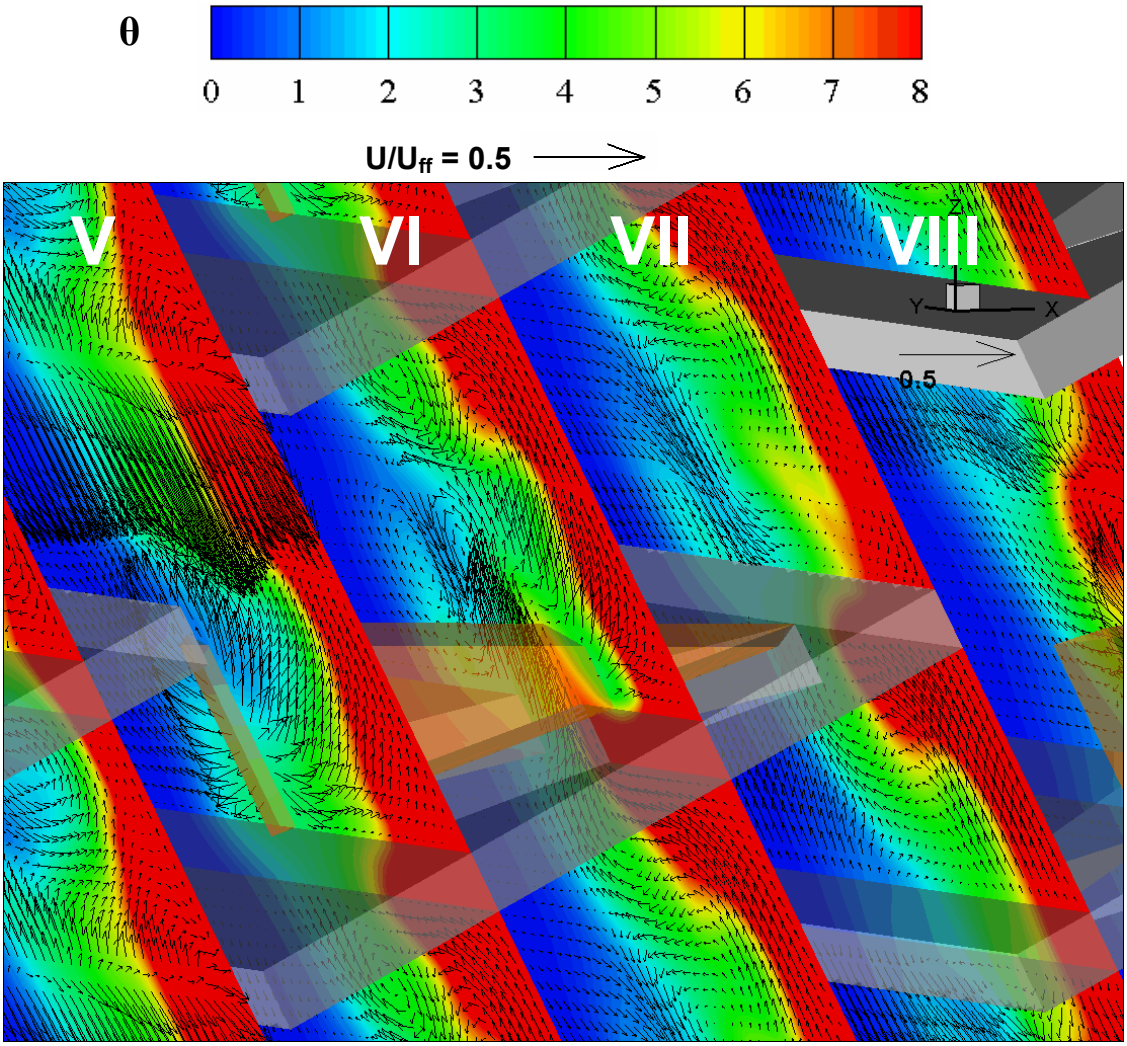

Figure 1.18. Louver 6 contours of non-dimensional temperature and secondary flow for pierced louvers with winglets angled towards the wall at Re = 1016.

Heat Transfer Augmentation along the Tube Wall of a Compact Louvered Fin Heat Exchanger Using Delta Winglets with Simulated Piercings

Michael J. Lawson and Karen A. Thole
Mechanical Engineering Department
Virginia Tech
Blacksburg, VA 24061

Abstract

Delta winglets are known to induce the formation of streamwise vortices and increase heat transfer between the working fluid and the surface on which the winglets are placed. This study investigates the use of delta winglets to augment heat transfer on the tube wall surface of compact louvered fin heat exchangers. In this study it is shown that delta winglets placed on three-dimensional louvered fins produce augmentations in heat transfer along the tube wall as high as 47% with a corresponding increase of 19% in pressure losses. Augmentations were caused primarily by vortices that swept along the tube wall. Manufacturing constraints were also considered in this study whereby piercings in louvered fins and manufacturable winglet configuration were simulated. Considering manufacturing constraints were shown to reduce average heat transfer augmentation, but significant heat transfer increases were still measured with respect to the baseline.

Nomenclature

b	Two times winglet height
c	Winglet chord
D_H	Hydraulic diameter
f	Fanning friction factor
f_o	Baseline Fanning friction factor
F_d	Fin depth
F_h	Fin height
F_p	Fin pitch
h	Convection coefficient, $h = (q''_{total} - q''_{cond} - q''_{rad})/(T_w - T_{in})$
k_{air}	Thermal conductivity of air
K_c	Loss coefficient for sudden contraction of flow entering louvered array
K_e	Loss coefficient for sudden expansion of flow leaving louvered array
L_l	Louver length
L_p	Louver pitch
Nu	Nusselt number, $Nu = h L_p / k$
Nu_o	Baseline Nusselt number
q''_{cond}	Heat flux lost by conduction through instrumented wall
q''_{total}	Applied heat flux at heated wall
q''_{rad}	Heat flux lost by radiation from the heated wall
Re	Reynolds number based on louver pitch, $Re = U_{ff} L_p/\nu$
t	Louver thickness
t_w	Winglet thickness
T_{inlet}	Temperature measured at test section inlet
T_w	Temperature measured on the heated tube wall
U	Local velocity
U_{ff}	Mass averaged velocity through the louvered fin array
x	Streamwise coordinate through the louver array
X	Non-dimensional fin depth, $X = x/F_d$
z	Distance of delta winglet from the tube wall
Z	Non-dimensional distance of delta winglet from the tube wall, $Z = z/L_p$

Greek symbols

α	Winglet angle of attack
Λ	Delta winglet aspect ratio, $\Lambda = 2b/c$
θ_L	Louver angle
ΔP	Pressure drop through louvered array
ρ_{air}	Density of air
ν	Kinematic viscosity of air

Introduction

In the automotive industry, decreasing the size of compact heat exchangers is of great importance for fuel economy. Advantages to decreasing heat exchanger size include weight savings, as well as a decrease in the required frontal area of a vehicle that must be dedicated to the heat exchanger. Louvered fin heat exchangers are commonly used over continuous fin designs in automotive applications because of the substantial advantages they provide in heat transfer performance, while causing acceptable increases in pressure losses. Increases in efficiency allow for louvered fin heat exchangers to be smaller and lighter, while providing the same heat transfer capacity. Figure 2.1 shows a compact louvered fin heat exchanger typical of those used by the automotive industry.

Louvers increase heat transfer by disrupting thermal boundary formation, causing a significant decrease in airside thermal resistance, which comprises 85% of overall resistance to heat transfer. There have been several studies, summarized by Chang et al. [2.1 and 2.2], that have attempted to determine an optimal louver pattern to maximize heat transfer. However, to date there has been little research performed that investigates the possibility of fundamentally altering the louvered fin geometry to improve heat transfer on the tube wall surface.

Recent studies by Lawson et al. [2.3], Sanders and Thole [2.4], and Sanders [2.5] have identified one possible alteration that may be a practical means for improving louvered fin heat exchanger performance is the implementation of delta winglets, shown in Figure 2.2, into louvered fin geometry. Louvered fins are manufactured using a stamping process whereby a modification to the geometry would also be stamped out of the same sheet of metal from which the fins are made. Louvered fins that incorporate winglets into their design would therefore have piercings in locations where the winglets were stamped.

Lawson et al. [2.3] and Sanders and Thole [2.4] performed experimental and computational investigations into the effect that winglets had with and without simulated piercing on the tube wall heat transfer. Lawson et al. [2.3] and Sanders and Thole [2.4] used a two-dimensional louvered fin geometry where the louver surface spanned the entire heat exchanger core. Winglets with a thickness of the louvers were shown to have only a small positive effect on heat transfer. Incorporating piercings into the louvered fins was shown to slightly increase heat transfer compared to tests without piercings; however, the maximum winglet augmentation of tube wall heat transfer observed was only 8%.

Sanders [2.5] also tested three-dimensional louvered fins with several different winglet geometries and measured heat transfer augmentation as high as 53% along the tube wall with only a 21% increase in pressure losses. The three-dimensional louvered fin geometry included the transition between the louvers and the flat landing abutting the tube wall. Sanders [2.5] however did not model the winglet piercings that would be left from the manufacturing process.

Currently, no studies have been performed incorporating winglets with simulated piercings into a three-dimensional, louvered fin geometry. As will be discussed in the next section, past studies have shown that measurements of tube wall heat transfer made using a two-dimensional louvered fin geometry do not agree with those made using a realistic three-dimensional geometry. Although Lawson et al. [2.3] have simulated delta winglets with piercings, their results can not be used to make direct inferences about winglet performance in a heat exchanger with a three-dimensional louvered fin geometry as they only modeled a two-dimensional louvered fin. This paper continues the work of Lawson et al. [2.3] and Sanders and Thole [2.4] by examining the effect of winglets and piercings on tube wall heat transfer for a three-dimensional, manufacturable louvered fin geometry.

Past Studies of Relevance

The majority of research on louvered fin heat exchangers has attempted to determine an optimal geometry for the louvers. Beauvais [2.6] was one of the first to perform an investigation of louvered fin heat exchangers. He found that louvers not only disturb the flow through the louver array, but also cause the flow to be redirected in the louver direction. Davenport [2.7] built upon the understanding of louver effects by suggesting that the mechanism by which louvers increase heat transfer performance is the breaking and reforming of the thermal boundary layer. It has since been accepted that this disruption of thermal boundary layer growth is the mechanism by which louvers decrease overall air-side resistance to heat transfer.

Since the work of Davenport [2.7], most experimental and computational studies have focused on the overall heat transfer performance of louvered fin heat exchangers. Achaicha and Cowell [2.8] comprehensively showed the effect of different heat exchanger geometries on heat transfer and flow alignment with the louvers. Geometric parameters investigated included louver pitch, louver angle, and fin pitch, as shown in Figure 2.3. Achaicha and Cowell [2.8] observed that heat transfer performance increased as the flow became more louver-aligned.

Aided by advances in the ability to model complex geometries computationally, detailed performance characteristics of heat exchangers have been studied through the use of CDF. Atkinson et al. [2.9] modeled two- and three-dimensional louvered fin arrays. They found that accounting for the three-dimensionality of the flow field more accurately matched published experimental results. Tafti and Cui [2.10] performed a computational study that investigated four different geometries for the transition between louvers and the tube wall. Tafti and Cui [2.10] found that for a realistic three-dimensional transition geometry, away from the tube wall the flow is mostly two-dimensional, while near the tube wall in the transition region flow is highly three-dimensional. Poor agreement was observed between the two- and three-dimensional models for the transition. Tafti and Cui's [2.10] work showed that accounting for three-dimensional effects will produce different heat transfer results than results obtained using a two-dimensional model. In their paper, Tafti and Cui [2.10] suggest that if a method of augmenting tube wall heat transfer can be determined, there is potential for large improvements in overall heat transfer performance. It has been shown by Sanders and Thole [2.4] that delta winglets, shown in Figure 2.2, are one means of augmenting tube wall heat transfer.

Delta winglets placed at an angle to a flow are known to create streamwise vortices. Biswas et al. [2.11] studied the effect of delta winglets on heat transfer over a flat plate. Augmentations as high as 65% augmentation were measured on the plate surface. Biswas et al. [2.11] concluded that delta winglets show significant promise for improving the heat transfer performance of heat exchangers. Gentry and Jacobi [2.12] studied the effect of delta wing vortex generators placed in developing channel flow and on flat plates. Delta wings are not to be confused with delta winglets. While both induce streamwise vortices, the geometries are slightly different. Using delta wings, Gentry and Jacobi [2.12] measured increases in average channel heat transfer of up to 55% between Reynolds numbers (with respect to channel hydraulic diameter) of 400 and 2000. Interestingly, Gentry and Jacobi's [2.12] results suggested that vortex strength, and not the location with respect to the channel boundary layer, was the most important factor in enhancing convective effects in the boundary layer. Biswas et al [2.11] and Gentry and Jacobi [2.12] identified that winglet performance and vortex strength improved with increasing angle of attack and Reynolds number.

One of the only studies that investigated the effect of delta winglets, including simulated piercings, on heat transfer in heat exchangers was that of Vasudevan et al. [2.13]. This

computational study modeled delta winglets, both with and without simulated piercings, placed in triangular duct flow. Vasudevan et al. [2.13] predicted that through the use of delta winglets, the required length of a triangular duct heat exchanger could be significantly reduced, possibly by as much as 20%, while maintaining the same heat transfer to the working fluid. It was found that implementing piercings caused both a more complex flow in the channel and some negative effect on overall winglet performance. High augmentations were still observed with piercings and Vasudevan et al. [2.13] concluded that winglets with piercings are a practical method of augmenting heat transfer performance.

This paper is a continuation of the work of Lawson et al. [2.3], Sanders and Thole [2.4], and Sanders [2.5]. The information contained within this paper reports on the investigation of varying winglet and piercing geometries on heat transfer and pressure drop performance using a three-dimensional louvered fin geometry as shown in Figure 2.3. Sanders and Thole [2.4] were the first to consider the possibility of implementing delta winglets along the tube wall surface of a louvered fin heat exchanger. The tube wall is considered the primary surface for heat transfer where the temperature difference between the free stream air and the tube wall is at its maximum. The work of Sanders and Thole [2.4] was performed using a two-dimensional heat exchanger geometry where the louvers spanned the width of the test section. Tube wall heat transfer augmentation over the baseline case with no winglets was as high as 35%, with pressure loss penalties of only 13%. Sanders [2.5] continued work with delta winglets by placing them along the tube wall surface of a three-dimensional model of a louvered fin heat exchanger. Sanders [2.5] observed convective heat transfer augmentations as large as 53% with a corresponding increase of 21% in aerodynamic losses. Clearly there is potential for the use of delta winglets as a means of augmenting tube wall heat transfer. The effect of piercings however, on winglet performance needs to be quantified before conclusions can be drawn on their potential benefit in future designs for louvered fin heat exchangers.

Louvered Fin Geometry

The louvered fin geometry used in this study was a realistic three-dimensional geometry provided by a heat exchanger manufacturer (Nino [2.14]), and was the same as that used by Sanders [2.5]. This geometry models the louvers, the flat landing, and the transitional region where the two adjoin as shown in Figure 2.3.

Louver length, including the transitional region from the louver into the flat landing (see Figure 2.3) was 70% of the total fin height. Louvered fins were made from a molding process that involved first constructing a stereolithography model of the fin (Nino [2.14]). The louvered fins were scaled up by a factor of twenty from that of actual heat exchanger dimensions to allow for good measurement resolution.

The louver pattern consisted of 17 louvers, as shown in Figure 2.3, which was comprised of an entrance louver, followed by seven louvers leading into the turnover louver, seven more louvers, and then the exit louver. Entrance, turnover, and exit louvers were twice the length of the other louvers and were specifically designed to turn the flow to increase flow mixing and heat transfer coefficients on the louver surfaces. All louvers had a louver angle of 27°, louver pitch of 27.9 mm, fin pitch of $0.76L_p$, louver thickness of 0.079Lp, fin depth of $20L_p$, and fin height of $5.3L_p$.

Winglet and Piercing Geometries

Several winglet and piercing geometries were tested and compared with baseline testing results. The winglet parameters that were varied included the winglet thickness, aspect ratio, non-dimensional distance from the tube wall, and number of winglets. Figure 2.2 presents the winglet parameters that were varied during testing.

Winglet aspect ratio and distance from the tube wall were varied to determine the effect each parameter had on heat transfer augmentation. Winglet aspect ratios were varied between 1.5 and 3. Note that for all tests the winglet height was fixed at $0.35F_p$. Three different non-dimensional winglet distances from the tube wall of 0.15, 0.22, and 0.29 were tested. In addition, two different winglet thicknesses were tested that included thin winglets having a thickness of 0.03t, as well as realistically thick winglets having a thickness approximately equal to the louver thickness. The realistic thickness was representative of a winglet that would result from the stamping process during louvered fin manufacturing.

To allow piercings to be incorporated into the scaled up louvered fins, square cutouts were machined into the fins. A laser was used to make inserts with piercings that simulated winglet stampings, which fit into the cutouts. Inserts were secured into the cutouts and winglets were placed in the appropriate location. Figure 4 shows an insert simulating a winglet with a piercing and a louvered fin with cutouts. Inserts allowed for a range of piercing locations and

winglet geometries to be tested. Piercings were only simulated using winglets with a thickness of the louvered fins, as this is the thickness that would result from the stamping process. Winglets angled towards the wall were always simulated with piercings downstream of the winglets and for winglets angled away from the wall, piercings were only simulated on the upstream side. For the remainder of this paper, louvered fins incorporating winglets with no piercings will be referred to as solid louvered fins while louvered fins with winglets and piercings will be referred to as pierced louvered fins.

Experiments were conducted incorporating either 28 or 16 winglets into the louvered fin geometry and were only placed in locations corresponding to the cutouts that are seen in Figure 4. For tests using 28 winglets, winglets were placed at every cutout location. Tests using 16 winglets had winglets placed at every other cutout location.

Sanders and Thole [2.5] demonstrated that a winglet angle of attack of 40˚ is near the optimal value to maximize heat transfer performance using a two-dimensional geometry. They also showed that there is little difference in heat transfer performance between winglet configurations having angles of attack of 30˚ and 40˚. For all tests with no piercings, winglets had $\alpha = 40^{\circ}$. To allow for piercings to fit onto the flat landing, tests incorporating piercings had $\alpha = 30^{\circ}$.

During assembly of heat exchanger cores, louvered fins can be placed in a number of different orientations. As such, it is important that the louvered fins perform equally well regardless of flow direction over the fins. For the performance of louvered fins to be independent of flow direction, the winglet and piercing setup should appear the same to the working fluid regardless of flow direction. For this reason, most of the testing performed is for setups that are mirrored (or symmetric) across the turnover louver. Figure 2.5 illustrates the difference between mirrored and non-mirrored winglet configurations. If the louvered fin and winglet geometry are mirrored, regardless of flow direction, the flow field through the heat exchanger will be the same.

Experimental Facilities and Instrumentation

The test rig used for these experiments, shown in Figure 6, was an open loop channel consisting of an inlet nozzle, test section, laminar flow element, and a motor-controlled blower. Excluding the test section, the experimental facility was the same as that used by Sanders and

Thole [2.4], Ebeling and Thole [2.15], Lyman et al. [2.16], and Stephan and Thole [2.17]. The inlet nozzle was designed using CFD to provide uniform flow at the inlet to the test section, which was verified using laser Doppler velocimeter. The nozzle consisted of honeycomb screen leading into a 16:1 area contraction. A 1.5 hp motor, controlled with an AC inverter, powered a centrifugal fan which pulled air through the test section. A laminar flow element for measuring the test section flowrate was located between the test section and the blower.

The test section, shown in Figure 2.7, was designed to accommodate flow periodicity for the three-dimensionality of the fins. The test section is the same as that designed, built, and used by Sanders [2.5] in his study using the same louvered fin geometry with twelve louver rows being simulated. This number of rows has been shown by Springer and Thole [2.18] to be sufficient to allow for periodic flow. The louvered fins were placed in a bounded flow path and were held in by brackets along the side walls, which simulated the tube walls of an actual heat exchanger. The bounding walls on the top and bottom of the test section were designed to simulate natural flow through an infinite louver array. To do so, the top and bottom bounding walls directed flow in the louver region of the fins in the louver direction, while allowing the flow that passed through the channels formed by the flat landings to travel along those landings. The flow path provided by the top and bottom bounding walls can be seen in Figure 2.7.

To simulate the hot tube wall of a heat exchanger, a custom, constant heat flux plate using a sandwich of kapton and inconel was secured to one of the side walls as shown in Figure 2.7. The side of the heater exposed to the test section had a thin copper coating to ensure a constant heat flux surface. The side wall opposite the heater was made of lexan and allowed for visual access to the test section. This wall was not heated, as past studies have shown that the thermal boundary layers from the tube walls do not merge. Therefore to obtain tube wall heat transfer measurements, only one side wall needed to be heated.

As the main purpose of this study was to measure convective heat transfer coefficients along the tube wall, it was important to determine the heat flux on tube wall convected by air passing through the test section. The heat flux produced by the heater was determined by measuring the resistance of the heater and the current passing through it. Conduction losses out the back side of the heated wall were minimized by placing insulating foam behind the heater. In addition, a guard heater, illustrated in Figure 2.7, was placed behind the foam and the temperature was set to match the temperature of the tube wall heater as closely as possible.

Through the use of the foam insulation and guard heater, conduction losses from the back of the test section were typically less than 4% of the total applied heat flux. Another source of heat loss from the tube wall was radiative heat transfer from the copper surface of the kapton heater to the louvered fins. To minimize these losses, fins were painted with a silver paint having an emmisiveity of 0.3. Radiative losses were typically less than 15% of the applied heat flux.

Twenty type E thermocouples were imbedded in the heated tube wall directly behind the heat flux surface. These thermocouples were equally spaced over the length of the louvered fin array in the streamwise direction and were oriented in the center of the channels formed by the flat landings of two fins. To ensure periodic conditions were occurring in the array, thermocouples were placed one channel above and below the thermocouples used for data acquisition to check for periodicity. Tests for heat transfer periodicity in the pitchwise direction indicated less than 4% variation between louver channels. Thermocouples were also placed on the guard heater in locations corresponding to those of the thermocouples imbedded behind the heated side wall. To ensure the accuracy of measurements, at least 200 samples were taken and then averaged. Before Nusselt numbers were calculated, the test rig was allowed to come to steady state, which occurred four hours after the heaters and blower were turned on. Allowing the test rig to run for an additional hour resulted in less than 1% change in average Nusselt number along the heated side wall.

Pressure drop measurements across the louvered fin array were measured with a 0-25 Pascal pressure transducer. Pressure taps were located $0.73L_p$ upstream and downstream of the louvered fins and were drilled into the lexan wall. At least 9000 samples were taken to calculate the pressure drop through the louvered fin array.

Data Analysis and Uncertainty

Nusselt numbers were calculated by determining the amount of heat convected from the heated side wall by the air passing through the test section. Nusselt number was calculated as:

$$Nu = \frac{q''_{total} - q''_{cond}(X) - q_{rad}(X)}{T_{wall}(X) - T_{inlet}} \frac{L_p}{k_{air}} \qquad (1)$$

Radiative heat loss was determined using view factor equations from Modest [2.19]. Losses from conduction were determined using the measured temperature difference between the guard heater and the tube wall heater. The plastic material from which the fins were made had a low

thermal conductivity and the contact area was small such that heat conduction into the fins from the tube wall was negligible.

To quantify winglet performance, Nusselt number augmentations were calculated as a percentage increase over the baseline case having no winglets. Only heat transfer coefficients measured downstream of the first winglet were used to calculate Nusselt number augmentations. For all tests, this corresponded to using only the last eighteen thermocouples in the streamwise direction to calculate augmentations.

Pressure losses for different winglet and piercing setups were characterized by Fanning friction factors, calculated using the equation:

$$f = \frac{D_H}{4F_d}\left(\frac{2\Delta P}{U_{ff}{}^2 \rho_{air}} - K_c - K_e\right) \tag{2}$$

Sudden flow area change as air enters and exits the louvered array were accounted for through loss coefficients K_c and K_e determined from White [2.20].

Methods described by Moffat [2.21] were used to calculate uncertainties in Reynolds number, Nusselt numbers, and friction factor. The largest uncertainty in measured Nusselt number occurred at the entrance louver where the temperature difference between the heated side wall and free stream air was at a minimum. At this location Nusselt number uncertainty was as high as 7%. Typically, averaged Nusselt uncertainties were 4%, 4%, and 3% for Reynolds numbers of 215, 577, and 955 respectively. Friction factor uncertainty was 8% at a Reynolds number of 955, and increased with decreasing Reynolds number. Low pressure drops through the test section at the Reynolds number of 216 caused the friction factor uncertainty to be 51%. Because of the high uncertainties associated with pressure drop measurements at Reynolds numbers of 216 and 577, this paper will only use friction factor data measured at Reynolds number 955 to make comparisons between different winglet and piercing geometries.

Baseline Measurements for Two- and Three-Dimensional Solid Louvered Fins

Comparisons are made in this section of the paper between two- (Sanders and Thole [2.4]) and three-dimensional solid louvered fins with no winglets. Figure 2.8 shows measured Nusselt numbers along the tube wall for both configurations at Re = 216 and 955. As was expected, the Nusselt numbers started high as the leading edge of the tube wall heater initiated the thermal boundary layer, and then slowly decreased as the boundary layer along the tube wall

grew. There was a significant difference in measured tube wall Nusselt numbers between the two- and three-dimensional geometries. While the streamwise-averaged Nusselt numbers were within 1% for the two- and three-dimensional louvered fins at Re = 955, the local data showed differences. The most notable difference occurred just after the turnover louver ($X \approx 0.6$) where, for the two-dimensional louvered fin, a significant increase in Nusselt number was measured with no increase in Nusselt number for the three-dimensional louvered fin.

Smoke visualization indicated that there were fundamentally different flow fields along the tube wall for the two- and three-dimensional geometries. Flow through the two-dimensional louvered fin array was louver-directed near the tube wall since the louver was immediately adjacent to the tube wall. As designed, the turnover caused a flow re-direction which lead to flow mixing with an accompanying increase in Nusselt number downstream of the turnover louver.

Flow through the three-dimensional louvered fin array contained two defined flow regimes. As shown in Figure 2.7, flow passing through the louvered region of the three-dimensional fins became louver directed, as with the two-dimensional louvered fin; however, flow along the tube wall where the fin has a flat landing was similar to channel flow which is undisturbed by the louvers. As such, the measurements for the three-dimensional louvered fins did not show the effect of the turnover louver because of the channel-like flow along the tube wall. While the turnover louver would influence heat transfer on the louver surfaces for the three-dimensional geometry, the flow disturbances have a minimal effect on heat transfer coefficients along the tube wall. Considering that significantly different flow fields were observed for the two- and three-dimensional louvered fin geometries, it was expected that the effect of winglets placed on the louvered fins would also be appreciably different for the two geometries as will be shown in the next sections of this paper.

Measured pressure losses through the two- and three-dimensional louvered fin arrays were converted to friction factors, which allowed for comparisons to be made to data provided by a heat exchanger manufacturer (Nino [2.14]) for an actual heat exchanger core. Figure 2.9 presents the results of this comparison. Excluding the measured friction factor at Re = 216, which had high associated experimental uncertainty, measured friction factors for the three-dimensional geometry were slightly lower than the manufacturer's data. This was expected because the geometry tested in this study does not model the tube wall thickness of an actual heat

exchanger. The blockage of the tube wall increases pressure losses, which would cause the higher friction factors measured by the manufacturer. Friction factor measurements were larger than the manufacturer's data for the two-dimensional louvered fin array. Two-dimensional louvered fins caused larger pressure drops compared to three-dimensional louvered fins because flow traveled a greater distance along the tube wall, encountering more friction, before it exited the test section as the flow was louver-directed.

The remainder of this paper quantifies the effects of winglets and piercings on tube wall heat transfer and friction factor. The effects of winglet geometry and mirroring winglets across the turnover louver were studied using a solid louvered fin and will be reported. In addition, the mirrored winglet configurations that produced the highest heat transfer augmentations were further studied by including piercings into the louvered fin geometry.

Winglet Augmentations for Two- and Three-Dimensional Solid Louvered Fins

Sanders [2.5] reported that winglets angled towards the tube wall produced small heat transfer augmentations when implemented into a two-dimensional louvered fin geometry. Measurements showed a reduction in heat transfer (-3% with respect to the baseline) at Re =216 with little positive augmentation (3%) at Re = 955. Conversely, incorporating winglets into a three-dimensional louvered fin geometry resulted in heat transfer augmentations of 1% and 47% at Re = 216 and 955 respectively. Figure 2.10 compares the dramatic difference in winglets' influence on heat transfer performance in two- and three-dimensional louvered fin arrays. Note that shown below the graph is a diagram of the winglet configuration used which was, $\alpha = 40°$, $\Lambda = 1.5$, $Z = 0.22$, with 28 winglets angled towards the wall in a non-mirrored configuration. As shown in Figure 2.10, winglets on the three-dimensional louvered fin increased average Nusselt number starting with the first winglet. Beginning at the turnover louver, on which there were no winglets, Nusselt numbers decreased before increasing again after the turnover where winglets were again implemented onto the louvered fin surfaces.

There are two physical mechanisms that lead to enhanced heat transfer along the tube wall from the use of winglets. The first of mechanisms is the re-direction of cool freestream air towards the tube wall, whereby Nusselt number is increased. The second mechanism is the formation of vortices by winglets that serve to enhance flow mixing and heat transfer along the tube wall.

The computational study of Lawson et al. [2.3] suggests that vortices produced by winglets in a two-dimensional louvered fin array are ineffective because the vortices are disrupted by downstream louvers after only propagating a short distance in the streamwise direction. Figure 2.11 demonstrates how, in a two-dimensional louvered fin array, winglets form vortices but the vortices are unable to propagate because they are formed in a region of louver directed flow. In Figure 2.11 the vortex can be seen forming as air rolls over the winglet from the pressure to the suction side. The vortex is present downstream but is then disrupted as the vortex impacts the leading edge of the next louver in the streamwise direction. Conversely, for the three-dimensional louvered fin geometry, winglets are placed in the channel-like flow along the tube wall, where vortices that are formed propagate without being disrupted by louvers. Vortex propagation was the mechanism that caused the large Nusselt number augmentations in the three-dimensional louvered fin geometry that were not present for the two-dimensional louvered fin geometry.

In this study both the two- and three-dimensional geometries showed small augmentations at Re = 216. Because of the low Reynolds number, it is believed that winglets were unable to cause significant mixing. The trend of winglets producing negligible augmentations at Re = 216 was measured for all tests performed. This study found no winglet configuration that provided more than 2% augmentation in Nusselt number at Re = 216. At Re = 216 winglets were determined to be ineffective for increasing heat transfer along the tube wall.

The data clearly demonstrated that due to the different flow fields present for two- and three-dimensional louvered fin geometries, modeling a louvered fin heat exchanger with a two-dimensional geometry inaccurately predicted the effect winglets have on augmenting heat transfer over the tube wall. To make measurements that will have practical significance in quantifying winglet effects on tube wall heat transfer, the three-dimensionality of the heat exchanger core needs to be considered.

Mirrored Winglet Configurations for Three-Dimensional Solid Louvered Fins

During the assembly of heat exchanger cores, a louvered fin array incorporating winglets can be placed in several orientations. As such, for a winglet configuration to be of practical use in a heat exchanger, the configuration should provide performance enhancements that are independent of the flow direction relative to the louvers. To simulate this in our experiments, the

winglet setup was mirrored downstream of the turnover louver. Figure 5 illustrates the definition of mirroring winglets across the turnover louver.

Nusselt number measurements, as shown in Figure 2.12, indicated mirroring the winglet setup decreased Nusselt number augmentation compared to a non-mirrored winglet configuration. The non-mirrored configuration produced average augmentations of 47%, 30%, and 1%, while mirroring the configuration decreased augmentations to 33%, 14%, and -5% at Re = 955, 577, and 216 respectively. Before the turnover louver where winglets were angled at the wall the non-mirrored and mirrored configurations performed similarly. At $X \approx 0.6$ however, which was the location of the first winglet angled away from the wall, augmentations decreased. The large decrease in augmentation, which started at $X \approx 0.6$, suggested that the winglets angled away from the wall decreased the positive average effect on heat transfer by either forcing vortex formation to occur at a distance from the tube wall where vortices were unable to cause mixing in the thermal boundary layer, or by decreasing the amount of freestream air that came in contact with the tube wall. Figure 2.13 shows the Nusselt number augmentation at each measurement location along the tube wall. Starting at $X \approx 0.6$ the reduction in augmentations caused by winglets angled away from the tube wall can clearly be seen.

Non-mirrored and mirrored winglet configurations showed only small differences in friction factor performance. The non-mirrored configuration increased friction factor measurements by 19%, while the mirrored configuration showed a 25% increase at Re = 955. This was expected as half the winglets in the mirrored case had the large end facing upstream, which has been determined by Sanders [2.5] to cause larger pressure losses than winglets with the smaller end facing upstream.

Mirroring the winglet configuration across the turnover louver negatively affected winglet performance; however, augmentations of up to 33% in heat transfer were still achieved. Although non-mirrored winglet configurations showed larger heat transfer augmentations with lower increases in friction factor, the remainder of the results reported in this study will be for mirrored winglet configurations in an attempt to present results relevant to an assembled heat exchanger.

Winglet Geometry Effects on Three-Dimensional Solid Louvered Fins

Sanders and Thole [2.4] demonstrated that winglet aspect ratio and distance from tube wall affected heat transfer performance in a two-dimensional louvered fin geometry. It is important to note that aspect ratio is a ratio of winglet height to the base, where aspect ratio decreases with winglet size because the winglet height is fixed. This study demonstrated that the effects of winglets measured for a two-dimensional geometry can not be applied to the three-dimensional geometry. Therefore, the effects of varying winglet aspect ratio and distance from the tube wall were measured using the three-dimensional louvered fin geometry. Aspect ratio and distance from tube wall both affected Nusselt number measurements as shown by Figures 2.14 and 2.15.

As seen in Figure 2.14, Nusselt number augmentations increased with decreasing aspect ratio. At Re = 955, the measured augmentation averages were 24%, 28%, and 33% for aspect ratio's of 3, 2, and 1.5 respectively. On flat plates, the vortex strength has been observed to be dependent on winglet aspect ratio with smaller aspect ratio winglets forming stronger vortices. Consistent with flat plate results, increases in Nusselt number augmentations with decreasing aspect ratio occurred because smaller aspect ratio winglets formed stronger vortices that increased flow mixing along the tube wall. Due to the blockages of larger winglets, friction factors also increased with decreasing aspect ratio from 11% for $\Lambda = 3$ to 22% for $\Lambda = 1.5$ at Re = 955.

Figure 2.15 clearly shows that as winglets were placed closer to the tube wall on the three-dimensional louvered fins, Nusselt number augmentations increased. At Re = 955 for Z = 0.15, 0.22, and 0.29, augmentation averages were 33.4%, 32.9% and 31.1% respectively. While increases were seen in augmentations with decreasing winglet distance from the tube wall, there was only a 2.3% difference between the highest and lowest augmentations observed at Re = 955. Winglet placement influenced the position of vortices with respect to the tube wall. Vortex strength and not location were shown by Gentry and Jacobi [2.12] to be the more dominant factor influencing heat transfer. The results of the winglet distance from tube wall tests agreed with Gentry and Jacobi's [2.12] findings as distance from tube wall was shown to be a minor a minor effect on heat transfer augmentation. Similarly, varying winglet distance from the tube wall was shown to have negligible effects on friction factor. Friction factor increases varied

between 22% and 24% for Z = 0.22 and 0.15 respectively at Re = 955, which was within the experimental uncertainty.

The experiments for determining the effects of varying winglet aspect ratio and distance from tube wall were performed using a winglet thickness of 0.03t. Pierced louver testing was performed using winglets having a winglet thickness equal to the louver thickness, which is representative of winglets that can be manufactured. To determine if the same Nusselt number trends would result from using thick winglets, the effect of winglet thickness on heat transfer performance was measured. Figure 2.16 presents measured Nusselt numbers for thick and thin winglet configurations. The average Nusselt number augmentations were nearly the same and, more importantly, trends were the same. These data indicated that winglet thickness was also not a significant variable.

Maintaining the structural integrity of louvered fins is an important consideration. As such, we considered the effects of varying the number of winglets placed on the louvered fins. To determine if winglet performance was better for 16 or 28 winglet configurations, a comparison was performed. Figure 2.17 presents the Nusselt number data measured for the 16 versus 28 winglet comparison tests. There was little difference between the 16 and 28 winglet configurations with only a 2% difference (33% and 31% for the 28 and 16 winglet configurations respectively) in Nusselt number augmentation at Re = 955 and a 1% (14% and 15% for the 28 and 16 winglet configurations respectively) difference at Re = 577. Figure 2.17 shows the 28 winglet configuration provided a significant advantage over the 16 winglet configuration in augmenting Nusselt number before the turnover louver. The overall advantage of the 28 winglet configuration is lessened after the turnover, where the 16 winglet configuration provided higher Nusselt number augmentation. The 28 winglet configuration performed worse than the 16 winglet configuration after the turnover louver because it had more winglets angled away from the wall. The winglets angled away from the wall directed air away from the wall, decreasing the flow rate, and made it more difficult for low temperature freestream fluid to cool the tube wall after the turnover louver. Friction factor measurements indicated no difference between 16 and 28 winglet configurations with both having approximately a 25% friction factor increase at Re = 955.

Effects of Simulated Piercings on Three-Dimensional Louvered Fins

Based on the findings of the solid louvered fin winglet tests, two winglet geometries were chosen to test the effect of piercings on winglet performance. The two winglet configurations chosen differed only in the aspect ratio of the winglets used. $\Lambda = 1.5$ winglets were selected because these were observed to produce the highest heat transfer augmentation in solid louvered fin testing. Minimizing the piercing area was an important consideration because any area removed from the louvered fin would decrease the fin's structural integrity, and also the area available for heat conduction from the tube wall through the louvered fins. For this reason, $\Lambda = 2$ winglets were testes as piercing area decreased with increasing winglet aspect ratio.

Figure 2.18 indicates piercings reduced the Nusselt number augmentation produced by winglets. The highest augmentations measured for the pierced louvered fin configurations were 24% and 8%,which corresponds to a 11% and 9% reduction in heat transfer compared to the same solid louvered fin winglet configuration at Re = 955 and 577 respectively. Measured reductions in heat transfer augmentation occurred only before the turnover louver where winglets were angled towards the tube wall. After the turnover louver where winglets were angled away from the wall there were no negative effects of piercings. Piercings actually increased Nusselt number augmentation after the turnover louver. The decreased augmentation due to the piercings was caused by flow ingestion through the piercings. Smoke visualization showed that when piercings were implemented into the louvered fin geometry, flow through the channels formed by the flat landings near the tube wall no longer passed along the tube wall. Piercings provided a flow path that allowed the channel directed flow to follow more closely the louver directed flow. The flow through the piercings disrupted the vortex formation which decreased the ability of winglets to augment heat transfer.

In the solid louvered fin tests, decreasing winglet aspect ratios was consistently shown to increase Nusselt number augmentation. With pierced louvered fins however, smaller aspect ratio winglets had larger piercings and allowed more flow to be ingested. As can be seen by comparing Figures 2.14 and 2.18, smaller piercings, $\Lambda = 2$ winglets caused larger Nusselt number augmentation at Re = 955. Although smaller aspect ratio winglets created stronger vortices and redirect more air towards the tube wall, these effects were offset by more flow passing through the large $\Lambda = 1.5$ piercings.

Augmentation results at each measurement location for the pierced and solid louvered fins, shown in Figure 2.19, indicated that before the turnover louver, winglets with $\Lambda = 2$

produced higher augmentations, and after the turnover louver the larger $\Lambda = 1.5$ winglets produced higher Nusselt number augmentations. It was also interesting to observe that negative effects of piercings only occurred before the turnover louver, where the winglets were angled towards the tube wall. After the turnover louver, where winglets were angled away from the wall, piercings increased Nusselt number augmentation compared to the solid louvered fins. It was shown previously that winglets angled away from the tube wall direct air away from the wall decreasing the Nusselt number augmentation. Piercings interfered with the winglet influence causing the larger Nusselt number augmentations after the turnover louver for the pierced louvered fin configurations. Flow passing through the piercings also explains why $\Lambda = 1.5$ winglets with the largest piercings outperformed $\Lambda = 2$ winglets after the turnover louver. The piercings of the $\Lambda = 1.5$ winglets provided a larger flow path than piercings for the $\Lambda = 2$ winglets. As such, the $\Lambda = 1.5$ winglets did not direct as much air away from the tube wall as the $\Lambda = 2$ winglets did, causing the $\Lambda = 1.5$ winglets to perform better after the turnover louver.

Friction factor tests indicated that piercings decreased the friction factors through the test section relative to the solid louvered fin configuration. The solid louvered fin configuration produced friction factor increases of 25% over the baseline, while the pierced louvered fin configurations had only 18% and 10% for $\Lambda = 1.5$ and 2 respectively at $Re = 955$. Flow through the piercings caused less shear at the interface between the louver-directed flow and channel-directed flow regimes. The reduction in shear between the regions of channel flow and louver-directed flow accounted for the measured decrease in friction factor relative to the solid louver.

Conclusions

This study investigated the use of delta winglets as a means to increase tube wall heat transfer in louvered fin heat exchangers. Tests were performed using a three-dimensional louvered fin geometry incorporating delta winglets and winglet piercings. By comparing the results to past studies performed using two-dimensional louvered fin geometries, it was demonstrated that the three-dimensionality of louvered fins affected the winglet performance.

For a two-dimensional geometry, Sanders [2.5] found that delta winglets angled towards the tube wall produced 3% Nusselt number augmentation at a Reynolds number of 955. The three-dimensional louvered fin geometry enabled delta winglets for the same configuration induced as much as a 47% Nusselt number augmentation at the same Reynolds number. The

mechanism causing heat transfer augmentation for the three-dimensional louvered fin geometry was flow mixing in the tube wall thermal boundary layer caused by vortices sweeping the tube wall surface. The vortices formed in the two-dimensional louvered fin array were disrupted by downstream louvers after propagating only a short distance; therefore, lower Nusselt number augmentations were measured.

Louvered fin geometries should be independent of flow direction given that louvered fin heat exchanger cores may be assembled in a number of different orientations during heat exchanger manufacturing. This variability requires winglet configurations to be mirrored across the turnover louver. Results show mirroring the winglet configuration decreases the positive benefits of delta winglets. Adverse effects of mirrored winglet configurations were measured after the turnover louver because winglets were angled away from the tube wall as opposed to towards the wall in the upstream portion of the louvered fin array.

Piercings in the louvered fins also decreased winglet benefits on augmenting heat transfer. Piercings disrupted the vortex formation by allowing flow to pass through the piercings following more closely the louver directed flow path. While piercings were shown to negatively affect heat transfer performance along the tube wall relative to solid louvered fins, they have the desirable effect of lowering pressure losses.

It is important to note that heat transfer augmentations reported in this paper only take into account heat transfer along the tube wall surface. Winglets with piercings will also have effects on heat exchanger performance not accounted for by only measuring tube wall Nusselt numbers. Other surfaces in the heat exchanger, such as the flat landings near the tube wall, that are swept by vortices would have likely shown increases in heat transfer. Another effect of incorporating winglets and piercing into louvered fin designs is a decrease in the area available for heat conduction from the tube wall through the louvered fins. This area reduction could possibly cause a decrease in louver heat transfer.

Overall, this study found that delta winglets including simulated piercings are a promising means of augmenting heat transfer in louvered fin heat exchangers, providing up to 24% augmentation over the tube wall surface. For a final conclusion to be reached on the practicality of implementing delta winglets into louvered fin heat exchanger designs, overall heat exchanger performance must be measured where all winglet and piercing effects are accounted for with a three-dimensional louvered fin model.

Acknowledgements

The authors would like to acknowledge Modine Manufacturing Inc. for their support on this project. In particular the authors would like to thank Drs. Victor Nino and Steve Memory who have provided technical feedback for this work.

References

[2.1] Yu-Juei Chang, Kuei-Chang Hsu, Yur-Tsai Lin, Chi-Chuan Wang, 2000, "A Generalized Friction Correlation for Louver Fin Geometry," *International Journal of Heat and Mass Transfer*, vol. 43, pp. 2237-2243.

[2.2] Yu-Juei Chang and Chi-Chuan Wang, 1997, "A Generalized Heat Transfer Correlation for Louver Fin Geometry," *International Journal of Heat and Mass Transfer*, vol. 40, pp. 533-544.

[2.3] Lawson, M.J., Sanders, P., Thole, K.A., 2006, "A Computational and Experimental Comparison of Tube Wall Heat Transfer Augmented by Winglets in Louvered Fin Heat Exchangers", under review, International Mechanical Engineering Congress and Exhibition, Chicago IL.

[2.4] Sanders, P. and Thole, K. A., 2006, "Effects of Winglets to Augment Tube Wall Heat Transfer in Louvered Fin Heat Exchangers," *International Journal of Heat and Mass Transfer*, (in press).

[2.5] Sanders P., "Effects of Louver Length and Vortex Generators to Augment Tube Wall Heat Transfer in Louvered Fin Heat Exchangers", 2005, MSME Thesis, Virginia Tech.

[2.6] Beauvais, F. N., 1965, "An Aerodynamic Look at Automotive Radiators," SAE Paper No. 650470.

[2.7] Davenport, C.J., 1983, "Correlations for Heat Transfer and Flow Friction Characteristics of Louvered Heat Exchanger Surfaces," AICHE Symposium Series, vol. 79, pp. 19-27.

[2.8] Achaichia, A. and Cowell, T. A., 1988, "Heat Transfer and Pressure Drop Characteristics of Flat Tube and Louvered Plate Fin Surfaces," *Experimental Thermal and Fluid Sciences* vol. 1, pp. 147-157.

[2.9] Atkinson, K. N., Draulic, R., Heikal, M. R., Cowell, T. A., 1998, "Two- and Three-Dimensional Numerical Models of Flow and Heat Transfer Over Louvered Fin Arrays in Compact Heat Exchangers," *International Journal of Heat and Mass Transfer*, vol. 41, pp. 4063-4080.

[2.10] Tafti, D. K. and Cui, J., 2003, "Fin–tube Junction Effects on Flow and Heat Transfer in Flat Tube Multilouvered Heat Exchangers," *International Journal of Heat and Mass Transfer*, vol. 46, pp. 2027-2038.

[2.11] Biswas, G., Torii, K., Fujii, D., Nishino, K., 1996, "Numerical and Experimental Determination of Flow Structure and Heat Transfer Effects of Longitudinal Vortices in a Channel Flow," *International Journal of Heat and Mass Transfer*, vol. 39, pp. 3441-3451.

[2.12] Gentry, M. C. and Jacobi, A. M., 2002, "Heat Transfer Enhancement by Delta-Wing-Generated Tip Vortices in Flat Plate and Developing Channel Flows," *International Journal of Heat and Mass Transfer*, vol. 124, pp. 1158-1168.

[2.13] Vasudevan, R., Eswaran, V., Biswas, G., 2000, "Winglet-Type Vortex Generators for Plate Fin Heat Exchangers Using Triangular Fins," *Numerical Heat Transfer*, vol. 58 , pp. 533-555.

[2.14] Nino, V. G., 2006, Personal communication through Modine Manufacturing.

[2.15] Ebeling, C., and Thole, K. A., 2004, "Measurements and Predictions of the Heat Transfer at the Tube-Fin Junction for Louvered Fin Heat Exchangers," *International Journal of Compact Heat Exchangers*, vol. 5, pp. 265-286.

[2.16] Lyman, A. C., Stephan, R. A., Thole, K. A., Zhang, L., Memory, S., 2002, "Scaling of Heat Transfer Coefficients Along Louvered Fins," *Experimental Thermal Fluid Science*, vol. 26, pp. 547-563.

[2.17] Stephan, R. A., and Thole, K. A., 2005, "Optimization Study Relevant to Louvered Fin Heat Exchangers," *International Journal of Heat Exchangers*, vol. 6, pp. 73-92.

[2.18] Springer, M. E., and Thole, K. A., 1998, "Experimental Design for Flowfield Studies of Louvered Fins," *Experimental Thermal and Fluid Science*, vol. 18, pp. 258-269.

[2.19] Modest, M. F., *Radiative Heat Transfer*, 2nd ed., Academic Press, New York, 2003.

[2.20] White, F. M., *Fluid Mechanics*, 4th ed., McGraw-Hill, New York, 1999.

[2.21] Moffat, R. J., "Describing the Uncertainties in Experimental Results," *Experimental Thermal and Fluid Science*, vol. 1, pp. 3-17, 1988.

Figures

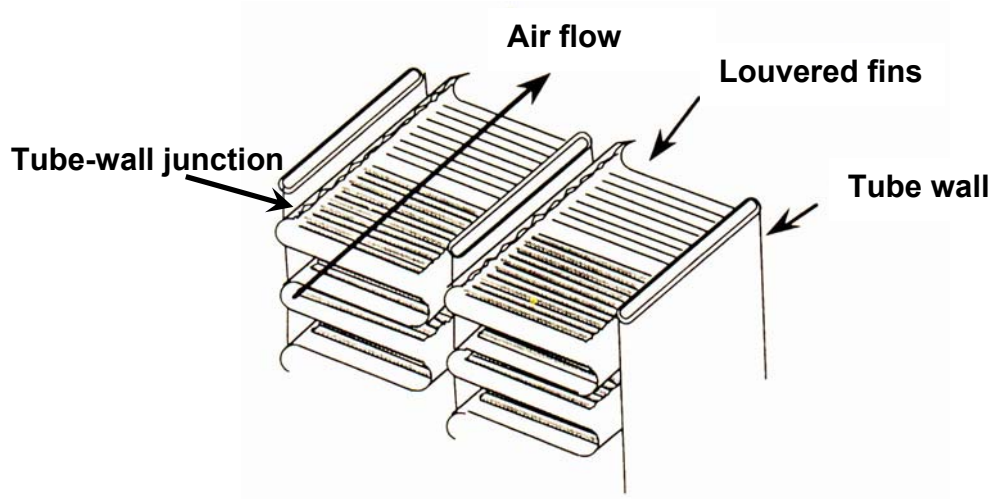

Figure 2.1. Louvered fin heat exchanger showing the location of the tube-wall junction.

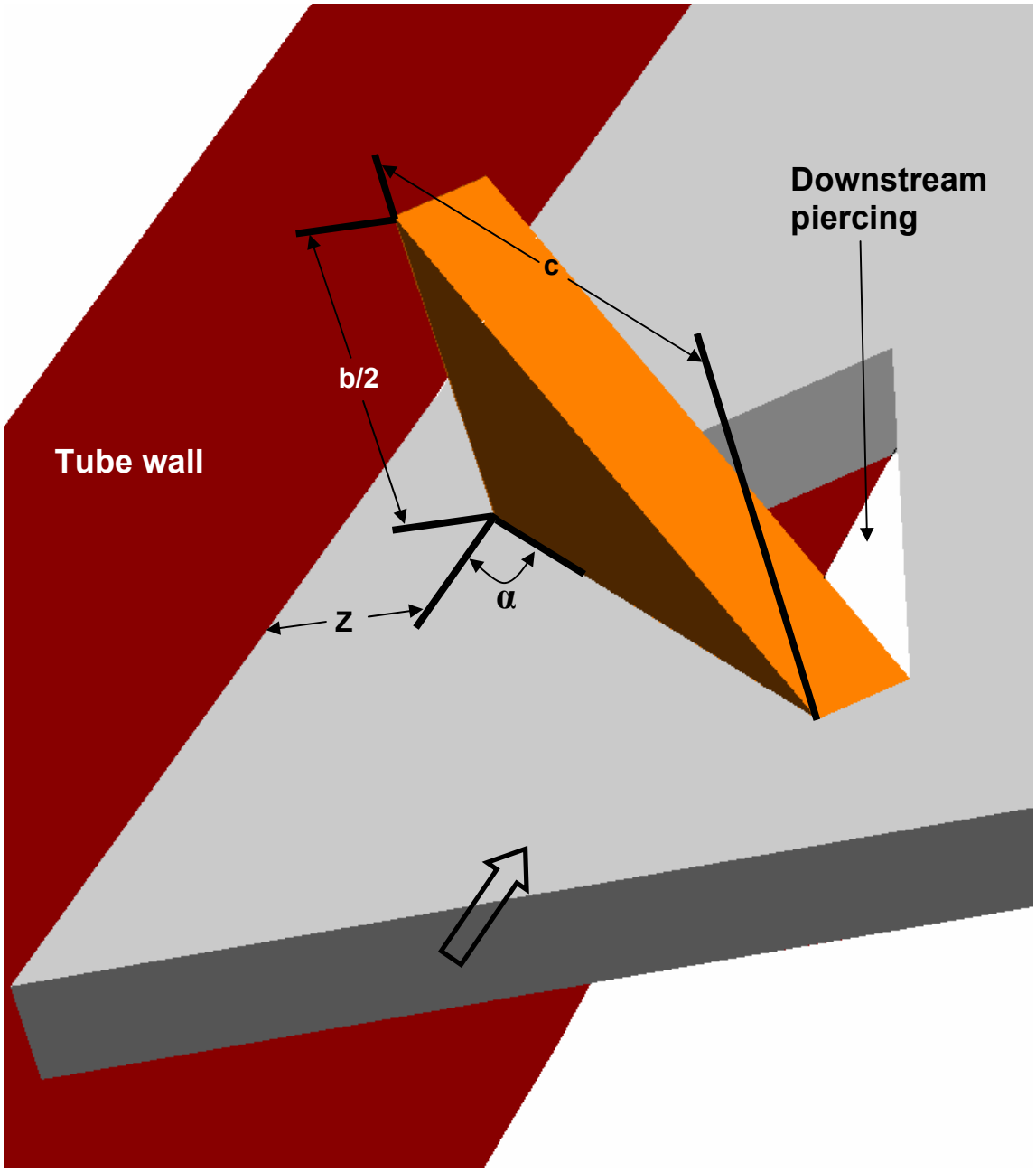

Figure 2.2. Diagram of a delta winglet vortex generator.

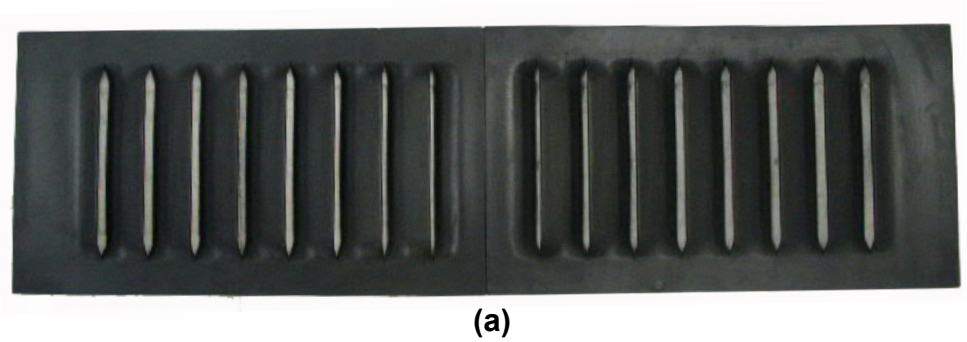

(a)

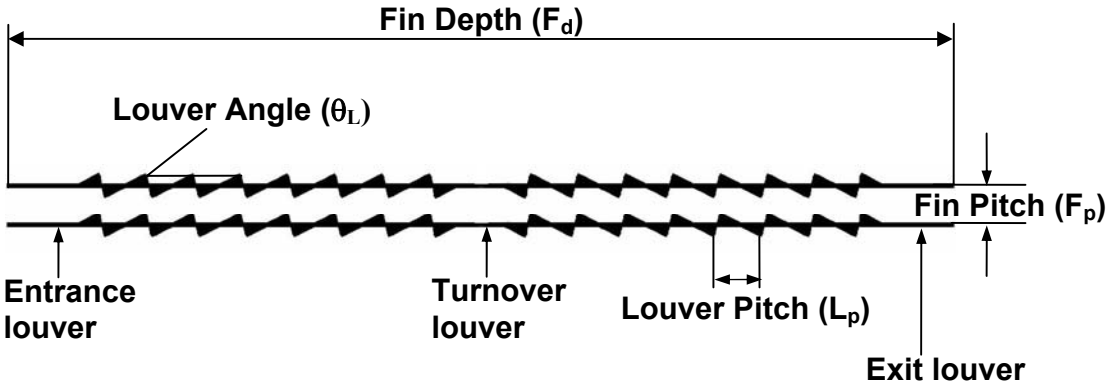

(b)

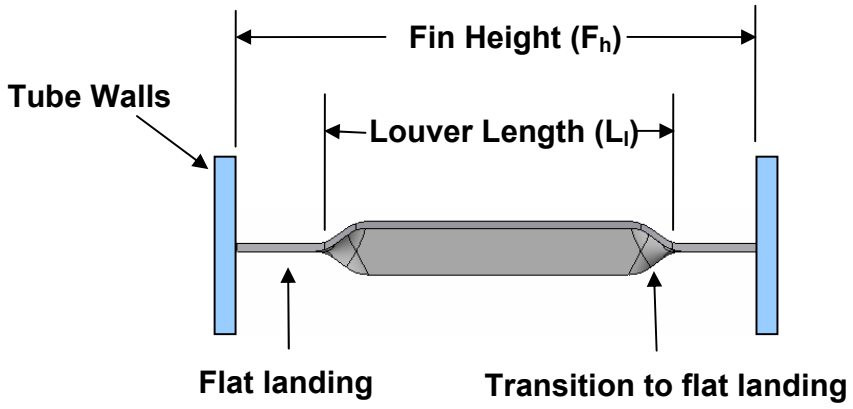

(c)

Figure 2.3. Actual louvered fin geometry used in testing, (a) – picture of the top view, (b) – side view, and (c) – front view. Note that the fin was molded in two pieces as seen in (a).

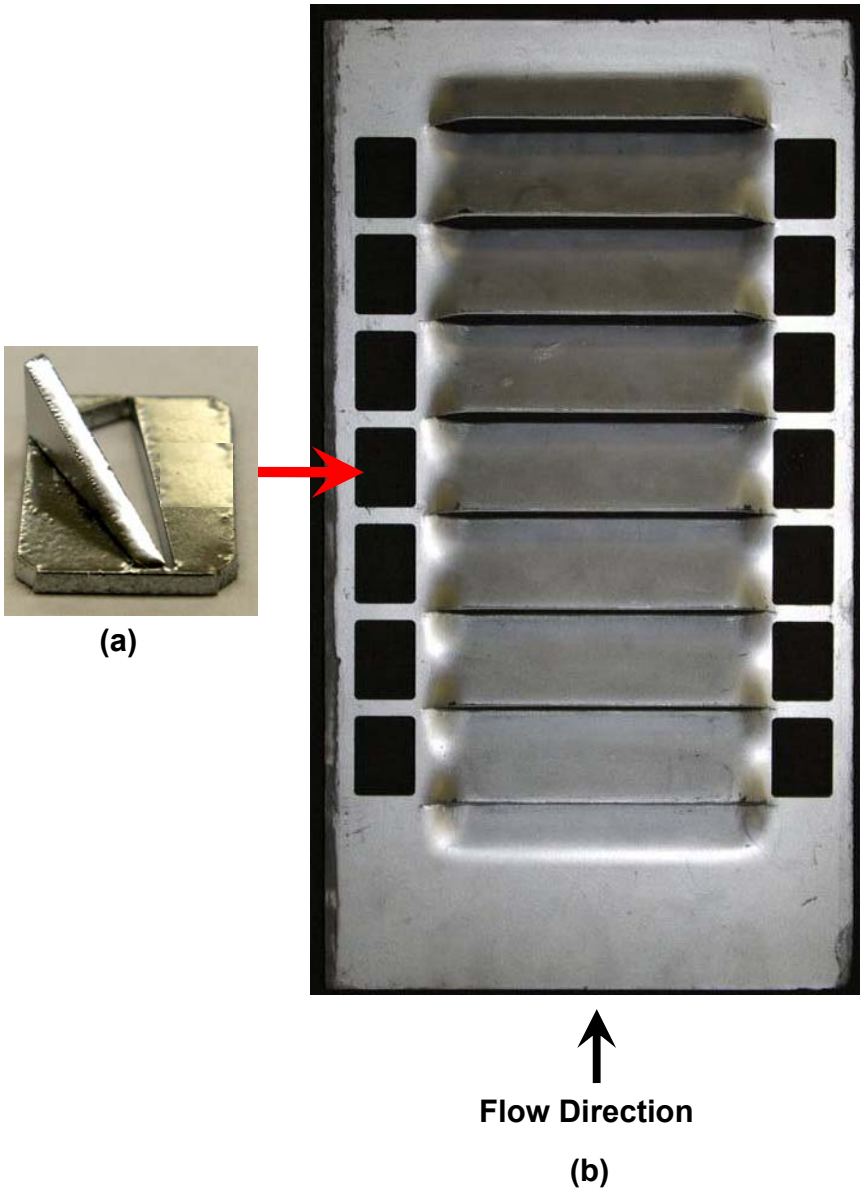

Figure 2.4. (a) – Plexiglas winglet and insert used to simulate piercings and (b) – Cutouts milled into a realistic three-dimensional louvered fin.

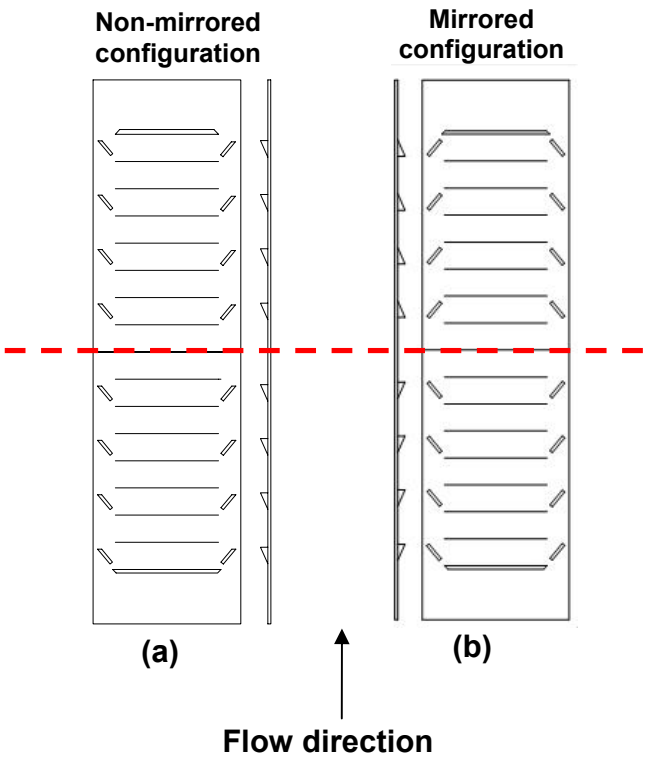

Figure 2.5. (a) – Mirrored and (b) – non-mirrored winglet configurations. The red dotted line passing through the turnover louver is the plane across which the winglet setup must be mirrored.

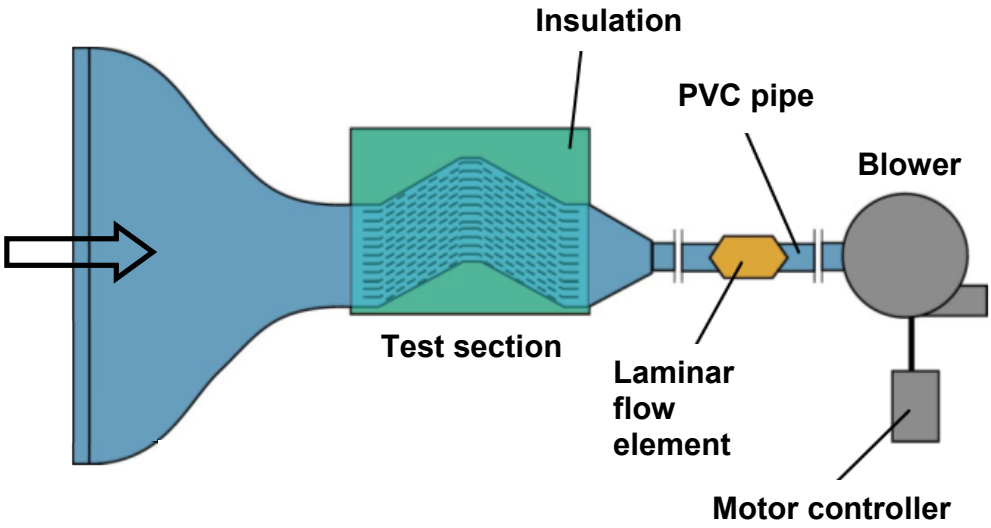

Figure 2.6. Schematic of the open loop wind tunnel used for all experiments.

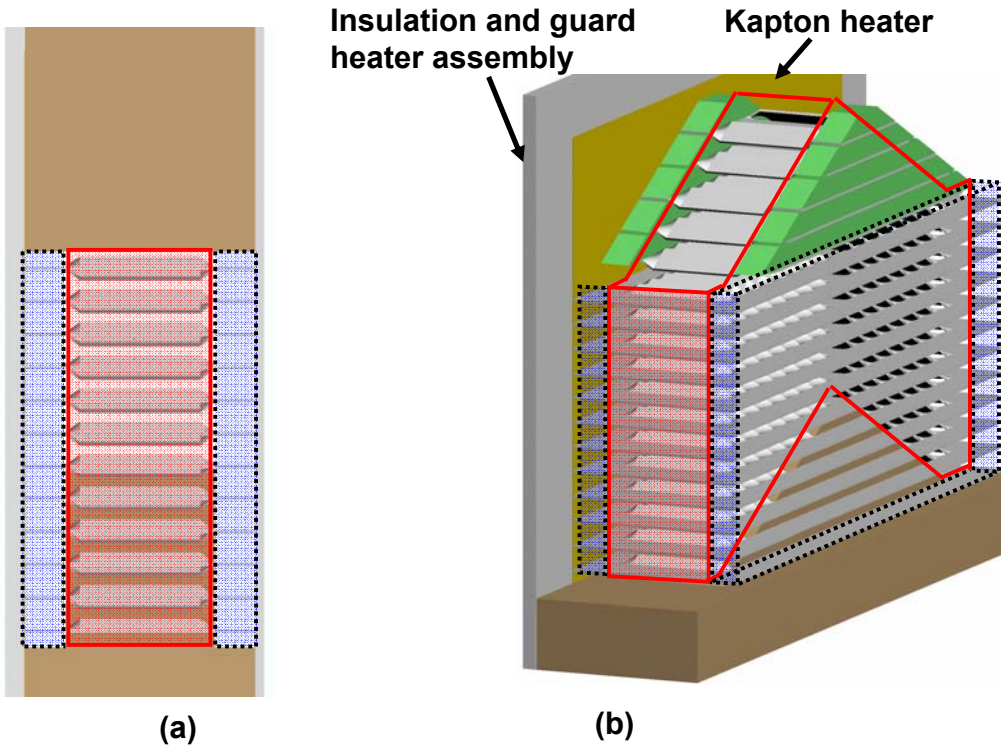

Figure 2.7. (a) – Front view, and (b) – isometric view of the test section used. The solid outlined areas indicate the region through which louver directed flow traveled. The dotted outlined areas indicated the region of flows over the flat landings at the edge of the fins.

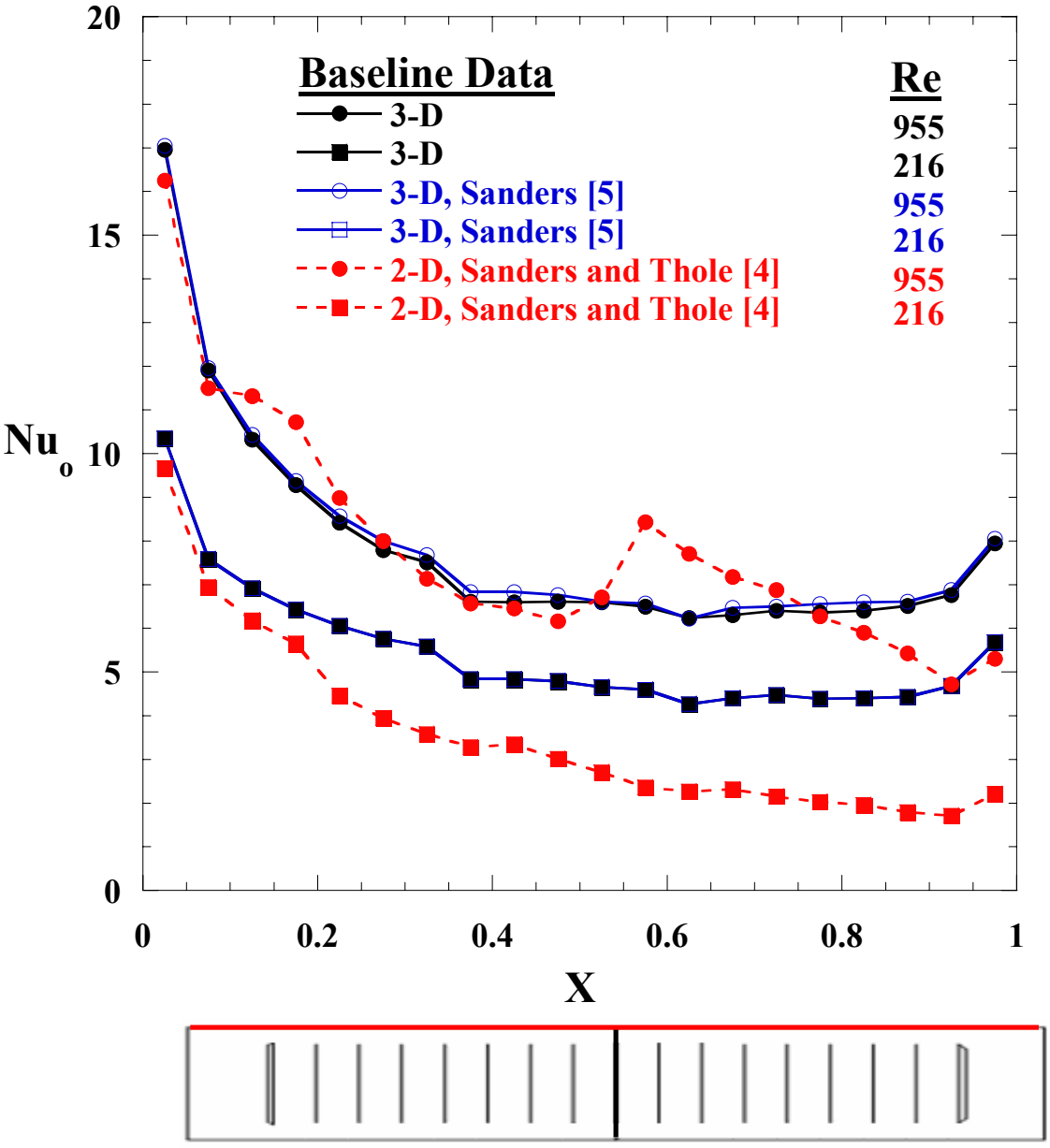

Figure 2.8. Two- and three-dimensional baseline heat transfer results. Also shown are baseline measurements made by Sanders [5] using the same louvered fin geometry. X = 0 corresponds to the entrance of the louvered fin array.

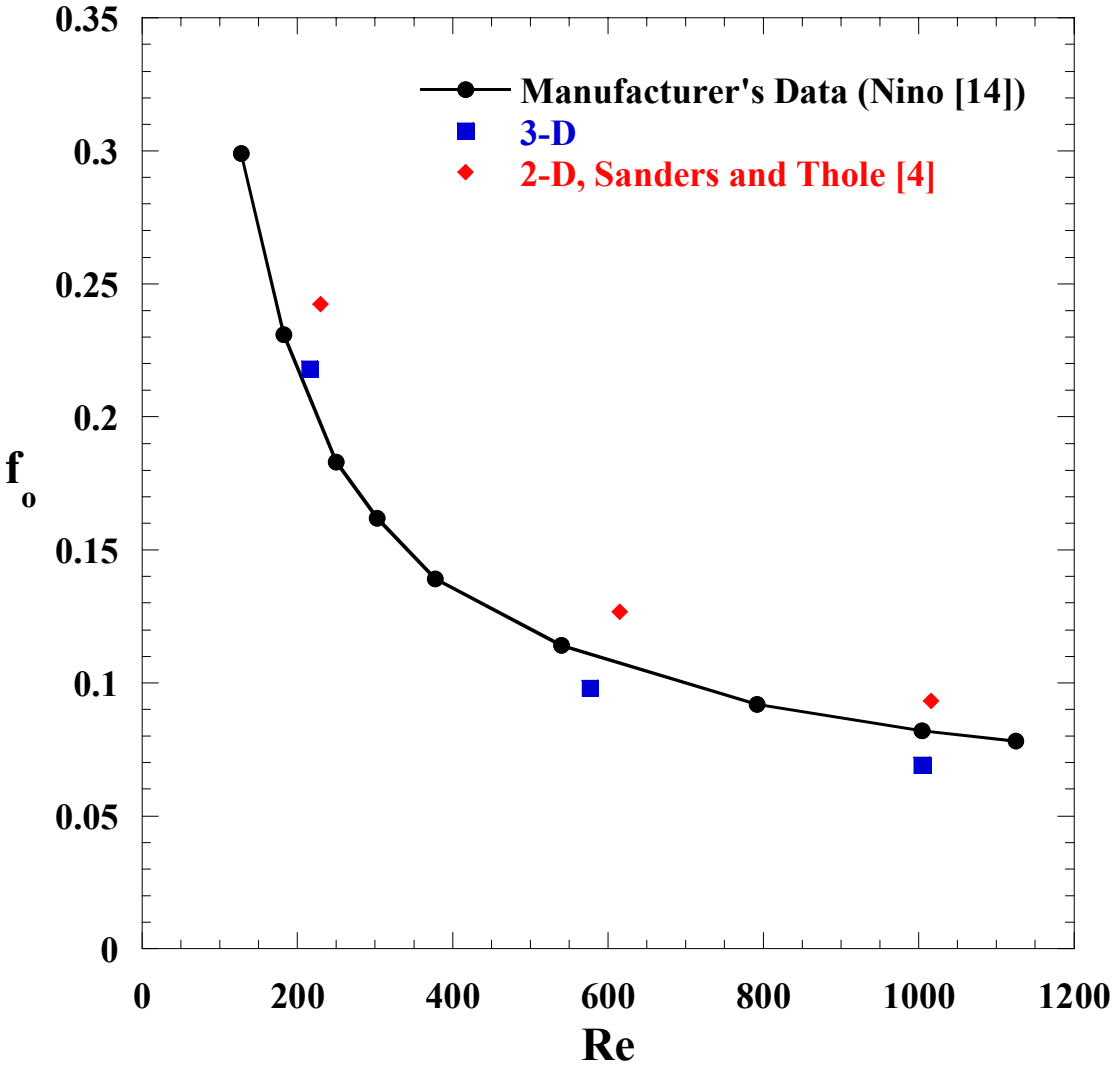

Figure 2.9. Baseline friction factors measured between $0.73L_p$ up and downstream of the louvered fin array compared to a manufacturer's data (Nino [14]).

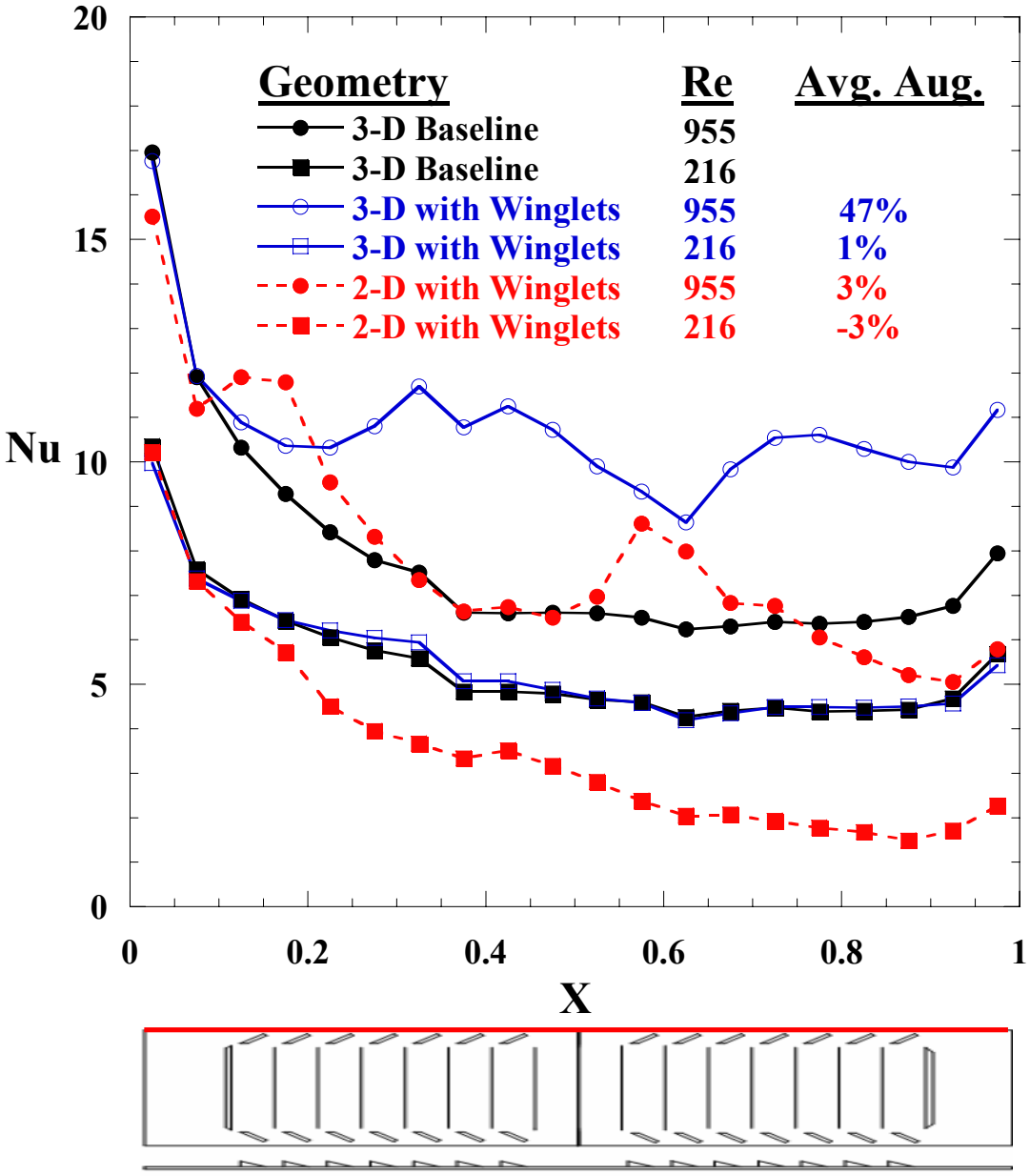

Figure 2.10. Comparison of heat transfer performance using two- and three-dimensional solid louvered fin geometries. $t_w = 0.03t$ for the two-dimensional louvered fins, $t_w = t$ for the three-dimensional louvered fins.

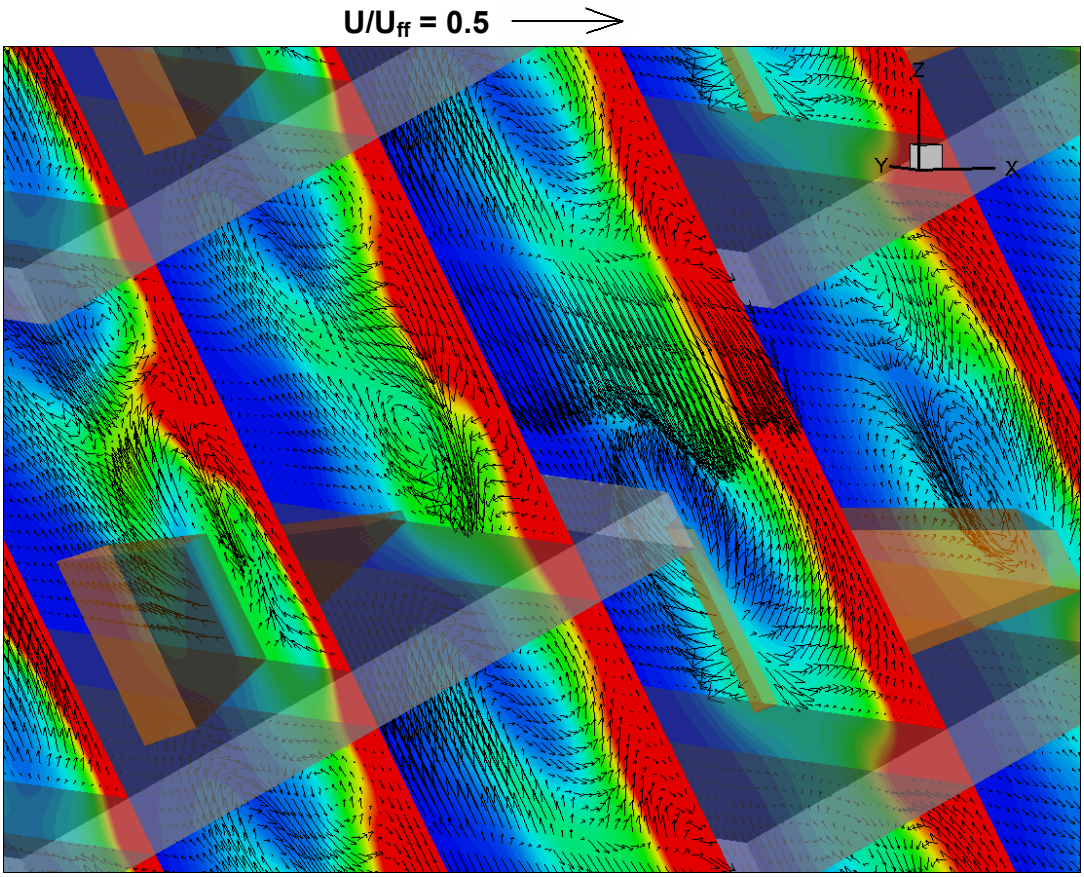

Figure 2.11. Secondary flow vectors showing a winglet forming a vortex in a two-dimensional louvered fin array. Flow is from left to right following the louver direction.

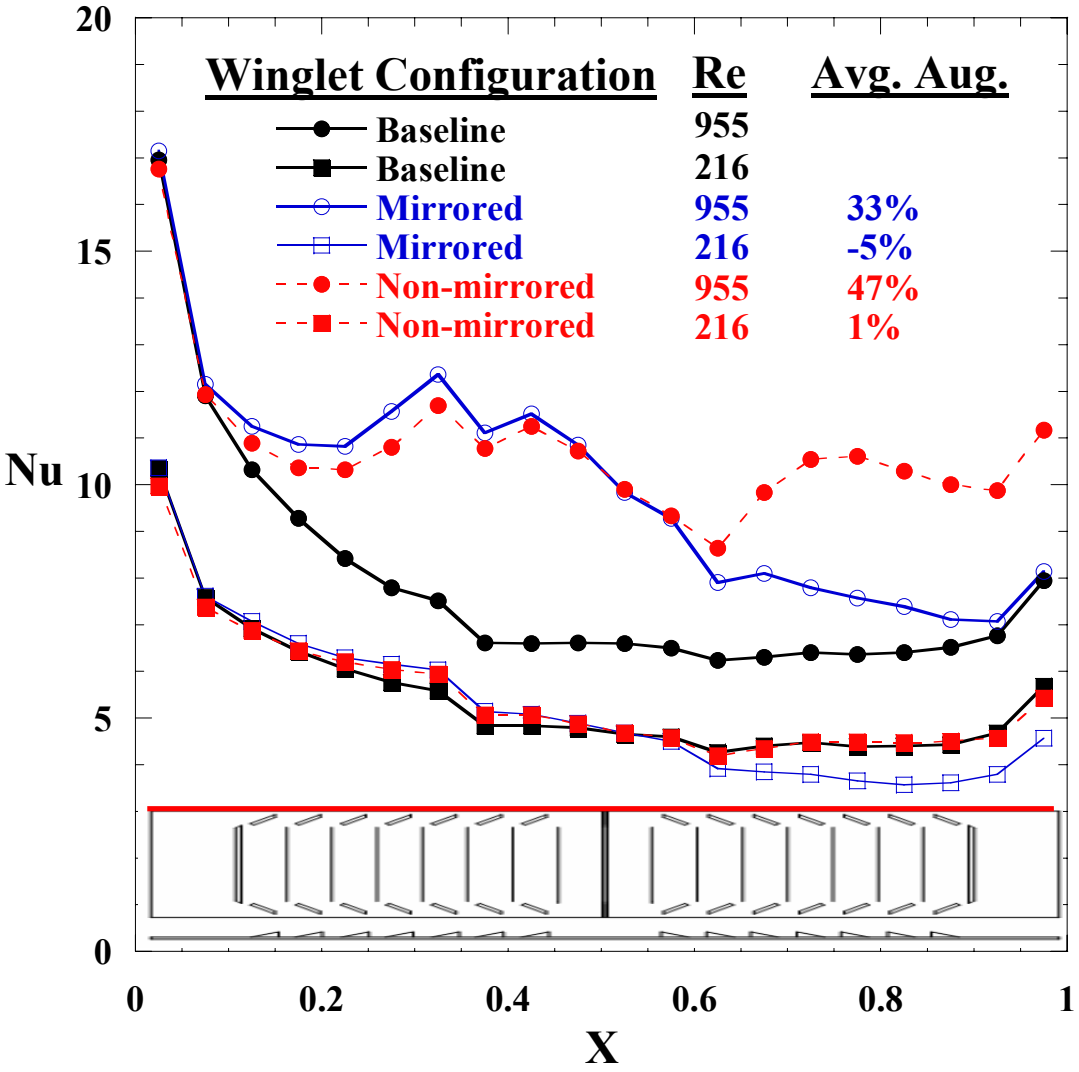

Figure 2.12. Comparison of heat transfer performance between non-mirrored and mirrored winglet configurations. Parameters for these tests were: $\alpha = 40°$, $\Lambda = 1.5$, $t_w = t$ using 28 winglets. For the non-mirrored test Z = 0.22, and for the mirrored test Z = 0.15. Note that the winglet setup shown is for the mirrored configuration.

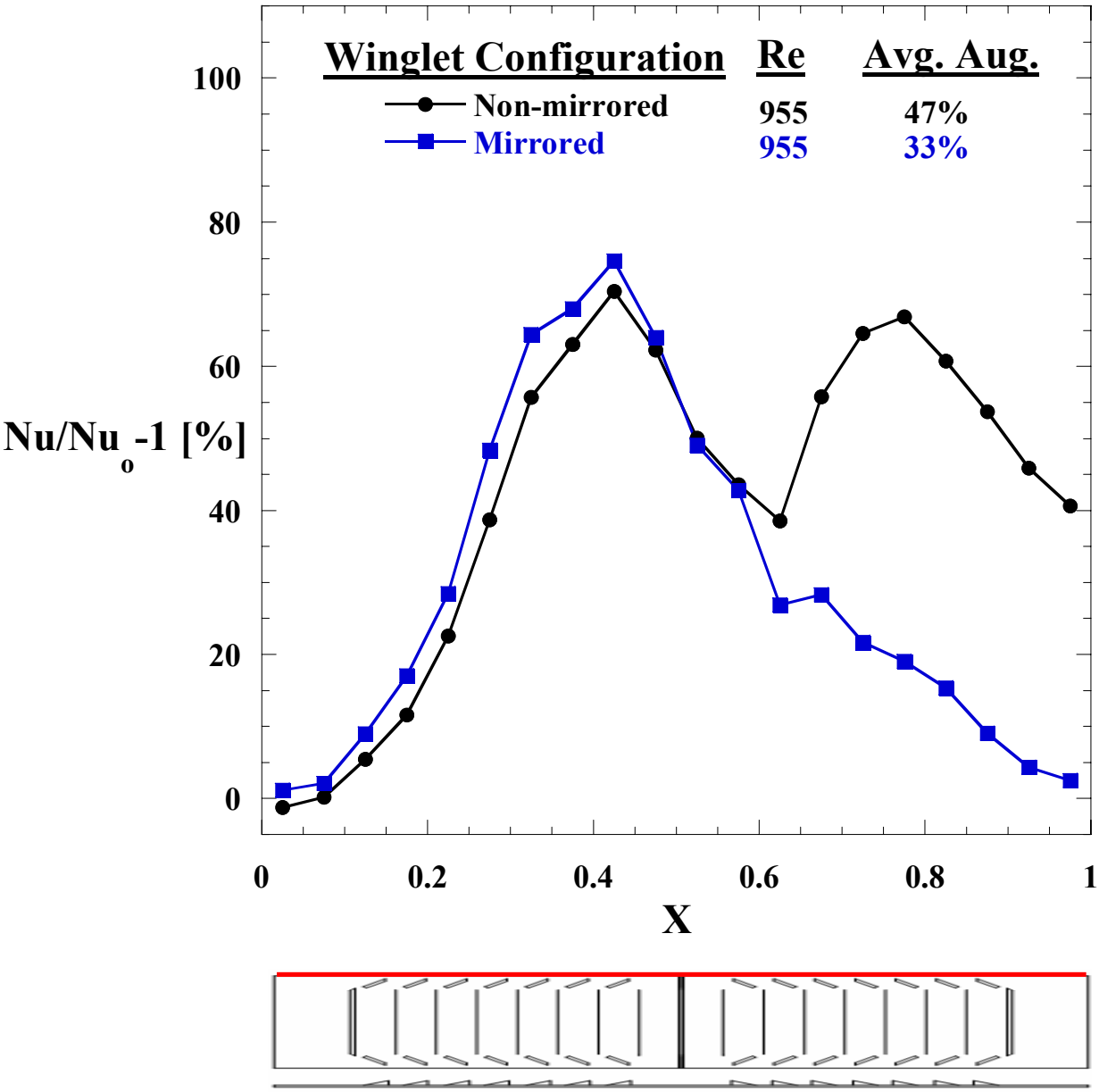

Figure 2.13. Nusselt number augmentations along the tube wall for non-mirrored and mirrored winglet configurations at Re = 955. Parameters for the tests were the same as Figure 2.12.

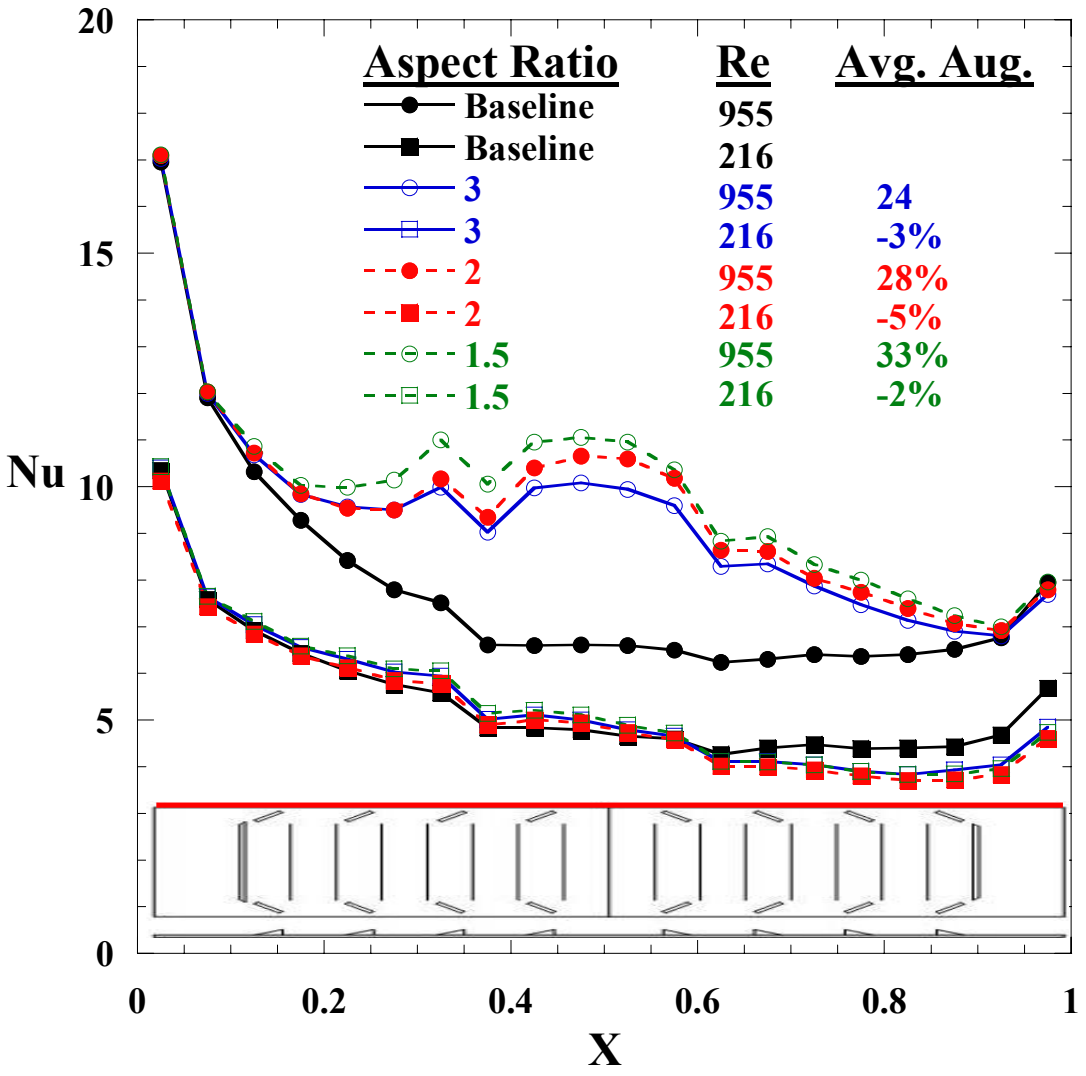

Figure 2.14. Comparison of heat transfer performance between winglets configurations of different aspect ratios. Parameters for the tests were: $\alpha = 40°$, $Z = 0.22$, $t_w = 0.03t$, using 16 winglets.

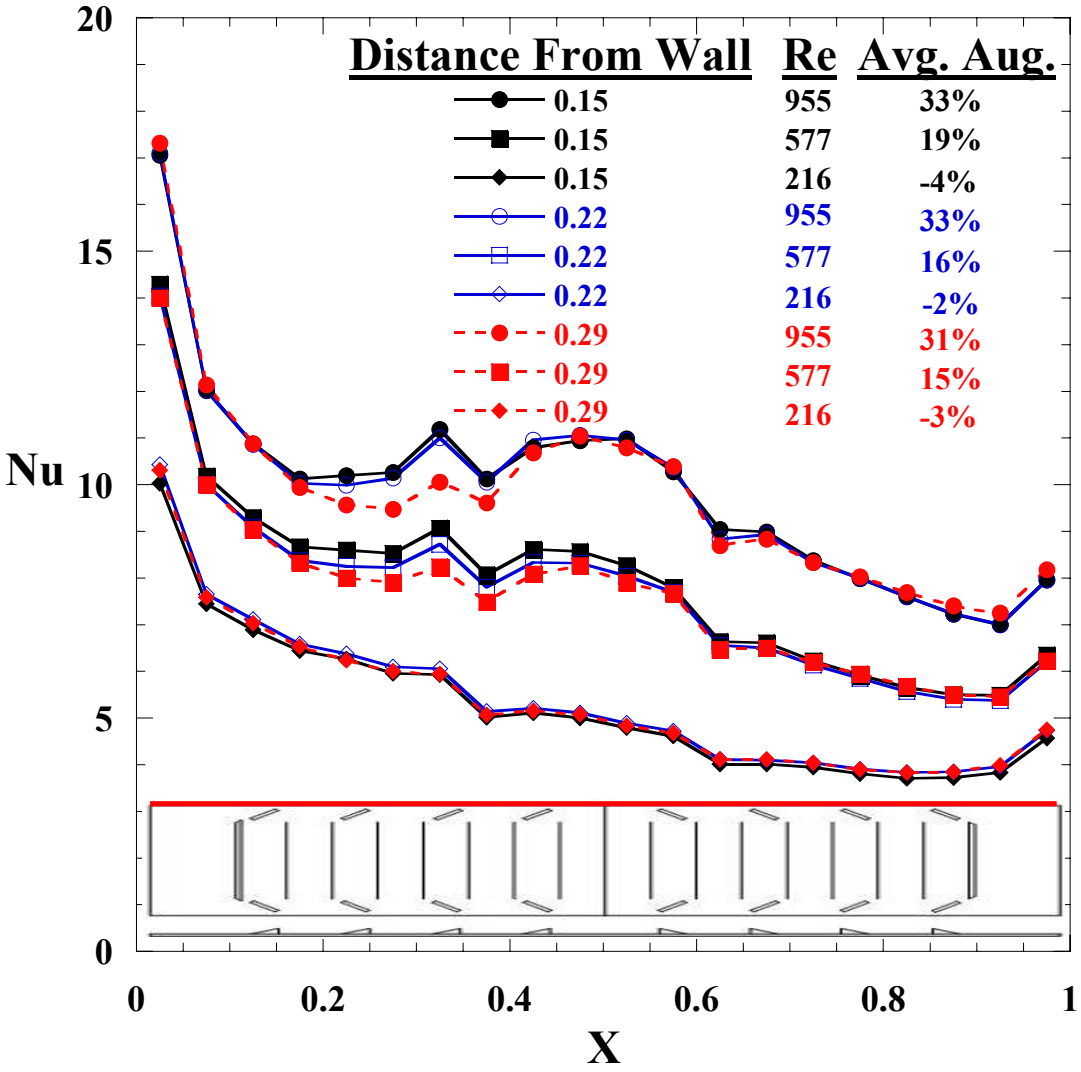

Figure 2.15. Comparison of heat transfer performance between winglet configurations having different distances from the tube wall. Parameters for the tests were: $\alpha = 40°$, $\Lambda = 1.5$, $t_w = 0.03t$, using 16 winglets.

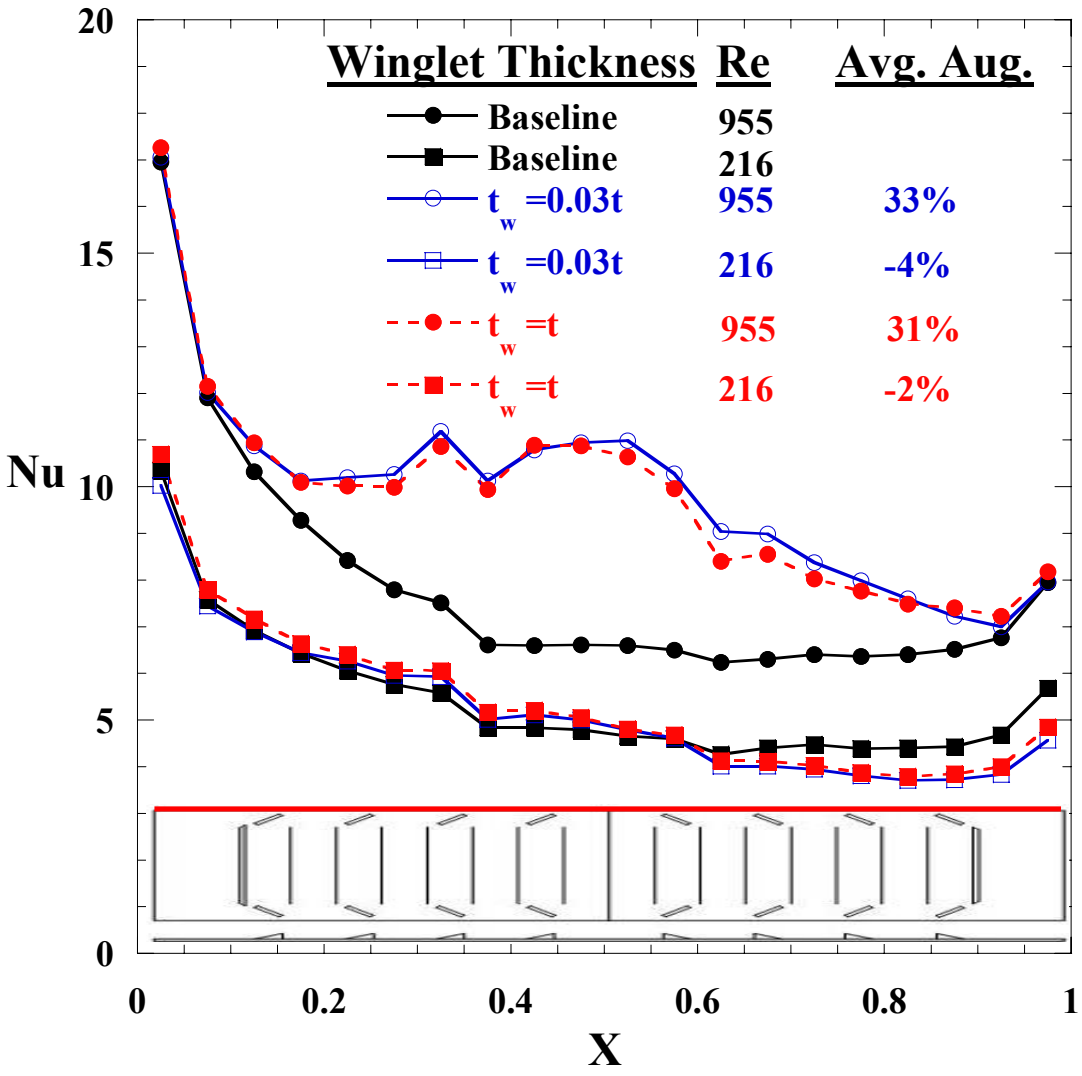

Figure 2.16. Comparison of heat transfer performance between winglet configurations having different winglet thicknesses. Parameters for tests were: $\alpha = 40°$, $\Lambda = 1.5$, $Z = 0.15$, using 16 winglets.

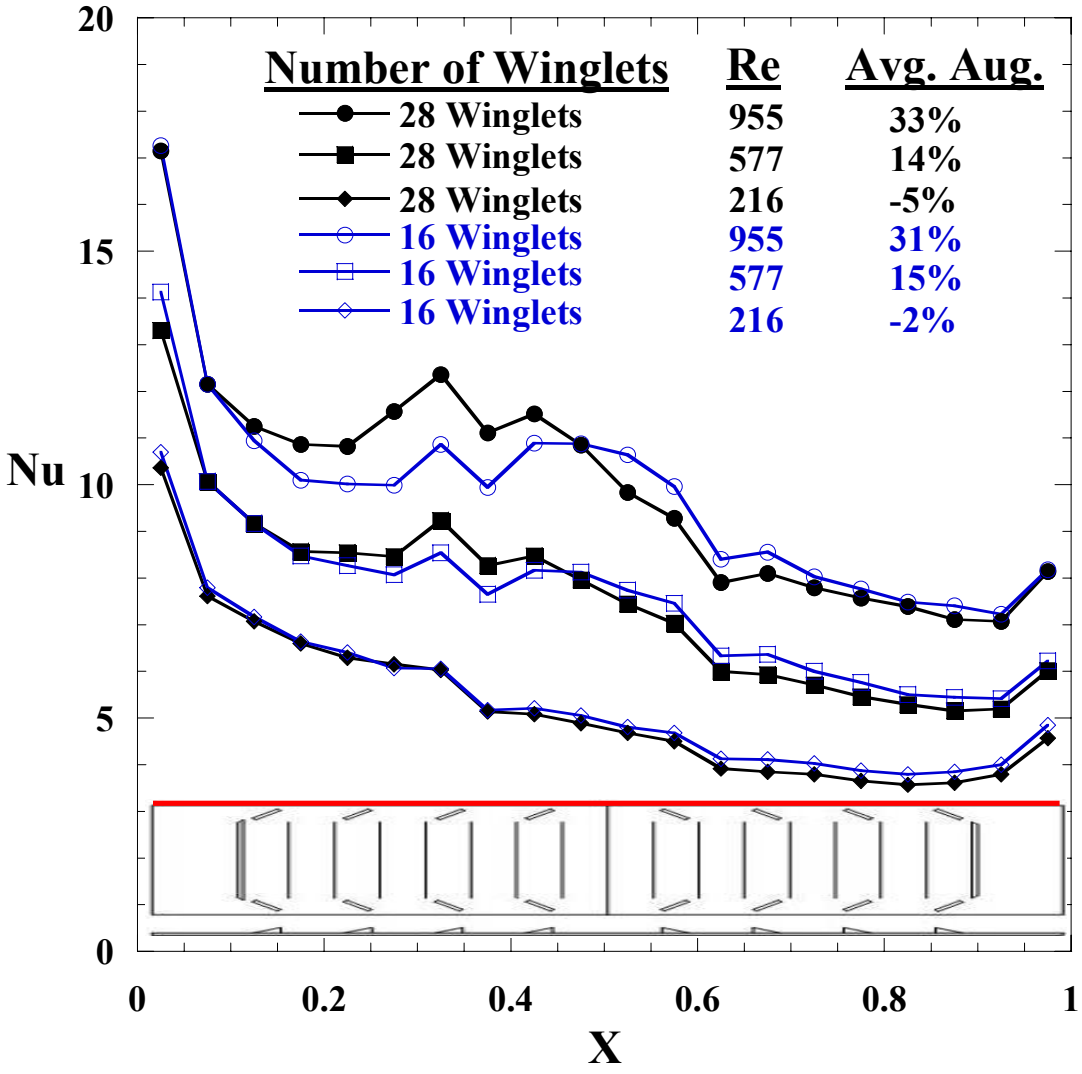

Figure 2.17. Comparison of heat transfer performance between 28 and 16 winglet configurations. Parameters for the tests were: $\alpha = 40°$, $\Lambda = 1.5$, $Z = 0.15$, and $t_w = t$. Note that the winglet configuration diagram shown is for the 16 winglet configuration.

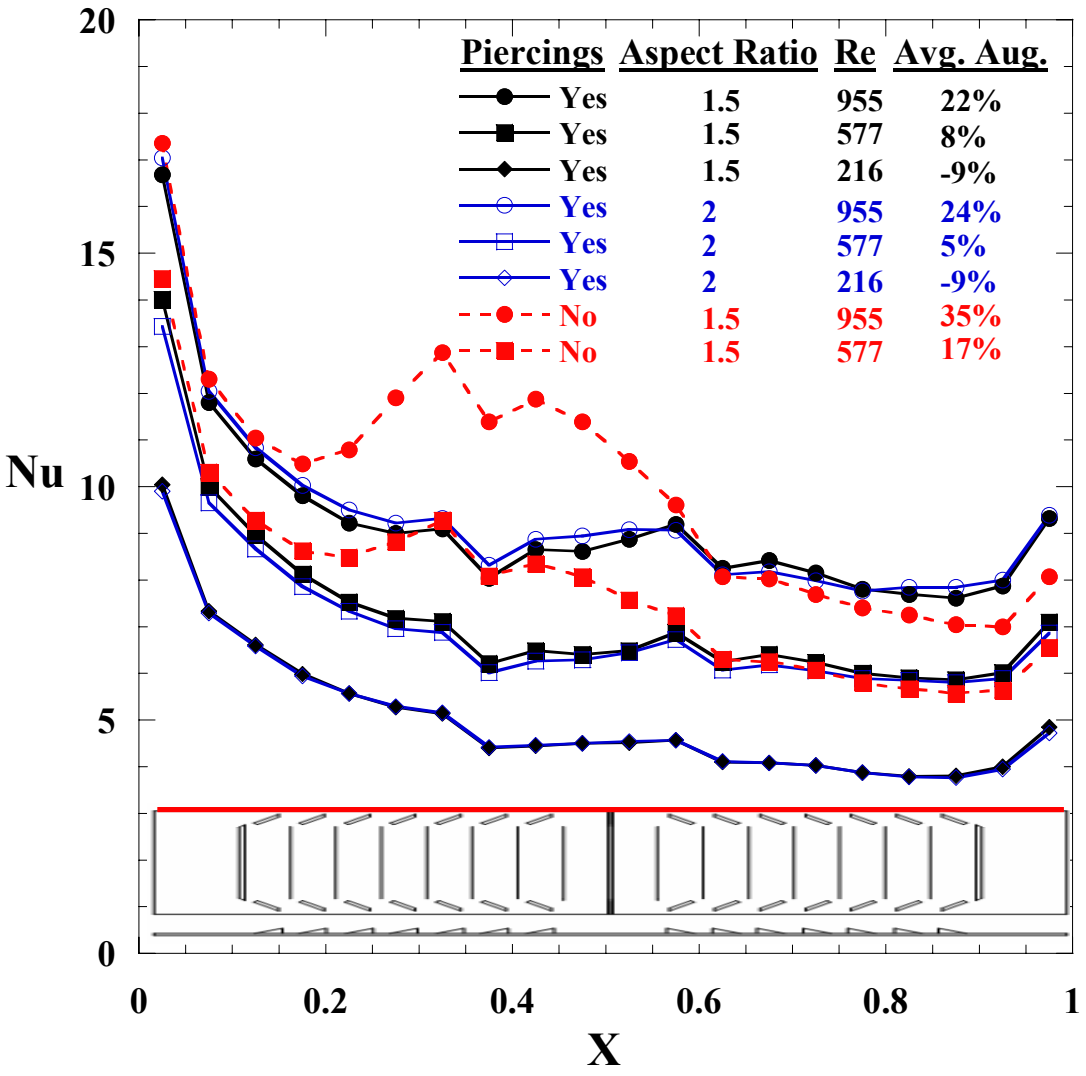

Figure 2.18. Comparison of heat transfer performance between pierced and solid fin winglet configurations. Parameters for the tests were: $\alpha = 30°$, $Z = 0.15$, $t_w = t$, using 28 winglets.

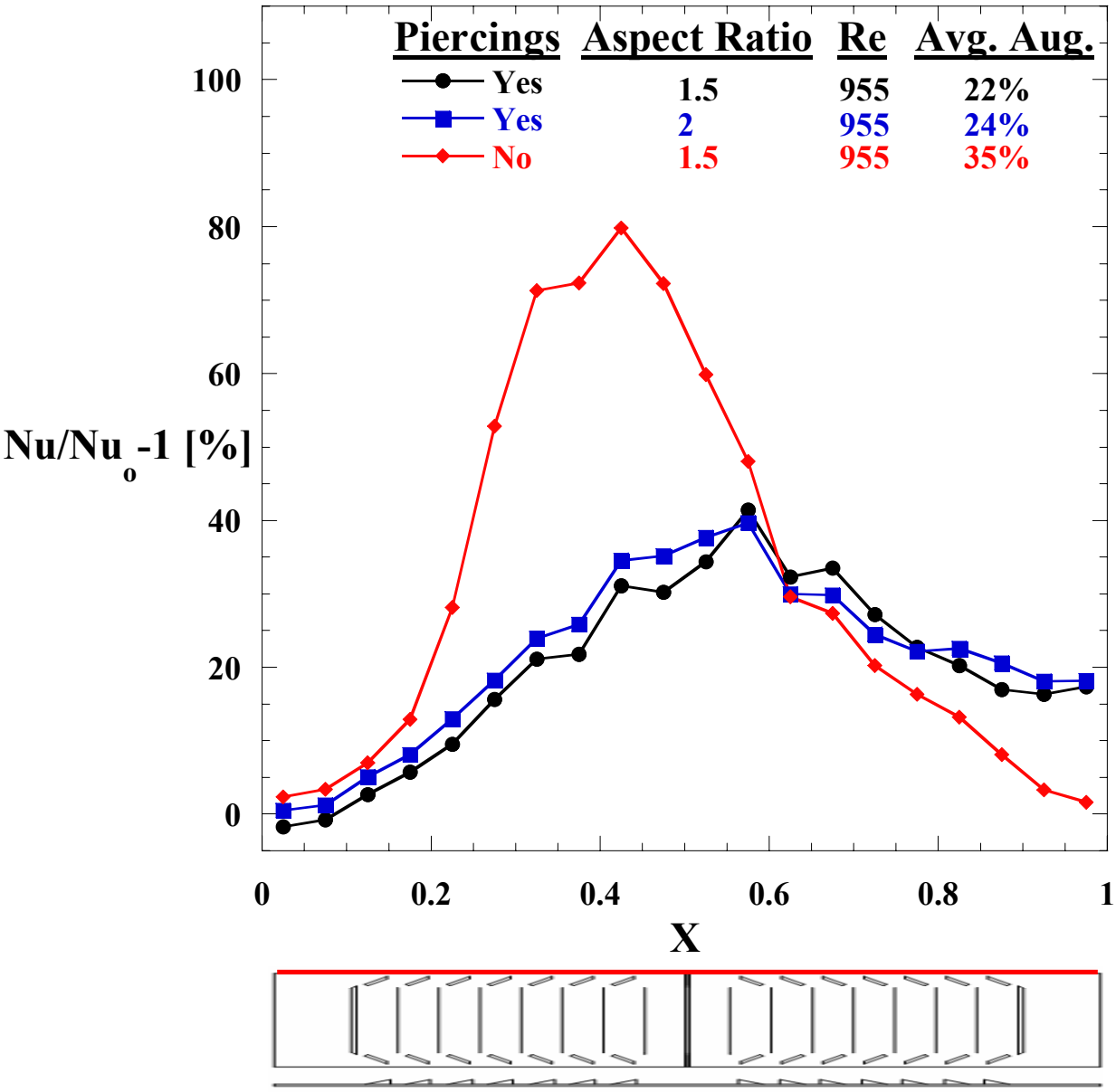

Figure 2.19. Nusselt number augmentations for pierced and solid louvered fin configurations at Re = 955. Parameters for the tests were: $\alpha = 30°$, $Z = 0.15$, $t_w = t$, using 28 winglets.

Appendix A
Introduction

This study has focused on practical applications of delta winglets in compact louvered fin heat exchangers. Figure A1 shows a louvered fin heat exchanger typical of those used in automotive radiators. Air-side resistance on the louvered fin and tube wall surfaces comprises 85% of the total resistance to heat transfer. The tube wall is considered the primary surface for heat transfer where the temperature difference with the free stream air passing through the heat exchanger is at a maximum. To increase overall heat transfer efficiency, this study has attempted to determine a manufacturable delta winglet configuration to maximize tube wall heat transfer.

The two papers included in this thesis do not contain all of the experimental data collected. The following Appendices contain details on experimental facilities and methodology, as well as a comprehensive data summary on all winglet configurations tested. Appendix B discusses the test rig, louver and winglet geometry, instrumentation, and data analysis techniques. Heat transfer and pressure drop results in the form of Nusselt numbers and friction factors are reported in Appendix C. Appendix D discusses the overall conclusions reached in this study and makes recommendations for possible future work on delta winglets in louvered fin heat exchangers.

A.1 Nomenclature

A_{ff}	Minimum cross sectional free flow area
A_{heater}	Area of tube wall heater
A_{in}	Cross sectional area of test section inlet
b	Half of winglet height
c	Winglet chord
D_H	Hydraulic diameter
F	View factor
f	Fanning friction factor
f_0	Baseline friction factor
f_{aug}	Friction factor augmentation
F_d	Fin depth, distance from leading edge of entrance louver to trailing edge of turnover louver
F_h	Fin Height
F_p	Fin pitch
I_{heater}	Current through strip heater
k	Thermal conductivity
K_c	Loss coefficient for sudden contraction of flow entering louvered array
K_e	Loss coefficient for sudden expansion of flow leaving louvered array
L	Material lengths
L_l	Louver length
L_p	Louver Pitch
n_{louver}	Number of louver rows at inlet of test section
Nu_0	Baseline Nusselt number
Nu_{aug}	Nusselt augmentation, $Nu_{aug} = \overline{Nu/Nu_0 - 1}$
Nu	Nusselt number
P_{wetted}	Wetted perimeter, $P_{wetted} = 2(F_p\text{-}t) + 2F_h$
Q	Volumetric flow rate through test section
$q''_{conduction}$	Heat flux lost by conduction through instrumented wall
q''_{heater}	Applied heat flux at heated wall

$q''_{radiation}$	Heat flux lost by radiation from the heated wall
Re_{Lp}	Reynolds number based on louver pitch, $Re_{Lp} = U_{ff}L_p/\nu$
R_{heater}	Resistance of constant heat flux heater
R_p	Resistance of precision resistor
t	Louver thickness
t_w	Louver thickness
T_{film}	Film temperature
T_{guard}	Temperature measured on guard heater plate
T_{inlet}	Temperature measured at test section inlet
T_{wall}	Temperature measured on heated wall
U_{ff}	Maximum free flow velocity
VG-F	Forwards facing delta winglet
VG-B	Backwards facing delta winglet
V_{heater}	Voltage drop across kapton/inconel heater
V_p	Voltage drop across precision resistor
w	Louver width
x	Horizontal coordinate through test facility
X	Non-dimensional fin depth
z	Distance of delta winglet from the tube wall
Z	Non-dimensional distance of delta winglet from the tube wall, $Z = z/L_p$

Greek

α	Delta winglet angle of attack
Λ	Delta winglet aspect ratio, $\Lambda = 2b/c$
θ	Louver angle
ΔP	Pressure drop through louvered array
ε	Surface emissivity
ρ_{air}	Density of air
ν	Kinematic viscosity
σ	Stefan-Boltzman constant

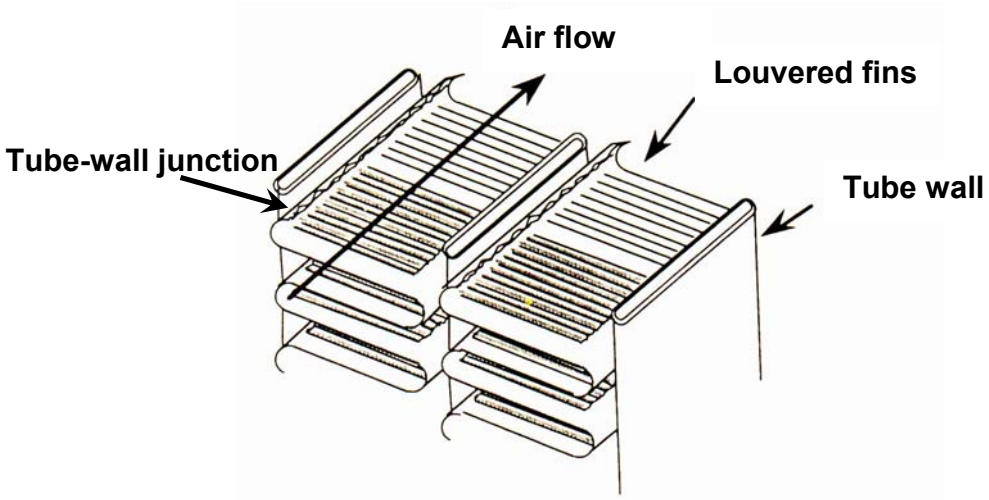

Figure A1. Louvered fin heat exchanger showing the location of the tube-wall junction.

Appendix B

Experimental Facility and Data Analysis Techniques

(Partially Adapted from Sanders [E.1])

This section details the different louver, winglet, and piercing geometries tested. In addition, the wind tunnel, test section, instrumentation, and data acquisition hardware used for all experiments are described. Methods of data collection, reduction, and uncertainty estimation are also outlined.

B.1 Louver Geometry and Modifications

The three-dimensional fins were specially fabricated at a 20:1 scale by a molding process. The mold for the fins was made at Prototype Techniques through the use of stereolithography. The fins, seen in Figure B1, were delivered in pieces that were half of the test section length. Each piece formed the entrance louver, seven normal louvers, and half of the turnover louver (or half of the turnover, seven normal louvers, and the exit louver, if turned 180˚). Figure B2 shows the specific geometry of the louver pattern used in this study. One forward facing fin and one backward facing fin completed a full fin row. The fins were not constructed to be inserted directly in the test section. To be centered in the test section, one side was kept long to slide into the milled wall while the other side had to be cut due to the protrusion of the brackets (the milled wall and brackets will be discussed in the next section). Once the cut was made, the louvers were centered in the test section. The fins were spray painted silver (Premium Décor PDS-94 Chrome) to reduce radiation loss from the wall. Due to the low thermal conductivity of the louvered fins, the junction between the fins and the heated tube wall was considered adiabatic.

Two different three-dimensional geometries were molded for testing. The louver pattern for both was the same as in Figure B2 with the only difference between the two being louver length. Louver lengths of 70% and 82% of the total fin depth were used for testing and are shown in Figure B3. The 82% geometry is representative of an actual louvered fin heat exchanger core. The 70% geometry was made to accommodate winglets on the flat landings near the tube wall as a possible design to be used in future heat exchangers.

To accommodate simulated piercings, the louvered fins were modified. Fourteen square cutouts were machined into the flat landing of each half fin (28 cutouts per fin) to allow for

inserts simulating piercings to be taped into the louvered fins. Cutout dimensions are shown in Figure B4. Dimensions were made as large as possible while maintaining the structural integrity of the louvered fins.

B.2 Winglet and Piercing Geometries

Several winglet and piercing geometries were tested. The winglet parameters that were varied included aspect ratio, non-dimensional distance form tube wall, angle of attack, and winglet thickness. Figure B5 presents the winglet parameters that were varied during testing. Winglets were also tested in the forwards (VG-F) and backwards (VG-B) directions as shown in Figure B6.

Winglet aspect ratio was varied between 1.5 and 3. Note that for all tests the winglet height was fixed at $0.35F_p$. Three different non-dimensional winglet distances from the tube wall of 0.15, 0.22, and 0.29 were tested. In addition, three different winglet thicknesses were tested that included thin winglets having a thickness of 0.03t, as well as realistically thick winglets that had thicknesses approximately equal to the louver thickness (0.67t and 0.95t). The realistic thicknesses were representative of winglets that would result from the stamping process during manufacturing.

A laser was used to make inserts with piercings (see Figure B7) that simulated winglet stampings, which fit into the cutouts. Inserts were secured into the cutouts and winglets were placed in the appropriate location. Inserts allowed for a range of piercing locations and winglet geometries to be tested, however, there were some geometric limitations. VG-F winglets could only be tested with downstream piercings. Testing VG-F with upstream piercings would result in the piercing not fitting onto the cutout as shown in Figure B7. VG-B winglets were able to be tested with both upstream and downstream piercings. Piercings were only simulated using winglets with a thickness of the louvered fins (0.95t) as this is the thickness that would result from the stamping process.

B.3 Wind Tunnel Design

The test facility used in this study was an open loop wind tunnel that consisted of an inlet nozzle, a test section, a laminar flow element, and a motor-controlled blower as shown in Figure B8. All of the major components in the test facility were the same used in the studies of Sanders

[E.1], Lyman et al. [E.2], Stephan and Thole [E.3], and Ebeling and Thole [E.4] and Sanders and Thole [E.5], with the exception of the test section.

The inlet contraction was designed by Lyman [E.6] using Fluent 5.0. The contraction was designed to provide a uniform inlet flow to the test section so that an infinite stack of louvers could be modeled as accurately as possible. The nozzle had a 16:1 area reduction, decreasing from an inlet area of 6.57 ft^2 (0.61 m^2) to an exit area, or test section inlet area (A_{in}), of 0.41 ft^2 (0.038m^2). There was a 2.01 in (51 mm) thick piece of aluminum honeycomb and a window screen at the inlet of the nozzle for flow uniformity.

Air was pulled through the test rig with a Dayton 3N1786 1.5 hp, 3-phase motor powering a Dayton 4C108 centrifugal fan. The fan speed was controlled with a 60 Hz Dayton 3HX72 AC inverter. The smallest increment of the inverter was 0.01 Hz which produced flow changes that were within the uncertainty of the pressure transducer mentioned earlier.

B.4 Test Section Design

The test section, shown in Figure B9, was comprised of 12 louvered fin rows, a constant heat flux heater, bounding walls, a conduction guard heater, thermocouples imbedded behind the heated tube wall and on the guard heater, and pressure taps $0.73L_p$ up and downstream of the louvered fin array. The test section was designed and built to accommodate the three-dimensional fins provided by Modine. The conduction guard heater assembly is not shown in the Figure B9, but for testing it was placed behind the constant heat flux heater and had thermocouples in the same relative locations as the heated tube wall.

The constant heat flux heater was a custom kapton and inconel design made by Electrofilm Manufacturing Co. and is shown in Figure B10. The heater was made by sandwiching a winding strip of inconel between layers of kapton. Approximately 15.67 ft (4.78 m) of 0.22 in wide inconel was used at 0.19 Ω/ft unit resistance, giving an overall heater resistance of 2.94 Ω. On one side of the heater, a very thin copper surface was added to help spread the heat between the gaps in the inconel. The heater had a maximum heat flux of 310 W/m^2 which was high enough to produce the needed flux for the highest Reynolds number tested. The reflective copper surface had an emissivity of $\varepsilon = 0.10$. The heater was adhered to the instrumented lexan wall with 3M 401B double sided paper tape of thickness 0.003 in (0.08 mm).

Louvers were held in place in the test section by milled slots in the lexan wall and brackets on the heated wall. Brackets were placed in rows of fin pitch spacing that stretched the length of the heater as seen in Figure B11. As shown in Figure B12, the slots on the milled wall started at the test section inlet and ended at the rear of the heater.

The flow through the realistic fin array had two distinct regions: louver-directed flow that would turn at the entrance, turnover, and exit louvers, and channel-directed flow on the flat landings that would continue straight through the test section without turning. It was important to allow each of these flow regions to take a periodic course as would occur in a real heat exchanger. To facilitate this, the bottom and top walls were made to angle only over the louver length while the sides remained flat and straight as seen in Figure B13. When the $L_l/F_h = 82\%$ louver length fins were used, two extra pieces were attached to the outside of the 70% bottom wall to provide the necessary extra width. Figure B14 shows the side piece additions and their orientation with respect to the bottom wall. The top wall was shaped to allow the louver directed flow to follow a periodic flow path, however, the flat landings of the fins placed within the angled portions of the top flow wall were blocked to allow only louver directed flow as shown by Figure B15. This was done because there was no inlet air to these fins to produce a flat landing flow. The flat landings were blocked off using 1 in (25.4 mm) thick foam cut to fit a particular louver length and fin. Both walls were made less than the channel width to allow room for adhesive-backed 0.19 in (0.48 mm) thick rubber on either side that prevented air leaks from the channel(see Figure B11).

B.5 Instrumentation

Flow through the tunnel was measured by a Meriam 50MC2-2 laminar flow element (LFE). The LFE was capable of measuring a maximum volumetric flow rate of 2.79 m^3/min with a corresponding pressure drop of 203 mm H_20. By measuring the pressure drop across the LFE and using a pressure drop to flow rate correlation given by the manufacturer, the volumetric flow rate (Q) through the tunnel could be determined. The volumetric flow rate was used in the Reynolds number calculation,

$$Re_{L_p} = \frac{L_p Q/A_{ff}}{\nu} \qquad \text{(B1)}$$

A_{ff} was defined as,

$$A_{ff} = A_{in} - t \cdot F_h \cdot n_{louver} \quad \text{(B2)}$$

Volumetric flow rates were set for desired Reynolds numbers. For this study, the desired Reynolds numbers were Re = 216, 577, and 955, chosen to match a range of important driving speeds at which a radiator would perform. The pressure drop across the LFE was measured with a Setra model 264, 0 to 5 in H_2O pressure transducer which had an accuracy of 0.25 % full scale value (FSV). A full description of the measurement devices and techniques will be given in a later section. Pressure drop measurements through the test sections are made with a Setra model 264, 0 to 0.1 in H_2O pressure transducer.

Type E thermocouples were used for all tube wall temperature measurements. Twenty thermocouples were imbedded behind the tube wall heater. Thermocouples were placed in an area where periodic flow has been shown to occur, as shown in Figure B16. Thermocouples were also placed one fin pitch above and below the center channel thermocouples at the locations to check for heat transfer periodicity along the tube wall. To measure conduction losses through the back of the heated tube wall thermocouples were placed on the guard heater assembly at locations corresponding to the location of tube wall thermocouples.

B.6 Data Acquisition Hardware and Techniques

The data acquisition hardware used was a SCXI-1000 chassis into which three SCXI-1102 modules and one SCXI-1100 module were inserted. The SCXI-1102 modules were coupled with SCXI-1303 terminal blocks which were made for thermocouple readings and provided cold junction temperature compensation for more accurate measurements. An SCXI-1300 was inserted into the SCXI-1100 module for pressure transducer, tube wall heater, and conduction guard heater voltage measurements. The chassis was connected to a 16 bit PCI-MIO-16XE-50 DAQ card. Codes were written in LabView 7.0 to acquire temperature and pressure drop measurements. One code was written to obtain thermocouple readings, the LFE pressure drop, and the voltages from the tube wall and conduction guard heaters. A separate code was written to collect pressure drop measurements through the channel.

Once the tunnel was at steady state, 200 temperature measurements were taken and averaged at each of the center channel thermocouple locations. Steady state was determined by

taking temperature measurements at one, two, three, four, and five hours and comparing the average Nusselt numbers at a given hour with the previous hour using the following equation:

$$Nu_{\%difference} = \frac{Nu - Nu_{previoushour}}{Nu_{previoushour}} \tag{B3}$$

Steady state was chosen as four hours because there was generally a less than 1% difference in average Nusselt number from four to five hours. Much care was taken to obtain data at the four hour mark and results were very repeatable. Once all temperatures, heater voltages, and the LFE pressure drops were collected, they were written to a computer file for later use in calculating the test Reynolds number and Nusselt numbers.

To obtain pressure drop measurements through the louvered array and the LFE, 9000 and 500 samples, respectively, were taken and averaged. Pressure transducers were re-zeroed daily because room temperature varied daily which affected the zero point. All pressure drop measurements were completed with the heaters turned off to avoid other complications with air temperature. Reynolds numbers for the pressure drop measurements were matched to within Re = ±0.5 of the target Reynolds number before data was collected.

B.7 Data Reduction

The previous section described the methods used to collect the temperature and pressure drop measurements. This section will detail the steps taken to convert raw data into Nusselt numbers and friction factors, and define how heat transfer and friction factor augmentations were determined.

The heat transfer data were divided into two parts: localized Nusselt numbers at each of the thermocouple locations and an averaged Nusselt augmentation percentage for the winglet tests. To isolate the convective heat transfer coefficient at a given location, the losses due to conduction through the instrumented wall and radiation from the heater had to be accounted for. Therefore, the Nusselt number at each discrete location was defined as

$$Nu(X) = \frac{q''_{heater} - q''_{conduction}(X) - q''_{radiation}(X)}{T_{wall}(X) - T_{inlet}} \frac{L_p}{k_{air}} \tag{B4}$$

where,

$$q''_{heater} = \frac{I_{heater} V_{heater}}{A_{heater}} \tag{B5}$$

$$q''_{conduction}(X) = \frac{T_{wall}(X) - T_{guard}(X)}{L_{lexan}/k_{lexan} + L_{foam}/k_{foam}} \tag{B6}$$

$$q''_{radiation}(X) = \frac{\sigma(T_1(X)^4 - T_2{}^4)}{\frac{1-\varepsilon_1}{\varepsilon_1} + \frac{1}{F_{12}} + \frac{1-\varepsilon_2}{\varepsilon_2}} + 2\left[\frac{\sigma(T_1(X)^4 - T_3{}^4)}{\frac{1-\varepsilon_1}{\varepsilon_1} + \frac{1}{F_{13}} + \frac{1-\varepsilon_3}{\varepsilon_3}}\right] \tag{B7}$$

The thermal conductivity and viscosity of air was interpolated using the film temperature, T_{film}, defined as:

$$T_{film} = \frac{\frac{T_{wall}(X=0) + T_{inlet}}{2} + \frac{T_{wall}(X=1) + T_{inlet}}{2}}{2} \tag{B8}$$

Equation B8 is based on a flat plate boundary layer formulation which applies because the boundary layers from the heated wall and the milled wall do not meet.

Equation B7 is a radiation network equation applied to the test section setup. In equation B7, subscript 1 refers to the heated wall, subscript 2 refers to the milled wall, and subscript 3 refers to the fin surface. For this calculation, T_2 and T_3 were assumed equal to the inlet temperature. The view factors F_{12} and F_{13} were found using the view factor equations in Modest [E.7] as well as the law of reciprocity. F_{12} and F_{31} were defined as

$$F_{12} = (1 + H^2)^{0.5} - H \tag{B9}$$

$$F_{31} = 0.5\left[1 + H_2 - (1 + H_2{}^2)^{0.5}\right] \tag{B10}$$

Where H_2 is the reciprocal of H. Equation B7 was applied at every streamwise thermocouple position to obtain losses at each location.

For each of the louver lengths and Reynolds numbers, baseline heat transfer measurements were taken at each of the 20 center channel thermocouple locations. In order to calculate the overall average Nusselt augmentation, the augmentation at each of the streamwise locations is first determined:

$$Nu_{aug}(X) = \frac{Nu(X) - Nu_0(X)}{Nu_0(X)} = \frac{Nu(X)}{Nu_0(X)} - 1 \tag{B11}$$

where Nu_0 refers to baseline Nusselt number. The $Nu_{aug}(X)$ values were then averaged to get the overall average Nusselt augmentation:

$$Nu_{aug} = \overline{Nu_{aug}(X)} \tag{B12}$$

The vast majority of tests did not include winglets on the entrance louver, so the Nusselt numbers at X=0.025 and 0.075 were usually not used in the averages. By excluding these two points, Nu_{aug} only reflects the average over the winglet affected region.

The pressure drop measurements through the array were converted to Fanning friction factors with the following equation,

$$f = \frac{D_H}{4F_d}\left(\frac{2\Delta P}{U_{ff}{}^2 \rho_{air}} - K_c - K_e\right) \tag{B13}$$

where K_c and K_e are loss coefficients of the sudden contraction and expansion associated with the air entering and leaving the finned array. Both coefficients were found to be 0.03 by using a duct area reduction and expansion chart (White [E.8]). U_{ff} is the maximum air velocity through

the test section. F_d is the fin depth and is defined by the distance from leading edge of the entrance louver to the trailing edge of the exit louver. The hydraulic diameter, D_H, is defined as,

$$D_H = \frac{4 \cdot A_{ff}}{P_{wetted}} = \frac{4(F_p - t)F_h}{2(F_p - t) + 2F_h} \tag{B14}$$

Friction factor augmentation was simply defined as,

$$f_{aug} = \frac{f - f_0}{f_0} = \frac{f}{f_0} - 1 \tag{B15}$$

where f_0 was the baseline friction factor.

B.8 Experimental Uncertainty Estimates

The uncertainties of experimental Nusselt numbers, Reynolds numbers, and friction factors were calculated using the method developed by Kline and McClintock [E.9] which is based on the chain rule of differentiation. Consider some quantity y that is a function of several variables

$$y = f(x_1, x_2, x_3, ..., x_n)$$

The error associated with y is given as

$$dy = \left[\left(\frac{\partial y}{\partial x_1} dx_1 \right)^2 + \left(\frac{\partial y}{\partial x_2} dx_2 \right)^2 + ... + \left(\frac{\partial y}{\partial x_n} dx_n \right)^2 \right]^{1/2} \tag{B16}$$

where each of the dx terms is a combination of bias and precision uncertainties. The most basic forms of the Nusselt number, Reynolds number, and friction factor equation were used so that the errors associated with the directly measured quantities could be found. For example, the Nusselt number equation used was,

$$Nu = \frac{\frac{V_p \cdot V_{heater}}{R_p \cdot A_{heater}} - \left[\frac{\sigma \cdot \left(T_{wall}^{\ 4} - T_{inlet}^{\ 4} \right)}{\frac{1-\varepsilon_1}{\varepsilon_1} + \frac{1}{F_{14}} + \frac{1-\varepsilon_4}{\varepsilon_4}} + 2 \cdot \frac{\sigma \cdot \left(T_{wall}^{\ 4} - T_{inlet}^{\ 4} \right)}{\frac{1-\varepsilon_1}{\varepsilon_1} + \frac{1}{F_{13}} + \frac{1-\varepsilon_3}{\varepsilon_3}} \right] - \frac{T_{wall} - T_{guard}}{\frac{L_{lexan}}{k_{lexan}} + \frac{L_{foam}}{k_{foam}}}}{T_{wall} - T_{inlet}} \cdot \frac{L_p}{k_{air}} \tag{B17}$$

The thermal conductivities were the only quantities that were not accounted for in the error analysis because this information was not available.

Basic forms of the friction factor, friction factor augmentation, Reynolds number, average Nusselt augmentation, and efficiency index equations were also found. Table B1 gives uncertainties calculated for the baseline tests at Re = 216 and 955. The Nusselt number uncertainties are given at three discrete locations (X = 0.025, 0.475, and 0.975) to give the range of possible errors. Reynolds number and friction factor are not dependent on streamwise position, therefore there is only one value given for each of these quantities.

Table B1. Representative Uncertainty Estimates for Calculated Values

		Baseline Uncertainties					
		Re = 216			Re = 955		
X		Value	Uncertainty	Uncertainty [%]	Value	Uncertainty	Uncertainty [%]
0.025	Nu_0	10.48	0.67	6.38	16.77	0.77	4.57
0.475		4.83	0.21	4.27	6.58	0.17	2.60
0.975		5.93	0.26	4.44	8.21	0.23	2.83
	f_0	0.19	0.10	51.40	0.06	0.01	8.20

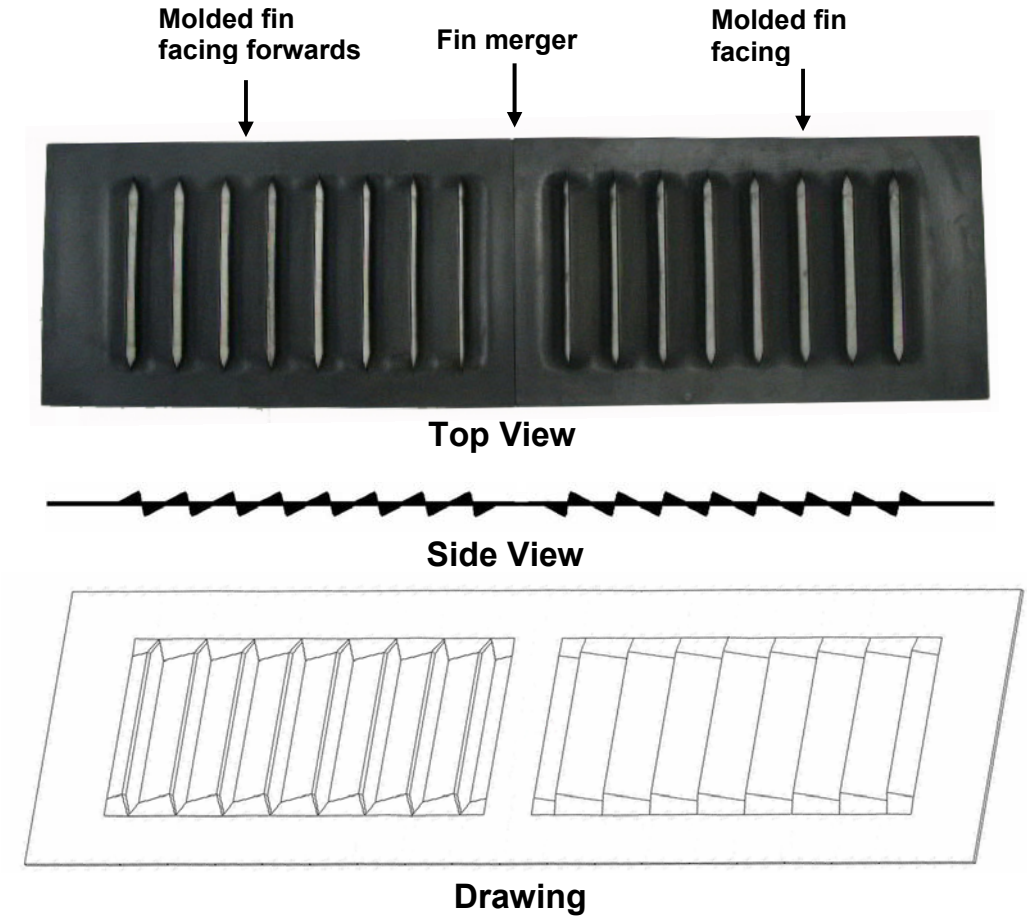

Figure B1. Top view, side view, and drawing of realistic molded fin.

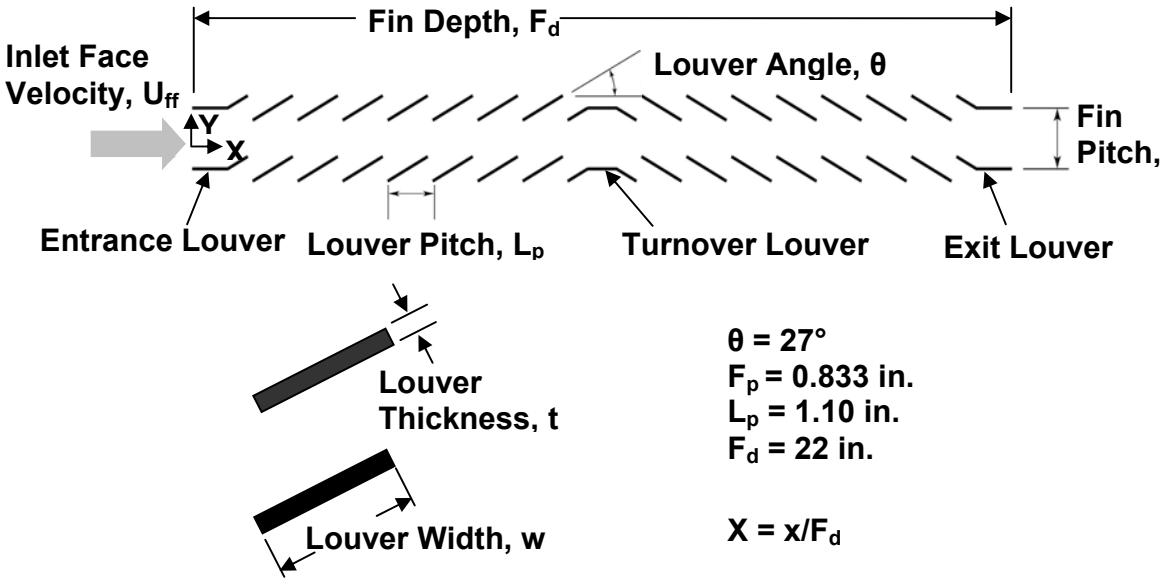

Figure B2. Louver geometry and definitions used in this study.

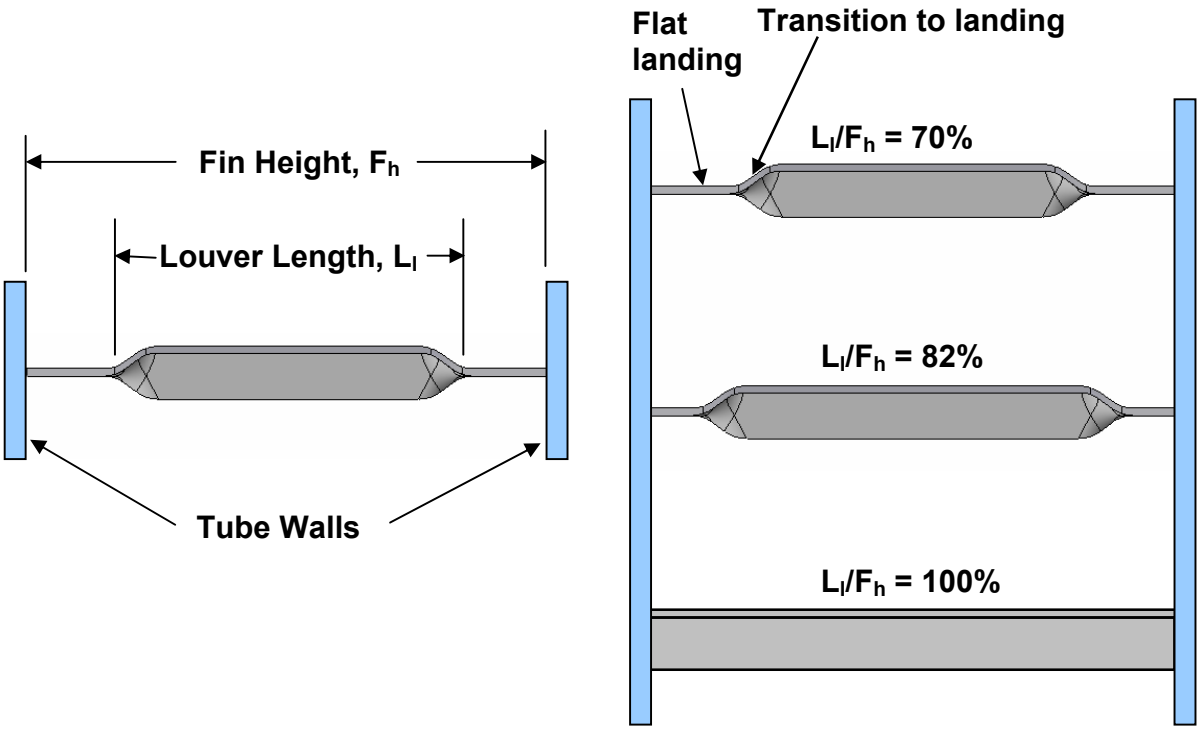

Figure B3. Comparison of different louver lengths and definitions of louvered fin geometries.

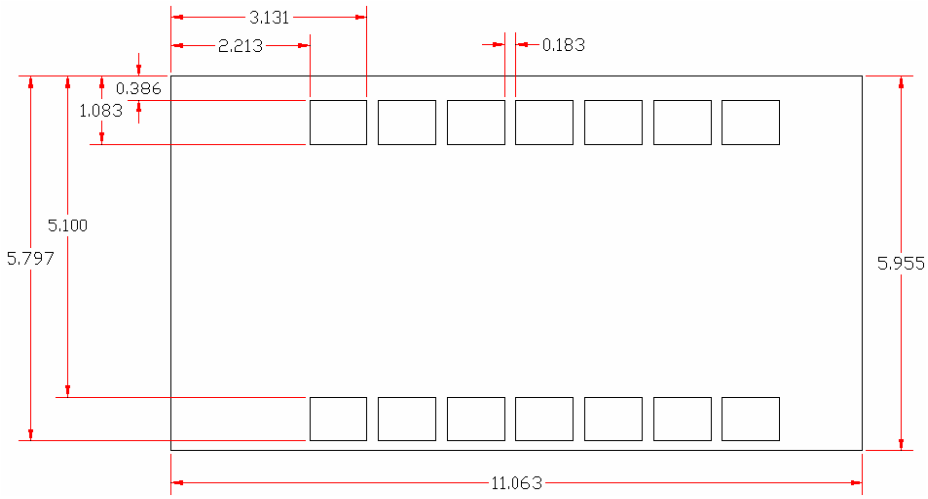

(a)

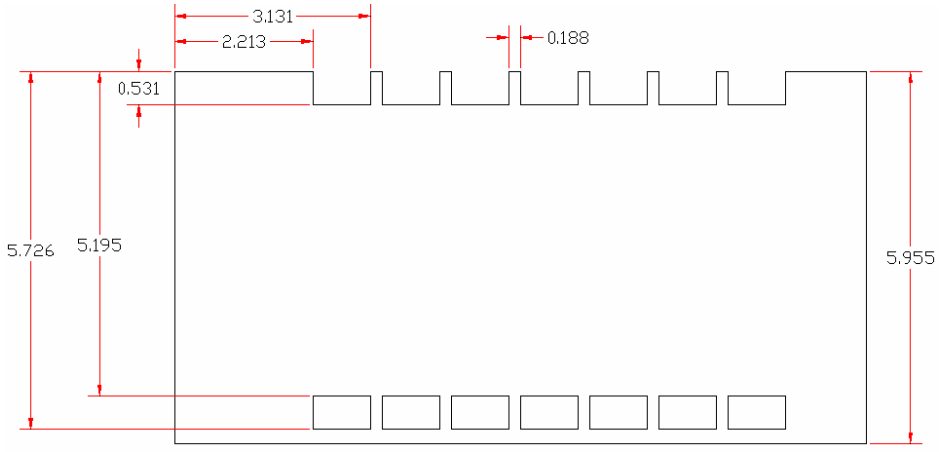

(b)

Figure B4. Modifications made to (a) – the L_l/F_h = 70% louvered fins, dimensions are measured form the uncut edge of the louvered fin, and (b) – the L_l/F_h = 82% louvered fins, dimensions are measured from the cut edge of the louvered fins.

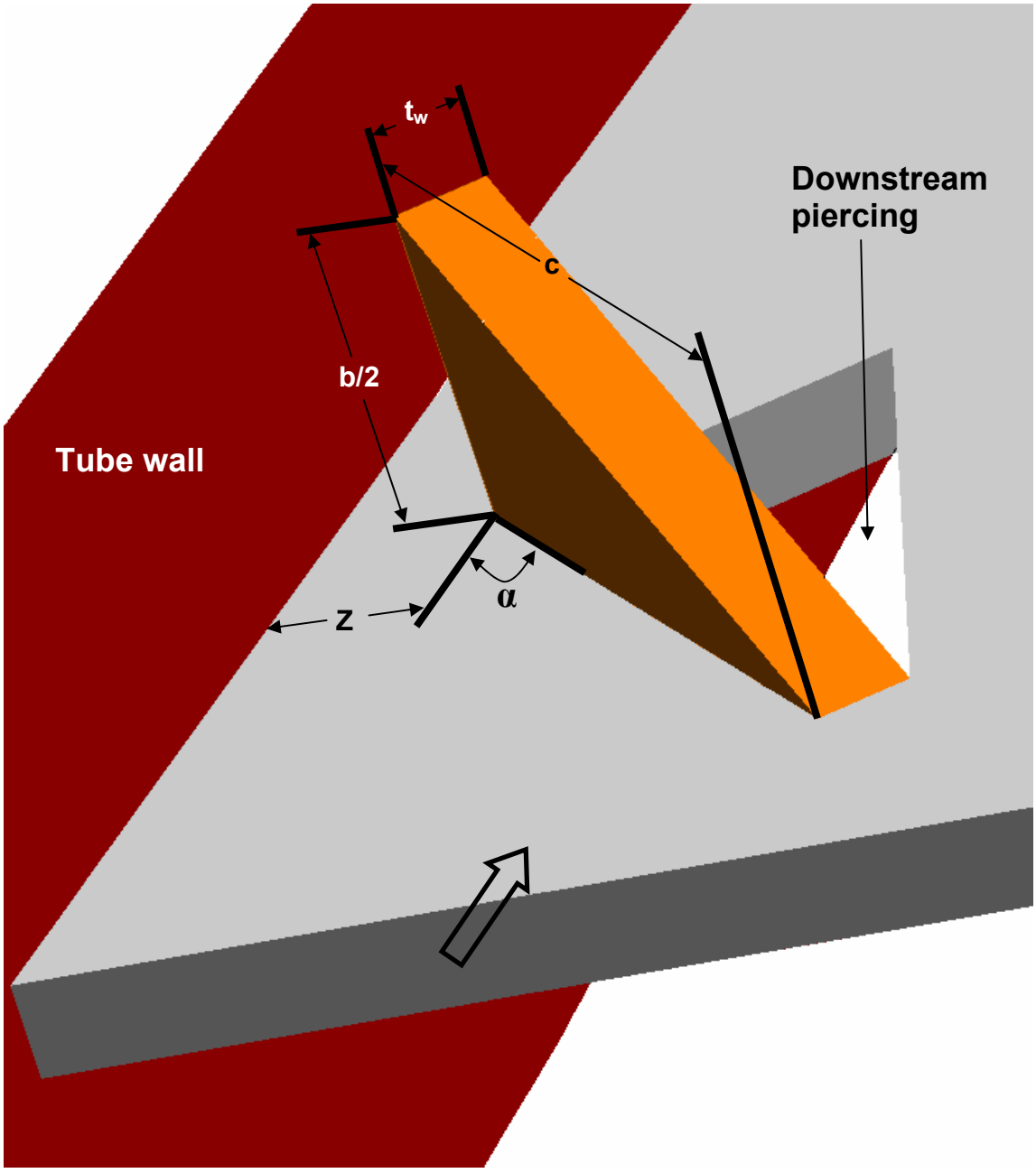

Figure B5. Illustration of a delta winglet vortex generator in the VG-F orientation angled towards the wall with a piercing on the downstream side.

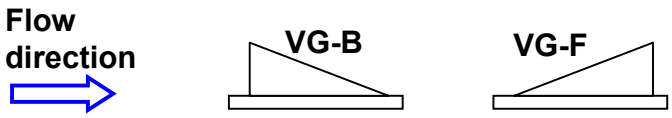

Figure B6. The definition of vortex generators placed in the backwards (VG-B) and forwards (VG-F) orientations.

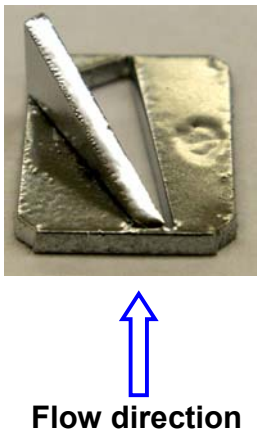

Figure B7. Insert for simulating a VG-F winglet with a downstream piercing.

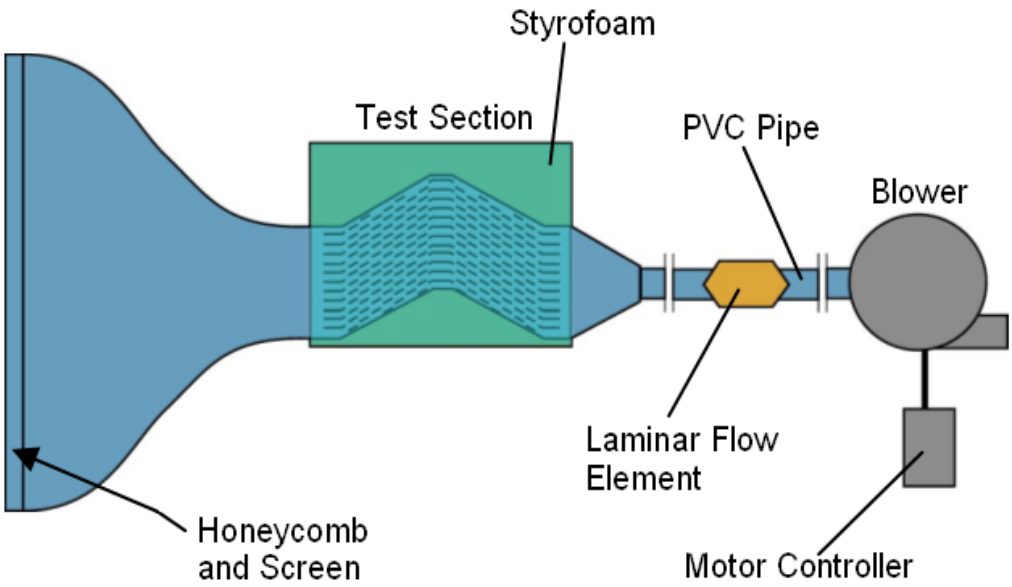

Figure B8. Test facility components.

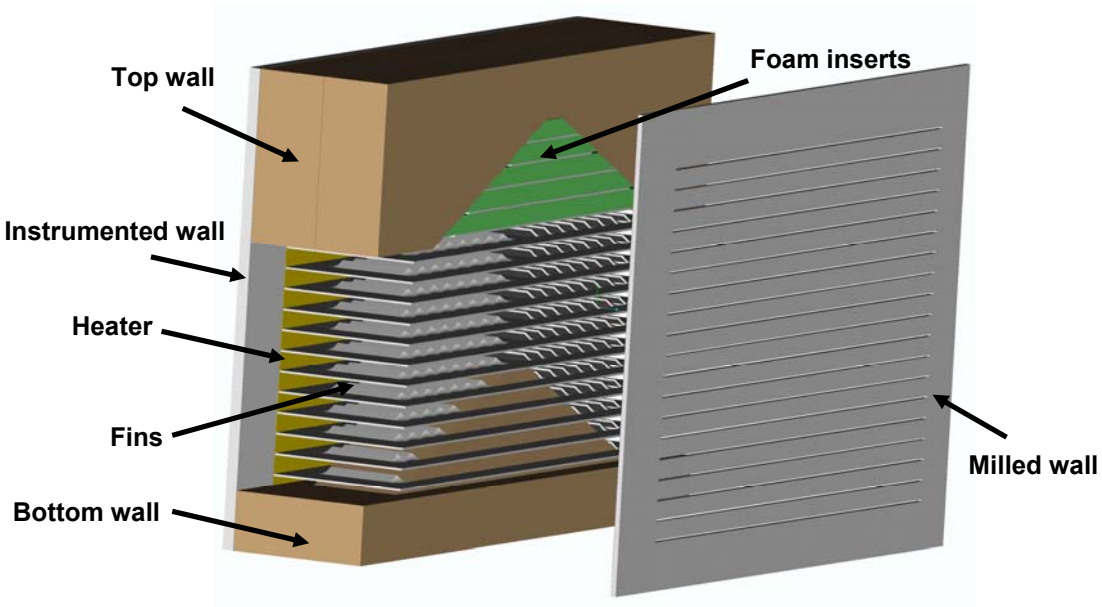

Figure B9. Exploded view of the L_l/F_h = 70% and L_l/F_h = 82% test section.

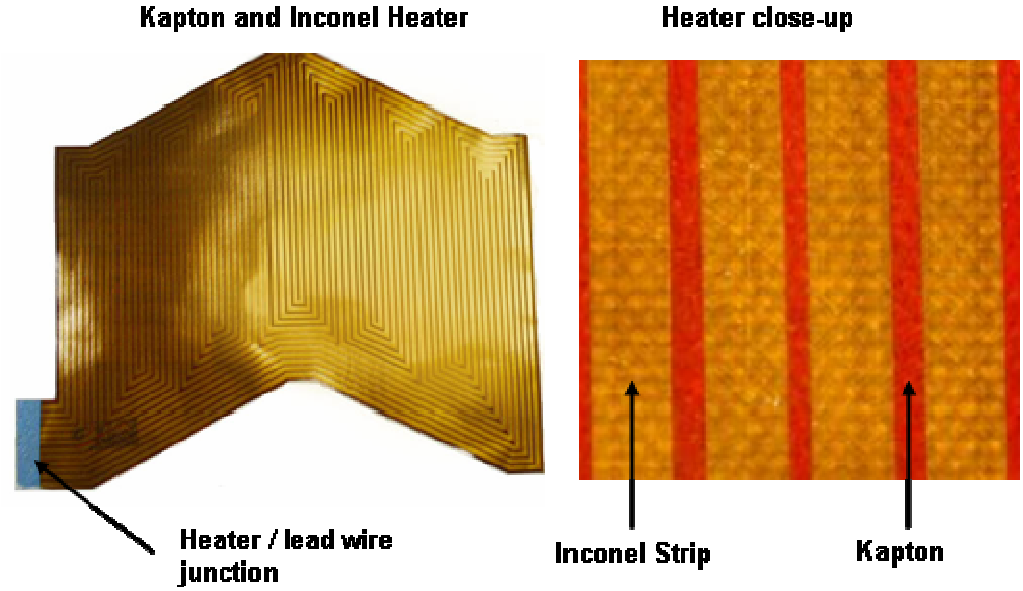

Figure B10. Custom kapton and inconel constant heat flux heater.

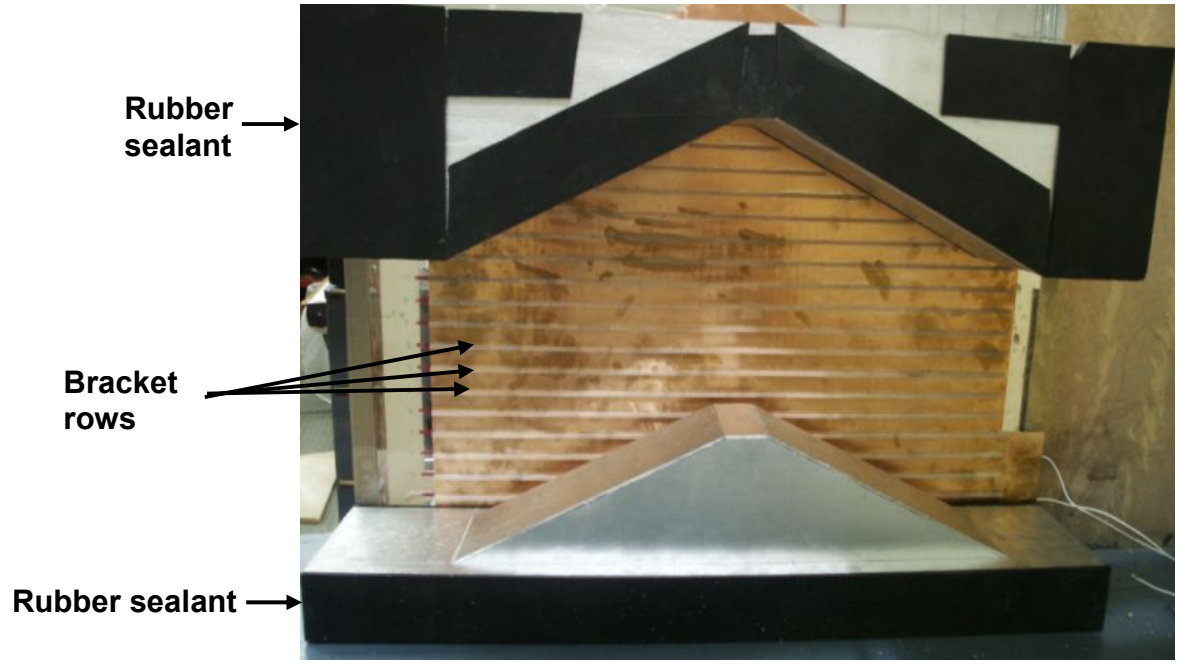

Figure B11. L_l/F_h = 70% and L_l/F_h = 82% test section side view showing fin brackets and rubber seals.

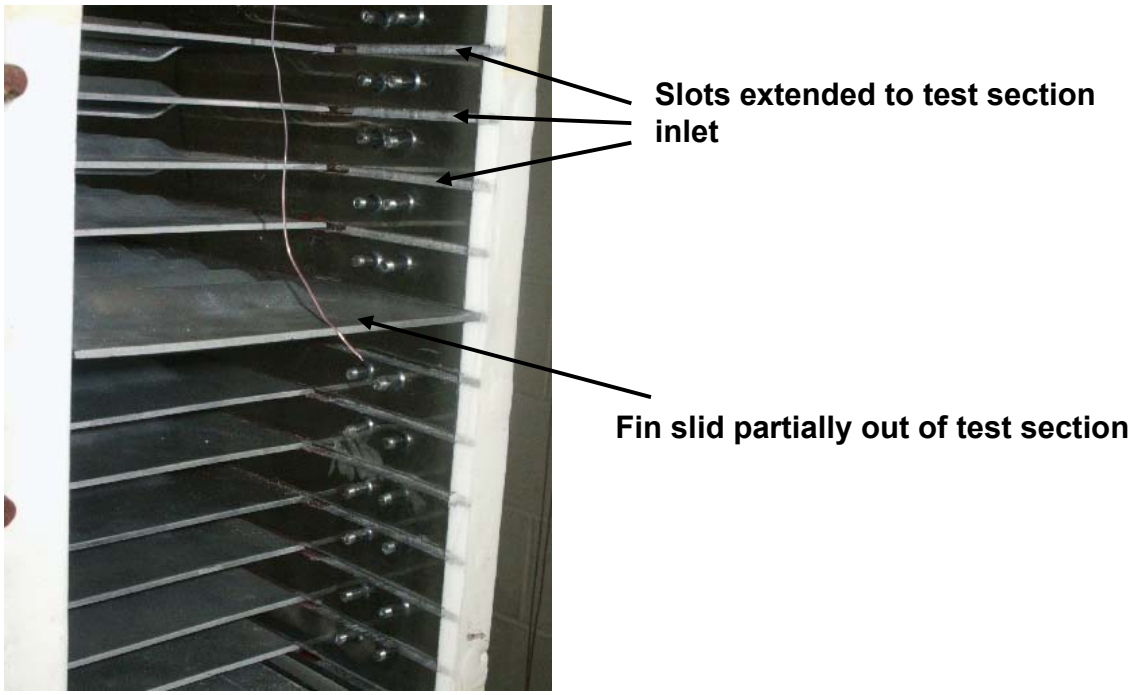

Figure B12. View of test section inlet showing slots for easy fin removal.

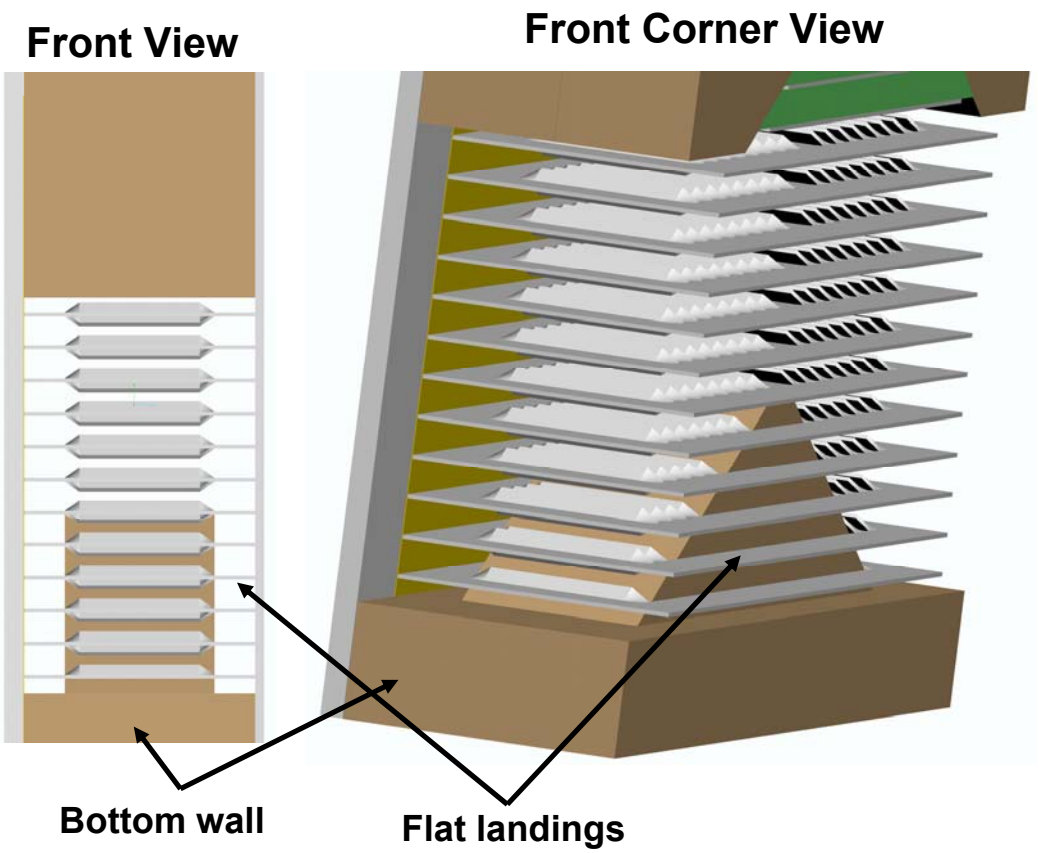

Figure B13. Diagrams showing geometric features of the bottom wall and surrounding fins.

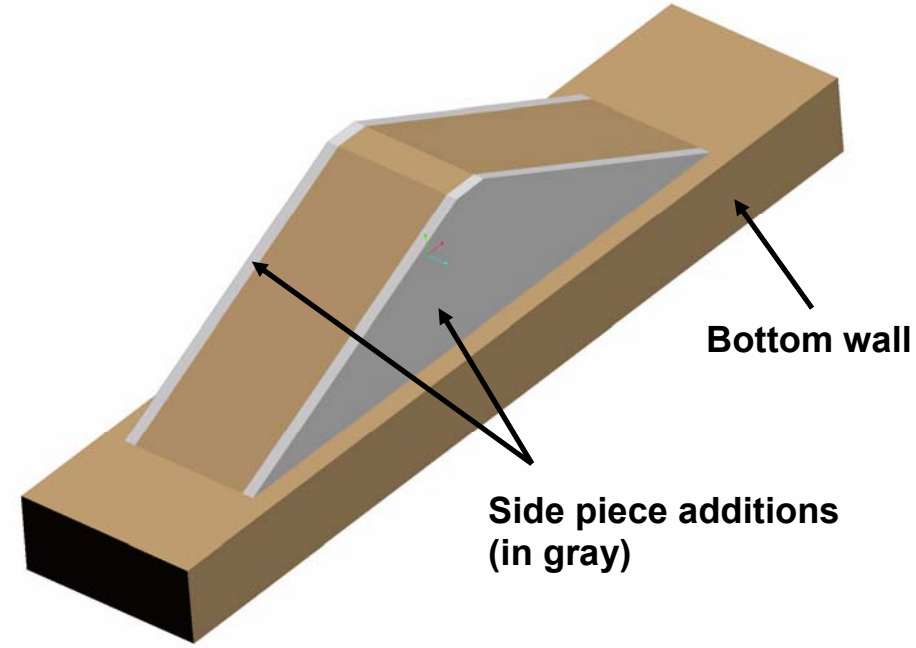

Figure B14. Diagram of bottom wall side piece additions for converting from L_l/F_h = 70% to L_l/F_h = 82% louver lengths.

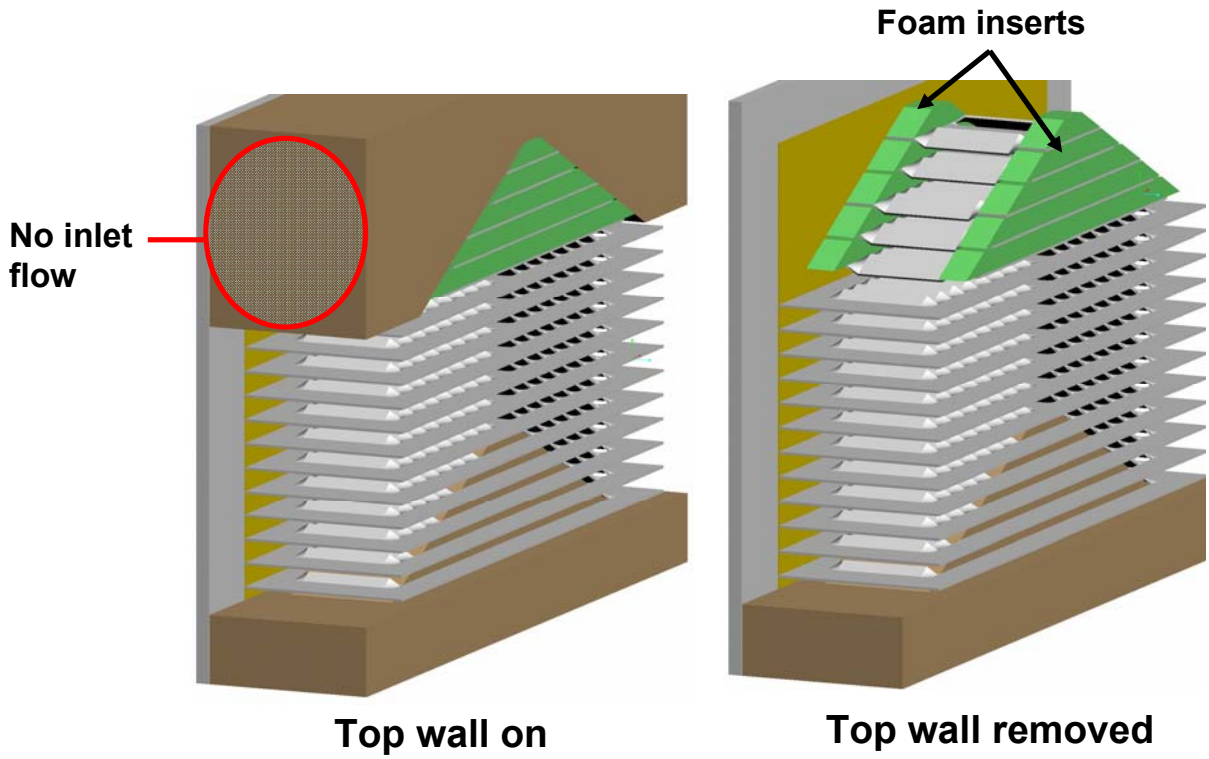

Figure B15. Diagram showing blocked off channel flow in top wall area.

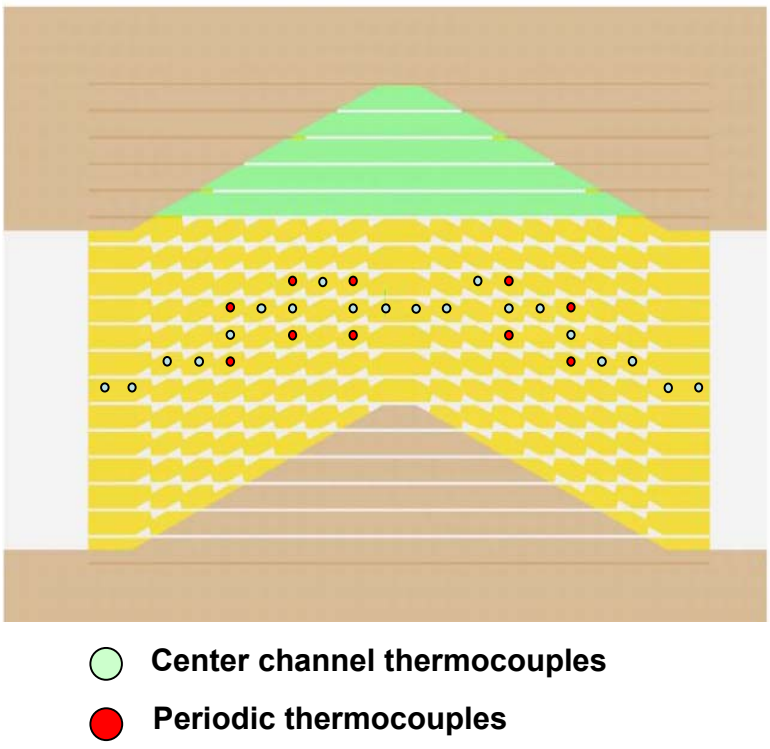

Figure B16. Thermocouple setup for the L_l/F_h = 70% and L_l/F_h = 82% test section.

Appendix C
Additional Experimental Results

This appendix contains the results of all experiments performed using the three-dimensional louvered fins. As discussed in previous sections, several winglet and piercing geometries were tested to determine a configuration that provided high heat transfer augmentation and small pressure loss increases. Table C1 contains the data for all the winglet and piercing configurations tested. The remainder of Appendix C is divided into six sections. The first section, C.1, identifies the different winglet and piercings configurations tested. Sections C.2 through C5 present the data collected. The titles of sections C.2 through C.5 correspond to sections of Table C1 that contain the data discussed in each section. The last section, C.6, presents the best pierced louvered fin mirrored winglet configuration tested.

C.1 Winglet and Piercing Configurations

One method by which winglet configurations were varied was by changing the geometry of the winglets. Winglet geometries tested include: aspect ratio, distance form tube wall, and angle of attack. Figure C1 illustrates how these parameters were measured. Aspect ratios of Λ = 1.5, 2, and 3, distances from the wall of Z = 0.15, 0.22, and 0.29, and angles of attack of $\alpha = 30^{\circ}$ and 40° were tested. Also, as shown in Figure C2, the direction in which winglets were placed was varied between the forwards (VG-F) and backwards (VG-B) directions.

Winglet configurations also differed from one another by the location that the winglets were placed on the louvered fins. Figure C3 shown how different numbers of winglets were placed on the louvered fins in different patterns. In addition to varying the number of winglets, winglets placement with respect to the top and bottom of the louvered fins was varied as shown in Figure C4.

During manufacturing of louvered fin heat exchangers, the heat exchanger core containing the louvered fins can be assembled in a number of different orientations. This requires louvered fin performance to be independent of flow direction over the fin. If winglets are implemented, the winglet configuration needs to be mirrored (or symmetric) across the turnover louver for performance to be independent of flow direction. Mirrored and non-mirrored configurations were both tested and the difference between the two is shown in Figure C5.

When piercings were implemented into the louvered fin geometry, there was a choice of piercing location with respect to flow direction. Piercings could either be placed on the up or downstream side of the winglets. Figure C1 shows a downstream piercing. Upstream piercings corresponded to a piercing on the pressure side of the winglet and downstream piercings were on the suction side of the winglets. Table C1 indicates exactly what winglet and piercing configuration was used for each test.

C.2 Baseline Data

All experiments used louvered fins with louver lengths of 70% or 82% of the total fin height as shown in Figure C6. Baseline testing was performed with no winglets or piercings incorporated into the louvered fins. Average Nusselt number was observed to increase with Reynolds number as the flowrate through the test section increased. Although friction factors were measured at each Reynolds number, due to the high experimental error associated with friction factor calculations at Re = 216 and 577, friction factors will only be reported at Re = 955.

C.3 Thin Winglet Testing using Solid Louvered Fins

Tests were performed using delta winglets that had a thickness of 0.03t to determine the effect of varying winglet aspect ratio and distance from the tube wall on tube wall heat transfer and pressure drop. Figures C7 and C8 show the results of these tests. Note that the numbers in parentheses in all graphs correspond to the test numbers in Table C1. Winglets aspect ratio was shown to affect heat transfer (Figure C7) and pressure drop with smaller aspect ratio winglets increasing both. Winglet distance from the tube wall was shown not to effect heat transfer (Figure C8) or pressure drop performance.

C.4 Thick Winglet Testing using Solid Louvered Fins

Test using winglets with $t_w = 0.67t$ were used to make comparisons between mirrored and non-mirrored winglet configurations, winglet orientation (VG-F and VG-B), number of winglets, and the effect of winglet thickness. Figures C9 through C12 present the results of these tests. Mirroring the winglet configuration across the turnover louver (Figure C9) was shown to decrease heat transfer augmentation and increase pressure losses. VG-B caused higher heat transfer and pressure drop than VG-F (Figure C10), and winglet performance was shown not to

be sensitive to varying the number of winglets or the winglet thickness (Figure C11 and C12 respectively).

C.5 Pierced Louvered Fin Testing

Parameters investigated during pierced louvered fin testing included: pierced versus solid louvered fins, aspect ratio, winglet orientation, piercings orientation, winglet placement, louver length effects, and winglet angle of attack. Figures C13 through C17 present the results of these tests.

Piercings in the louvered fins decreased heat transfer augmentation (Figure C13) and lowered pressure loss increases compared to solid louvered fin winglet configurations. An important conclusion drawn from the pierced louvered fin testing was that winglet effects measured with solid louvered fins were not the same for pierced louvered fins. This was due to piercings altering the flow field near the wall. Notably, VG-B and $\Lambda = 1.5$ winglets performed best in solid louvered fin testing with respect to heat transfer. For the pierced louvered fins however, VG-F were seen to provide significant advantages over VG-B (Figure C14) and there was negligible difference between $\Lambda = 1.5$ and 2 winglets (Figure C13) in respect to heat transfer.

Testing showed upstream piercings performed better than downstream piercings (Figure C15). However, there was negligible effect of piercing orientation on average heat transfer because the winglet configuration was mirrored, causing each winglet configuration in Figure C15 to have both upstream and downstream piercings. Winglet placement strongly effected winglet performance with the best mirrored configuration having all winglets on top of the louvered fin (Figure C16). Winglets with simulated piercings caused similar heat transfer augmentations for both the 70% and 82% louver length fins (Figures C17).

C.6 Best Pierced Louver Winglet Configurations

The best mirrored winglet configuration tested with piercings was number 29 in Table C1 and is shown in Figure C18. This configuration had $\Lambda = 2$ winglets and produced 24%, 5%, and -9% heat transfer augmentations at Re = 955, 577, and 216 respectively. Although the configuration of test number 23 performed similarly, test 23 had $\Lambda = 1.5$ winglets and had lager piercings in the louvered fins which needs to be avoided for manufacturing considerations. It is important to note that there was little difference measured between configurations of 16 and 28

winglets. The configuration of test 29 would be expected to perform well with either 16 or 28. Recommendations for an optimal non-mirrored configuration will be discussed in Appendix D

Table C1. Experimental Data for all Winglet Configurations Tested

Test #	L_l/F_h [%]	Winglet Setup	α	Z	Λ	VG's before turnover	t_w	Mirrored	# of VGs	Piercings before turnover	Re	$\overline{Nu}$	Nu_{aug} [%]	f	f_{aug} [%]
Baseline Data															
	70	baseline									216	5.5	-	0.218	-
											577	6.8	-	0.098	-
											955	7.9	-	0.069	-
	82	baseline									216	5.3	-	-	-
											577	6.9	-	-	-
											955	8.0	-	-	-
Thin Winglet Testing using Solid Louvered Fins															
1	70	1	40	0.22	3	VG-F towards	0.03t	yes	16	no	216	5.4	-3	-	-
											577	7.5	12	-	-
											955	9.4	24	0.076	11
2	70	1	40	0.22	2	VG-F towards	0.03t	yes	16	no	216	5.2	-5	-	-
											577	7.6	14	-	-
											955	9.6	28	0.080	16
3	70	1	40	0.22	1.5	VG-F towards	0.03t	yes	16	no	216	5.4	-2	-	-
											577	7.7	16	-	-
											955	9.9	33	0.084	22
4	70	1	40	0.15	1.5	VG-F towards	0.03t	yes	16	no	216	5.3	-4	-	-
											577	7.9	19	-	-
											955	10.0	33	0.086	24
5	70	1	40	0.29	1.5	VG-F towards	0.03t	yes	16	no	216	5.4	-3	-	-
											577	7.6	15	-	-
											955	9.8	31	0.086	24
Thick Winglet Testing using Solid Louvered Fins															
6	70	1	40	0.22	1.5	VG-B towards	0.67t	no	28	no	216	5.5	1	-	
											955	11.3	55	0.087	26
7	70	1	40	0.22	1.5	VG-F towards	0.67t	no	28	no	216	5.5	1	-	-
											577	8.5	30	-	-
											955	10.8	47	0.082	19
9	70	1	40	0.15	1.5	VG-F towards	0.67t	yes	28	no	216	5.3	-5	-	-
											577	7.6	14	-	-
											955	10.0	33	0.086	25
10	70	1	40	0.15	1.5	VG-B towards	0.67t	yes	28	no	216	5.3	-3	-	-
											577	8.0	20	-	-
											955	10.4	40	0.089	29
11	70	1	40	0.15	1.5	VG-F towards	0.67t	yes	16	no	216	5.4	-2	-	-
											577	7.6	15	-	-
											955	9.8	31	0.086	25
Pierced Louvered Fin Testing															
12	70	1	30	0.15	1.5	VG-B towards	1.1t	yes	28	downstream	216	5.2	-5	-	-
											577	7.0	3	-	-
											955	8.9	16	-	-
13	70	1	30	0.15	1.5	VG-B towards	1.1t	yes	28	downstream	955	8.6	11	-	-
14	70	1	30	0.15	1.5	VG-B towards	1.1t	yes	28	downstream	955	8.7	13	-	-
15	70	1	30	0.15	1.5	VG-B towards	1.1t	yes	28	no	955	10.0	33	-	-

16	70	1	30	0.15	1.5	VG-B towards	0.95t	yes	28	no	577	7.8	17	-	-
											955	10.1	35	-	-
17	70	1	30	0.15	1.5	VG-B towards	0.95t	yes	28	downstream	216	5.3	-5	-	-
											577	7.4	8	-	-
											955	8.6	12	0.079	15
18	70	1	30	0.15	1.5	VG-B towards	0.95t	yes	28	no	216			-	-
											577			-	-
											955	10.1	35	0.084	22
19	70	4	30	0.15	1.5	VG-B towards	0.95t	no	28	no	577	6.9	1	-	-
											955	9.4	24	-	-
20	70	4	30	0.15	1.5	VG-B towards	0.95t	no	28	upstream	216	4.9	-12	-	-
											577	6.6	-5	-	-
											955	8.0	2	0.081	17
21	70	1	30	0.15	1.5	VG-B towards	0.95t	yes	28	upstream	216	5.2	-6	-	-
											577	6.8	3	-	-
											955	8.7	12	0.082	19
22	70	3	30	0.15	1.5	VG-B towards	0.95t	no	28	upstream	216	5.3	-2	-	-
											577	7.2	7	-	-
											955	9.1	19	0.080	16
23	70	1	30	0.15	1.5	VG-F towards	0.95t	yes	28	downstream	216	5.0	-8	-	-
											577	7.3	8	-	-
											955	9.2	22	0.082	18
24	70	1	30	0.15	1.5	VG-F towards	0.95t	yes	16	downstream	216	5.1	-7	-	-
											577	5.1	5	-	-
											955	9.2	21	0.079	14
25	70	2	30	0.15	1.5	VG-F towards	0.95t	yes	16	downstream	216	5.1	-7	-	-
											577	6.7	-3	-	-
											955	8.4	9	0.076	11
26	70	2	30	0.15	1.5	VG-F towards	0.95t	yes	28	downstream	955	8.9	15	-	-
27	70	5	30	0.15	1.5	VG-F towards	0.95t	no	28	downstream	216	5.0	-9	-	-
											577	7.0	2	-	-
											955	8.5	9	0.085	23
28	70	1	30	0.15	1.5	VG-F towards	0.95t	yes	28	no	216	5.1	-8	-	-
											577	7.6	14	-	-
											955	9.9	33	0.085	23
29	70	1	30	0.15	2	VG-F towards	0.95t	yes	28	downstream	216	5.0	-9	-	-
											577	7.1	5	-	-
											955	9.4	24	0.076	10
30	70	1	30	0.15	2	VG-F towards	0.95t	yes	16	downstream	216	5.1	-7	-	-
											577	7.3	8	-	-
											955	9.1	20	0.072	4
31	70	1	40	0.15	1.5	VG-F towards	0.95t	yes	16	downstream	216	5.3	-5	-	-
											577	6.9	2	-	-
											955	9.0	17	0.075	9
32	70	1	40	0.15	1.5	VG-F towards	0.95t	yes	28	downstream	216	5.1	-9	-	-
											577	7.0	3	-	-
											955	9.2	21	0.082	19
33	70	1	40	0.15	2	VG-F towards	0.95t	yes	16	downstream	216	5.2	-5	-	-
											577	7.0	4	-	-
											955	9.0	18	0.077	11

34	70	1	40	0.15	2	VG-F towards	0.95t	yes	28	downstream	216	-	-	-	-
											577	-	-	-	-
											955	-	-	0.079	15
35	70	1	30	0.15	2	VG-F towards	0.95t	yes	14	downstream	216	4.9	-11	-	-
											577	7.0	5	-	-
											955	9.0	19	0.072	4
36	70	3	30	0.15	2	VG-F towards	0.95t	no	14	downstream	216	5.1	-8	-	-
											577	6.7	-1	-	-
											955	8.2	7	0.070	1
37	82	1	30	0.1	2	VG-F towards	0.95t	yes	28	downstream	216	5.0	-8	-	-
											577	6.9	3	-	-
											955	9.1	20	0.079	14

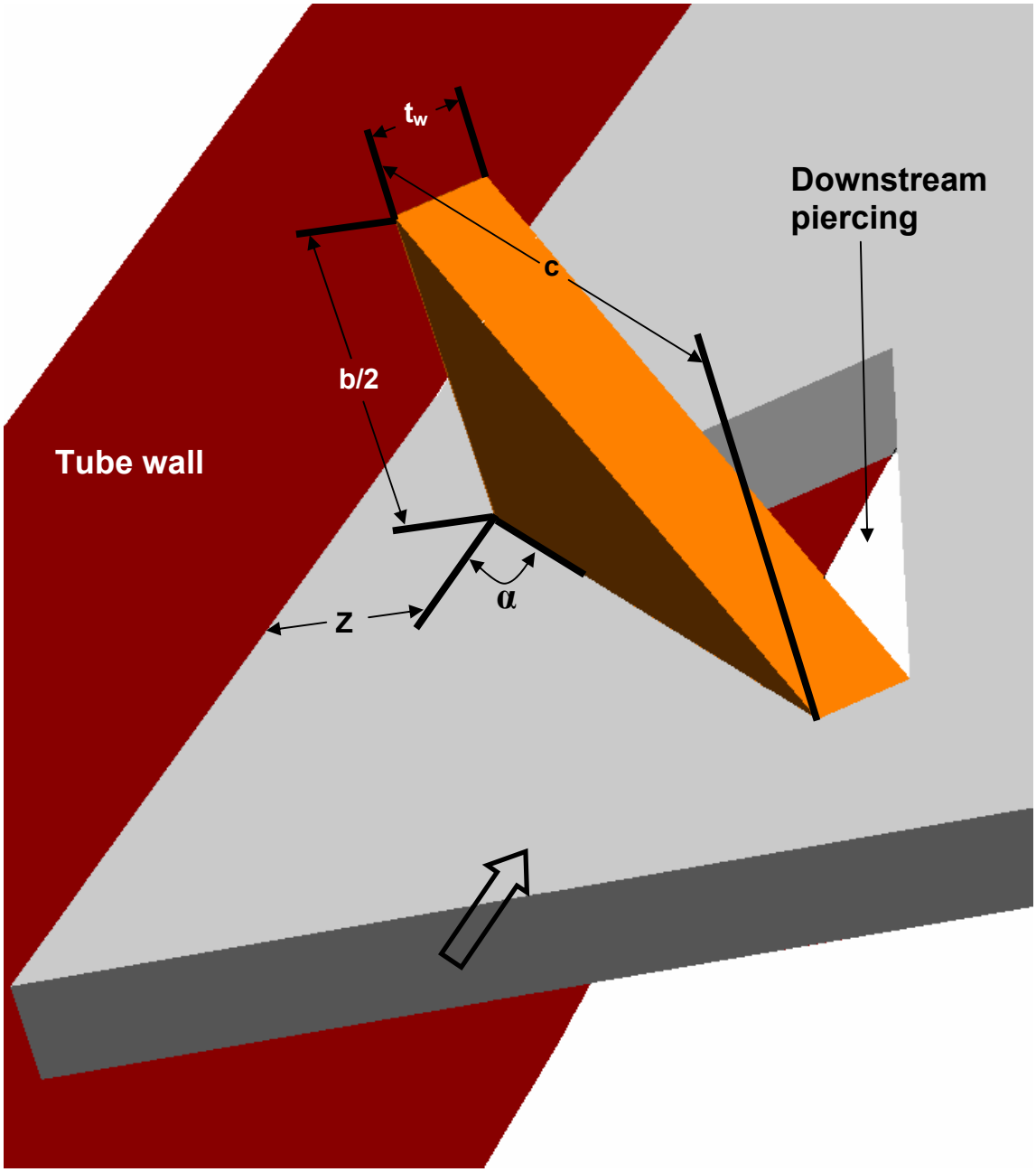

Figure C1. Illustration of a delta winglet vortex generator in the VG-F orientation angled towards the wall with a piercing on the downstream side.

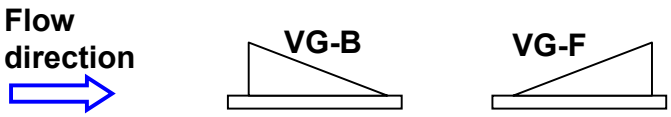

Figure C2. The definition of vortex generators placed in the backwards (VG-B) and forwards (VG-F) orientations.

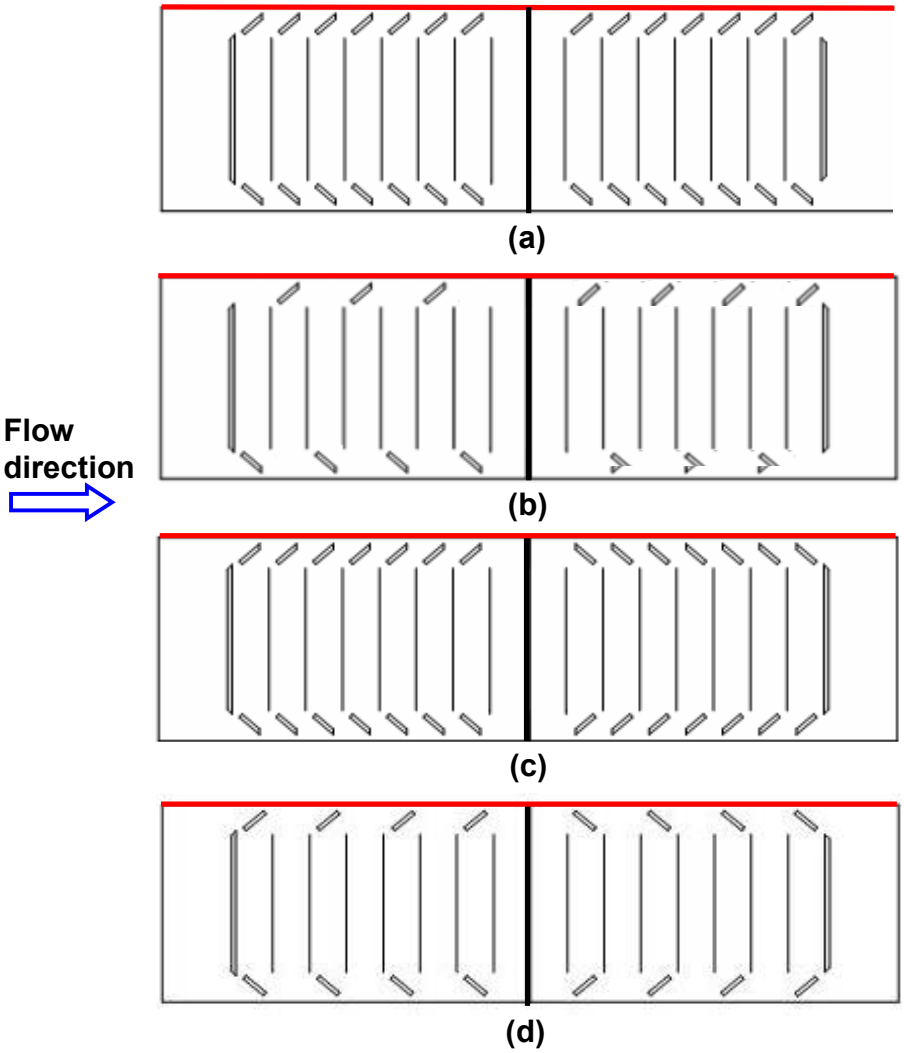

Figure C3. (a) – the 28 and (b) the 14 winglet configurations with all winglets angled towards the wall. (c) – the 28 and (d) the 16 winglet configurations with winglets angled towards the wall before the turnover louver and away from the wall after the turnover louver. Note the dark red line represents the heated tube wall and that only configurations (c) and (d) are mirrored.

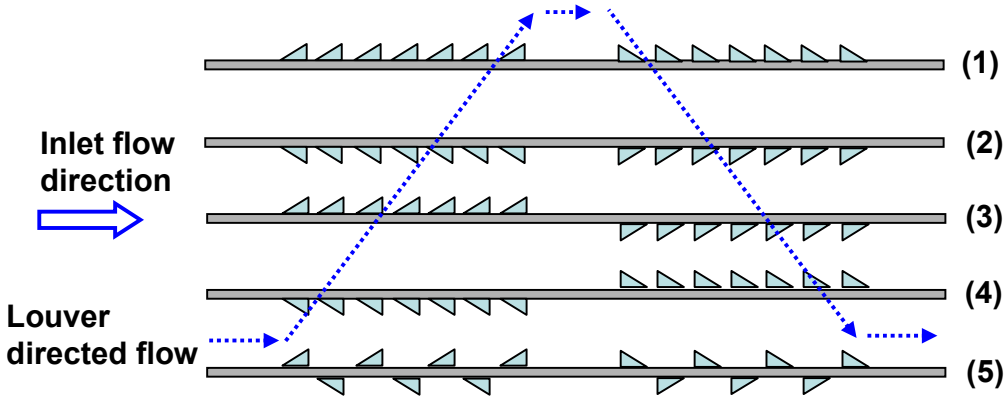

Figure C4. Different winglet placement locations tested: (1) – all winglets on top of the louvered fins, (2) – all winglets on the bottom of the louvered fins, (3) winglets on the top before the turnover louver and on the bottom after the turnover louver, (4) winglets on the bottom before the turnover louver and on the top after the turnover louver, and (5) – winglets alternating between placement on the top and bottom of the louvered fins. Note that only configurations (1), (2), and (5) are mirrored.

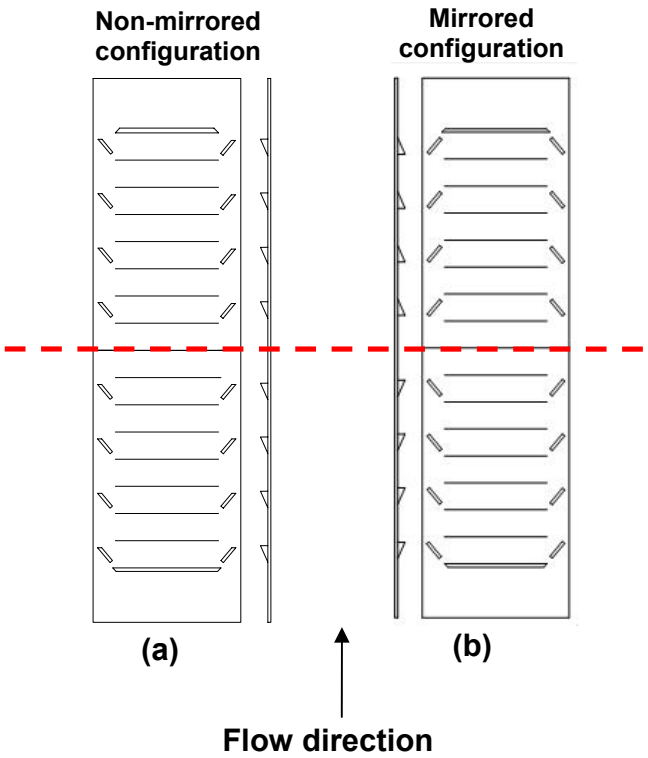

Figure C5. (a) – Mirrored and (b) – non-mirrored winglet configurations. The red dotted line passing through the turnover louver is the plane across which the winglet setup must be mirrored.

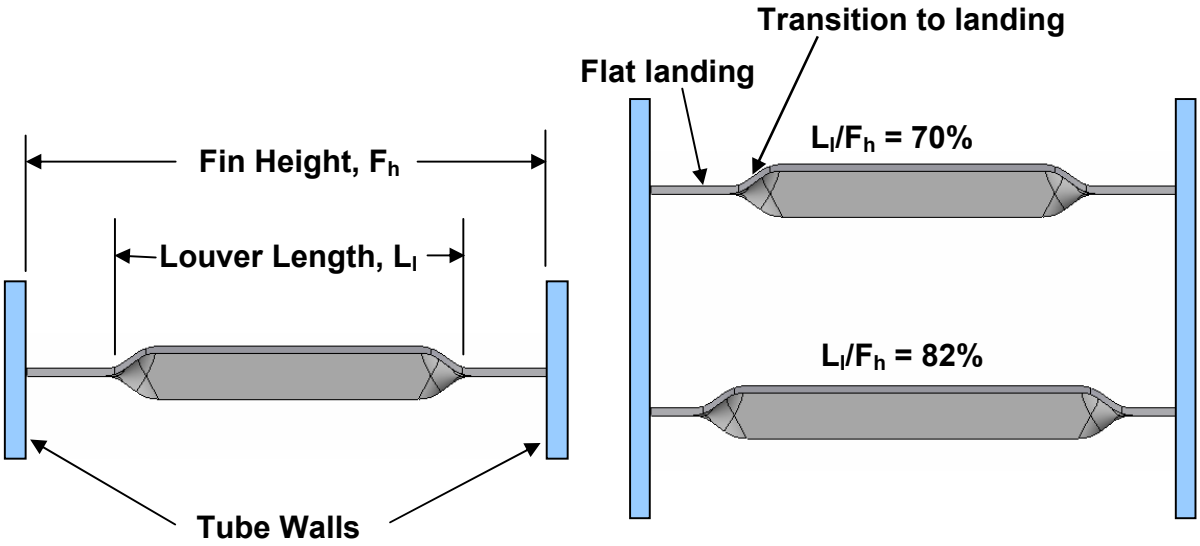

Figure C6. Different louvered fin geometries used in this study.

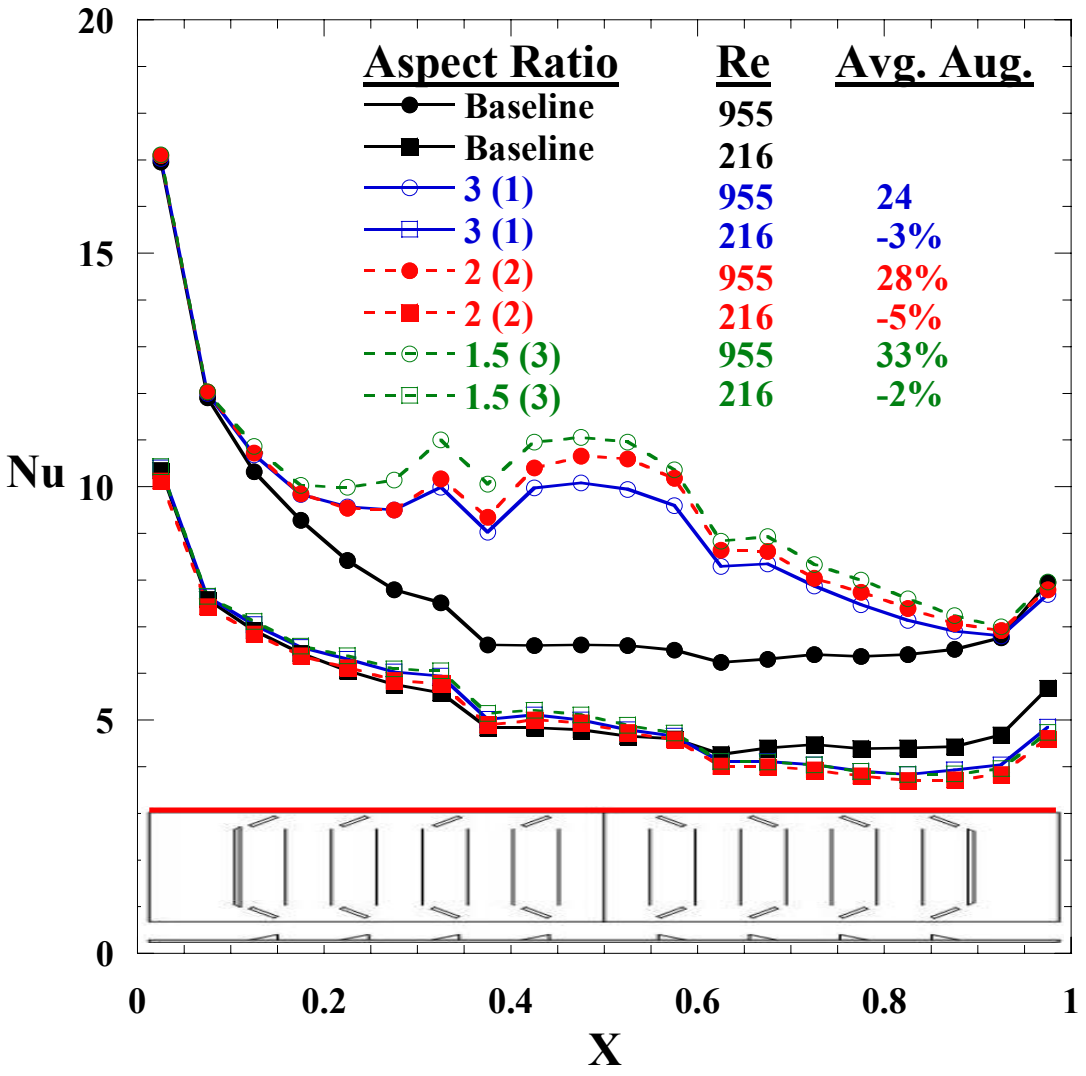

Figure C7. Comparison of heat transfer performance between winglets of different aspect ratios using solid louvered fins.

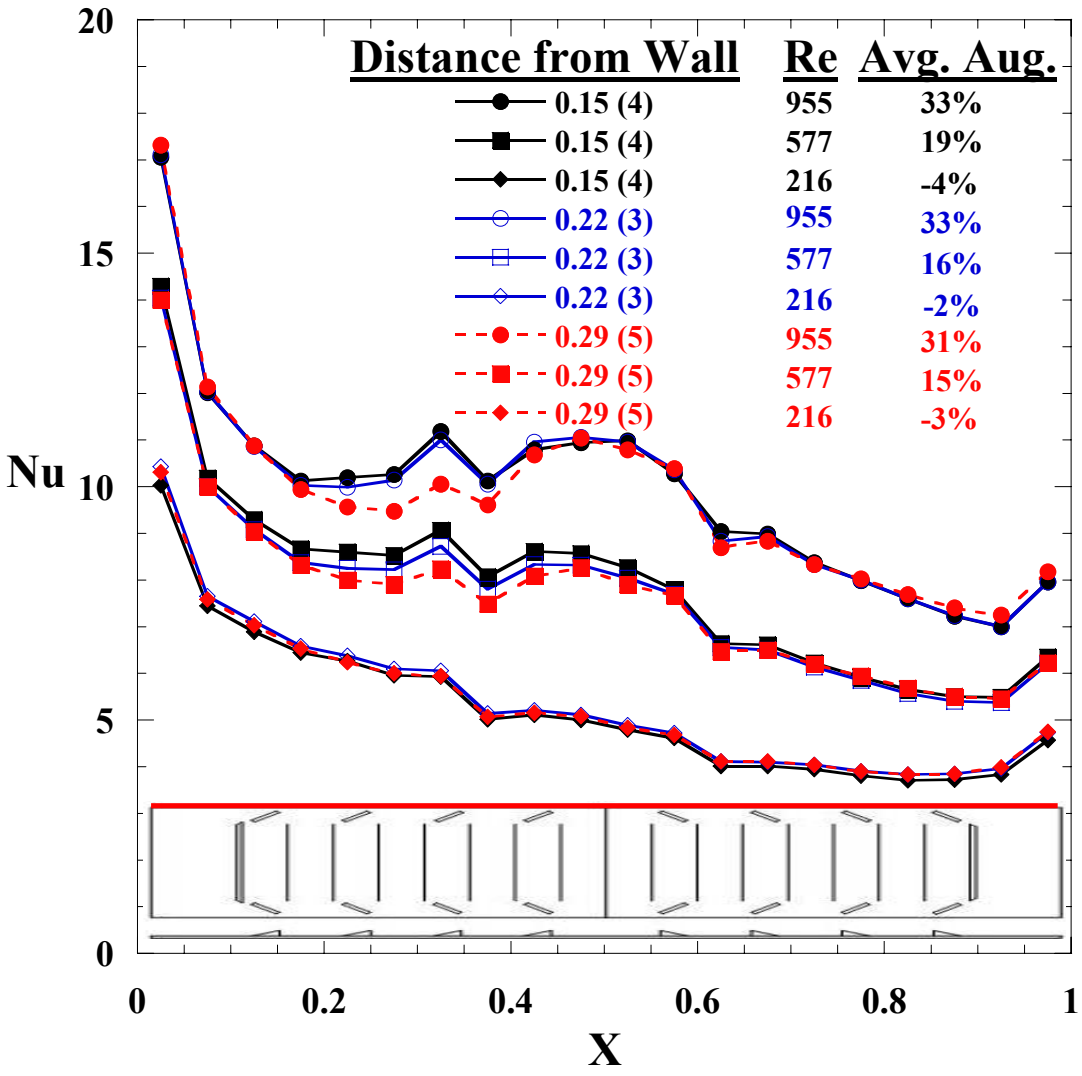

Figure C8. Comparison of heat transfer performance between winglets having different distances from the tube wall using solid louvered fins.

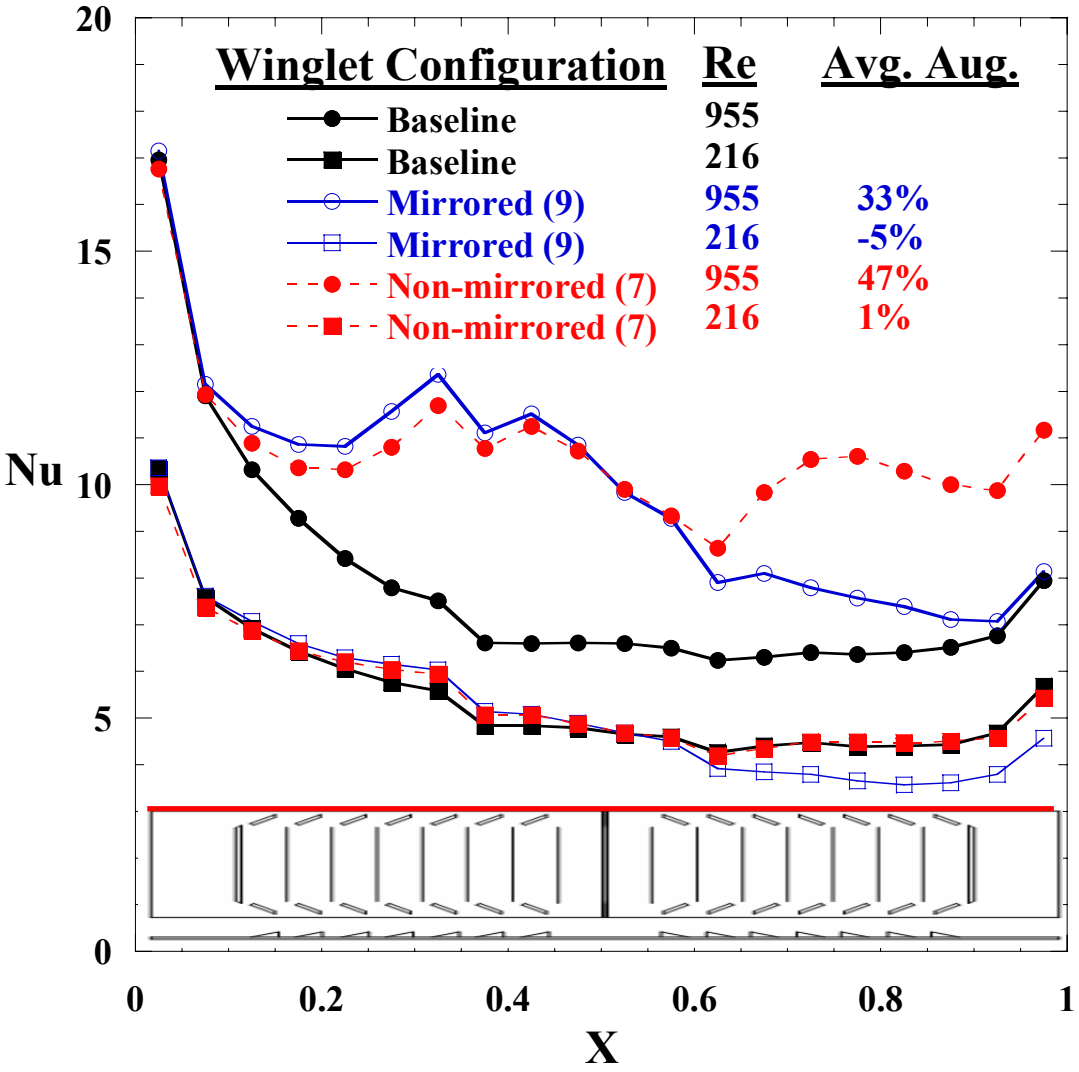

Figure C9. Comparison of heat transfer performance between non-mirrored and mirrored winglet configurations using solid louvered fins. Note the winglet configuration shown is for the mirrored test.

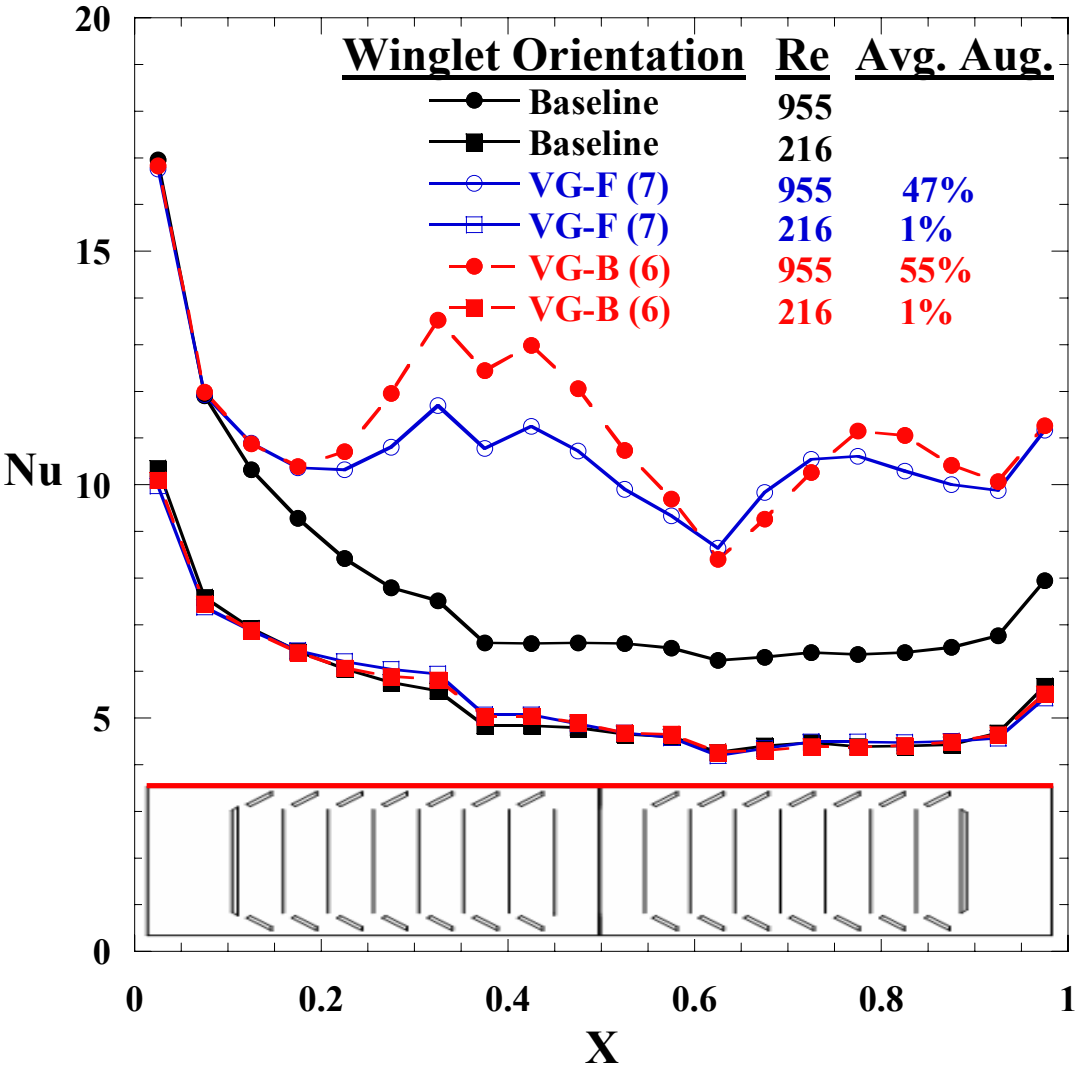

Figure C10. Comparison of heat transfer performance between non-mirrored winglets configurations of VG-B and VG-F using solid louvered fins.

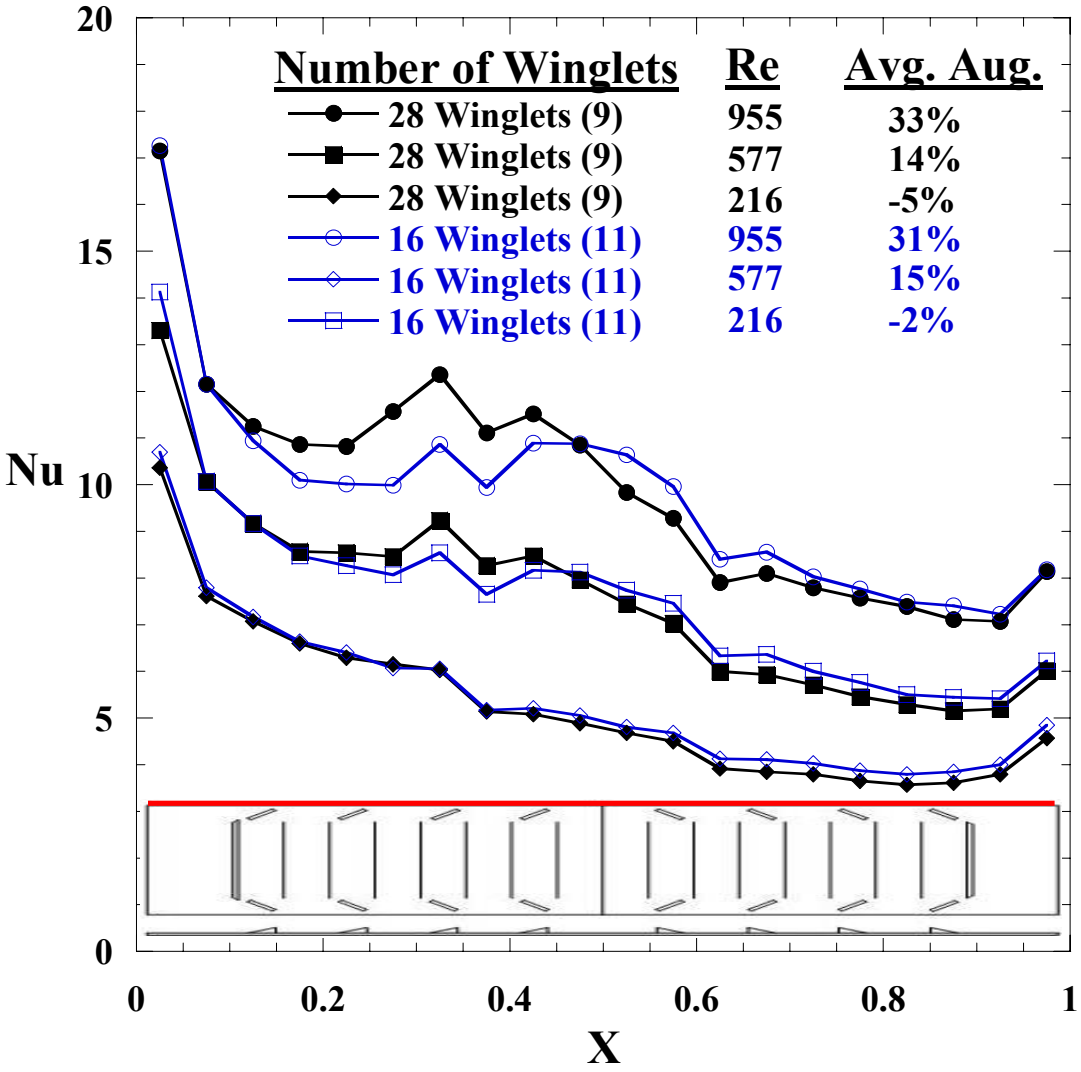

Figure C11. Comparison of heat transfer performance between 28 and 16 winglet configurations using solid louvered fins. Note the winglet configuration is shown for the 16 winglet test.

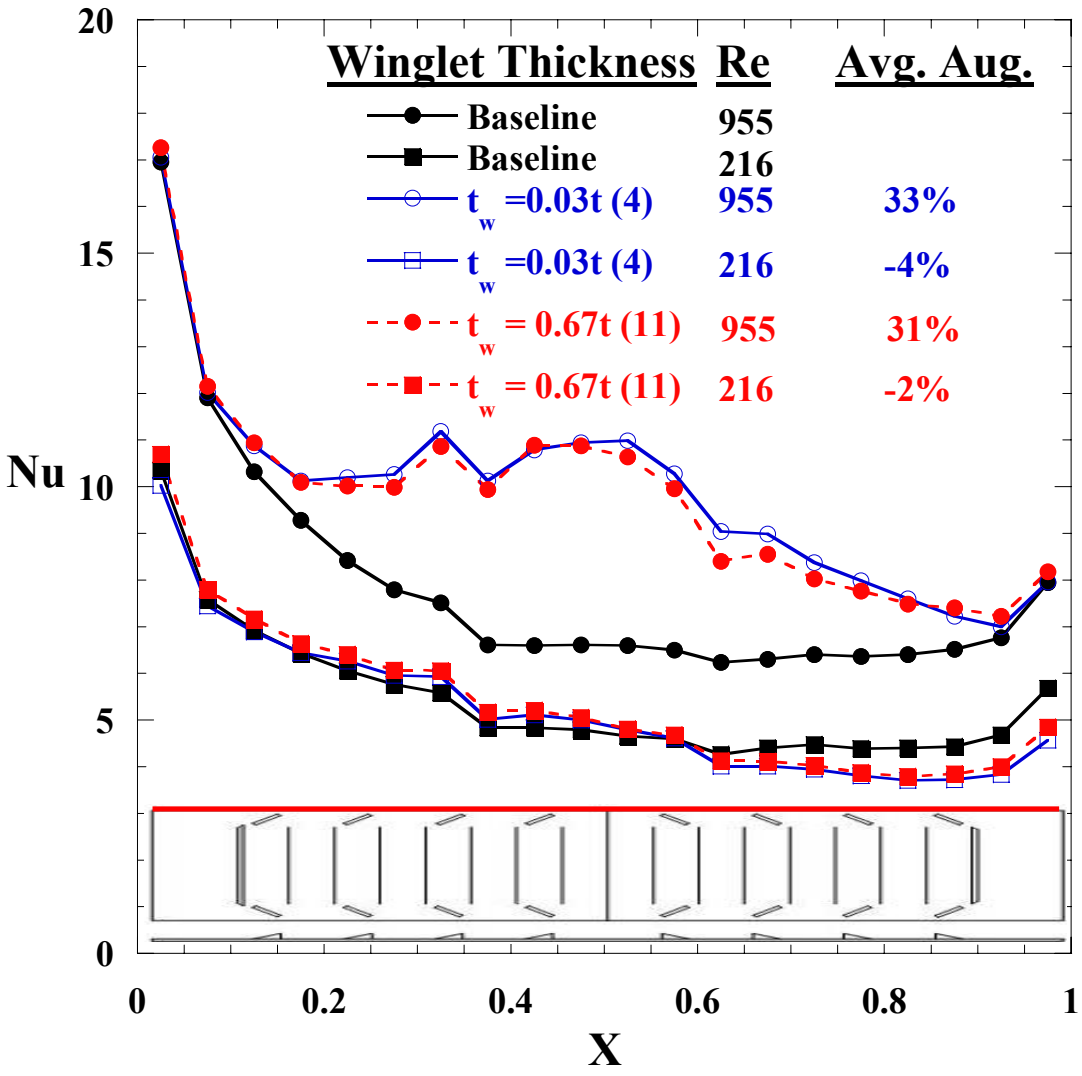

Figure C12. Comparison of heat transfer performance between winglet configurations having different winglet thicknesses using solid louvered fins.

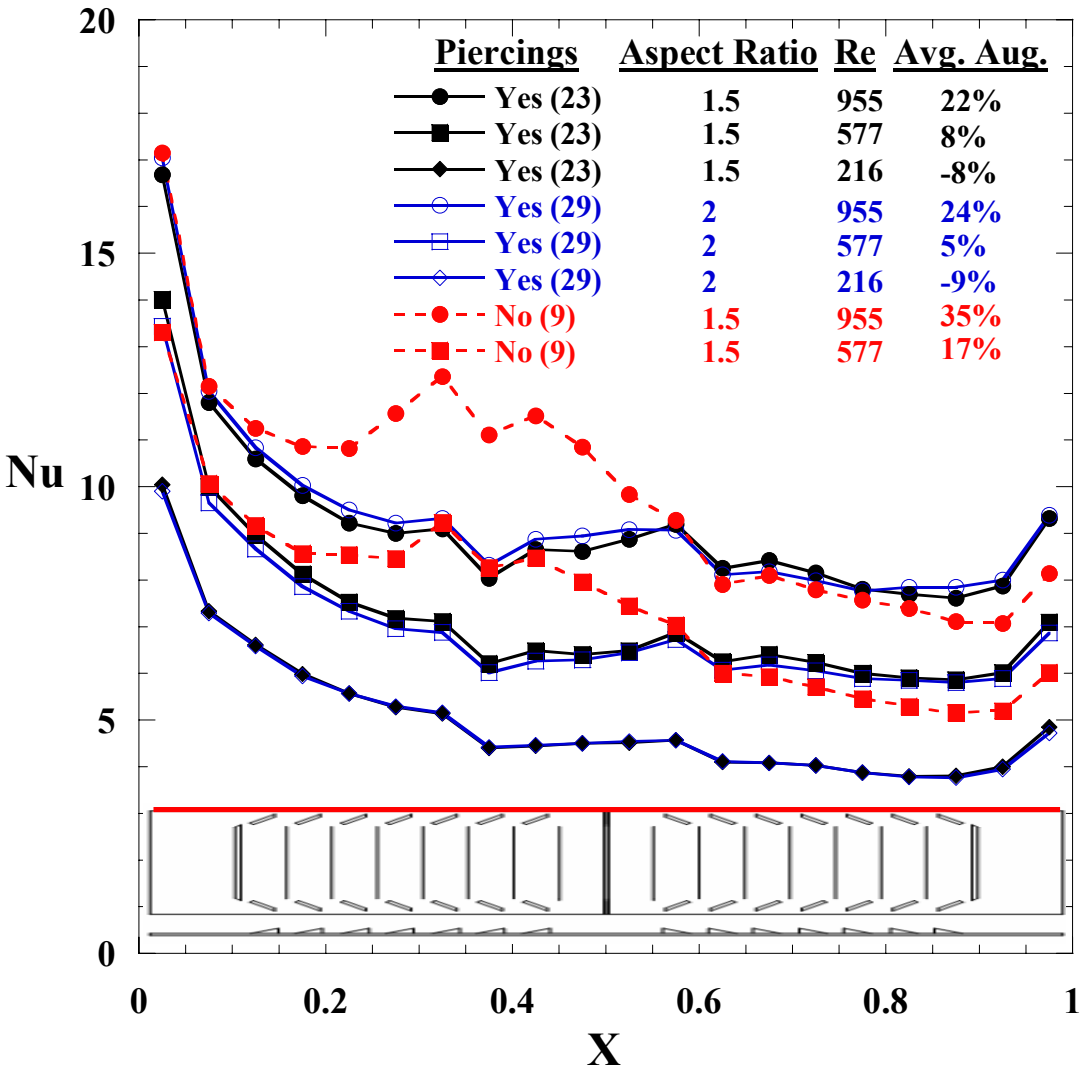

Figure C13. Comparison of heat transfer performance between pierced and solid fin winglet configurations. Also shown is the comparison of aspect ratio for the pierced louvered fin configurations.

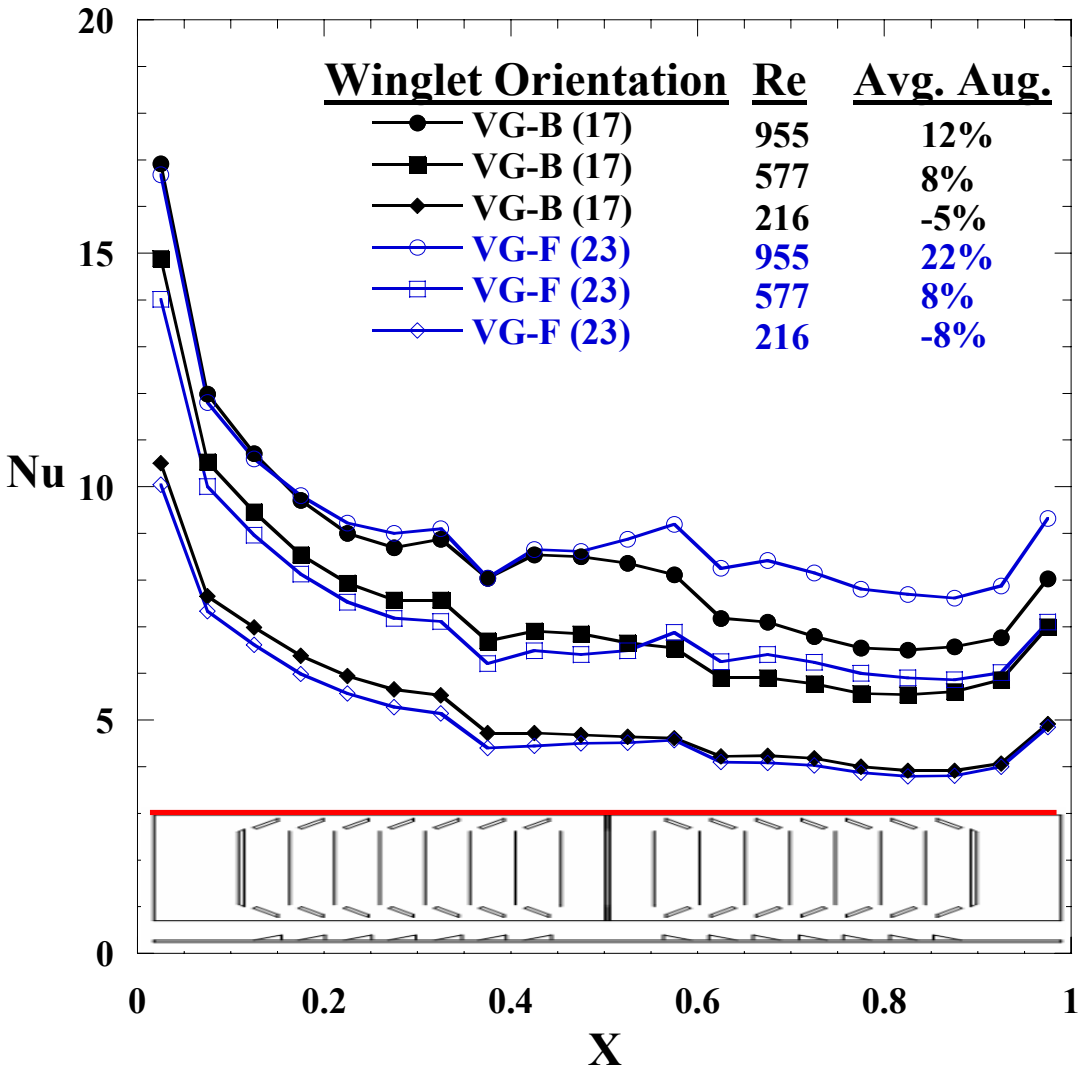

Figure C14. Comparison of heat transfer performance between VG-B and VG-F in a mirrored winglet configurations using pierced louvered fins. Note the winglet orientation labeled "VG-B" has VG-B before the turnover louver and VG-F after the turnover louver. The orientation labeled "VG-F" has VG-F before the turnover louver and VG-B after the turnover louver.

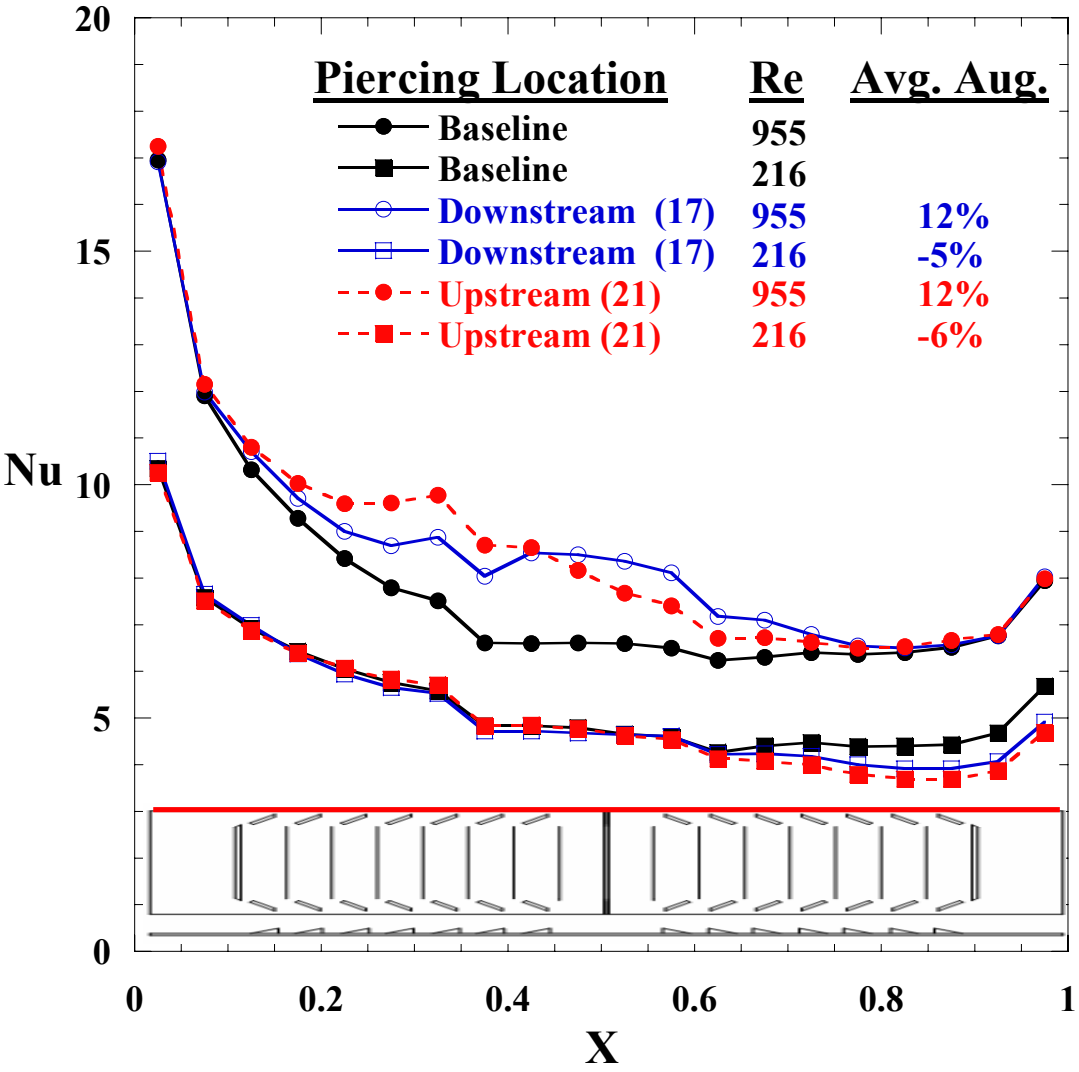

Figure C15. Comparison of heat transfer performance between winglets configurations having different piercing placements. Note that the tests labeled "downstream" had downstream piercings before the turnover louver and upstream piercings after it. The test labeled "upstream" had upstream piercings before the turnover louver and downstream piercings after the turnover louver.

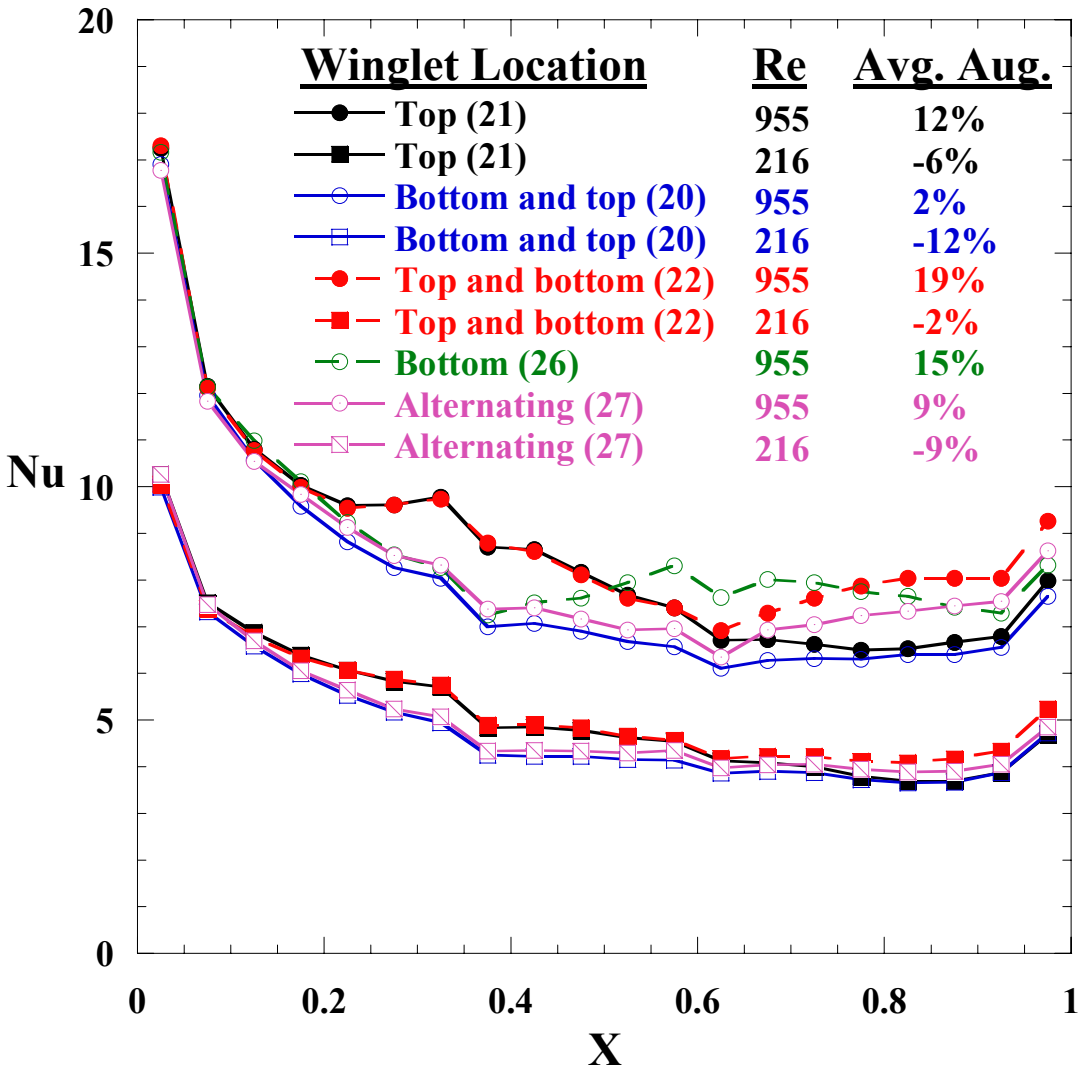

Figure C16. Comparison of heat transfer performance between winglets configurations having different winglet placements using pierced louvered fins. Note that no winglet configuration diagram is shown because the tests had several different configurations.

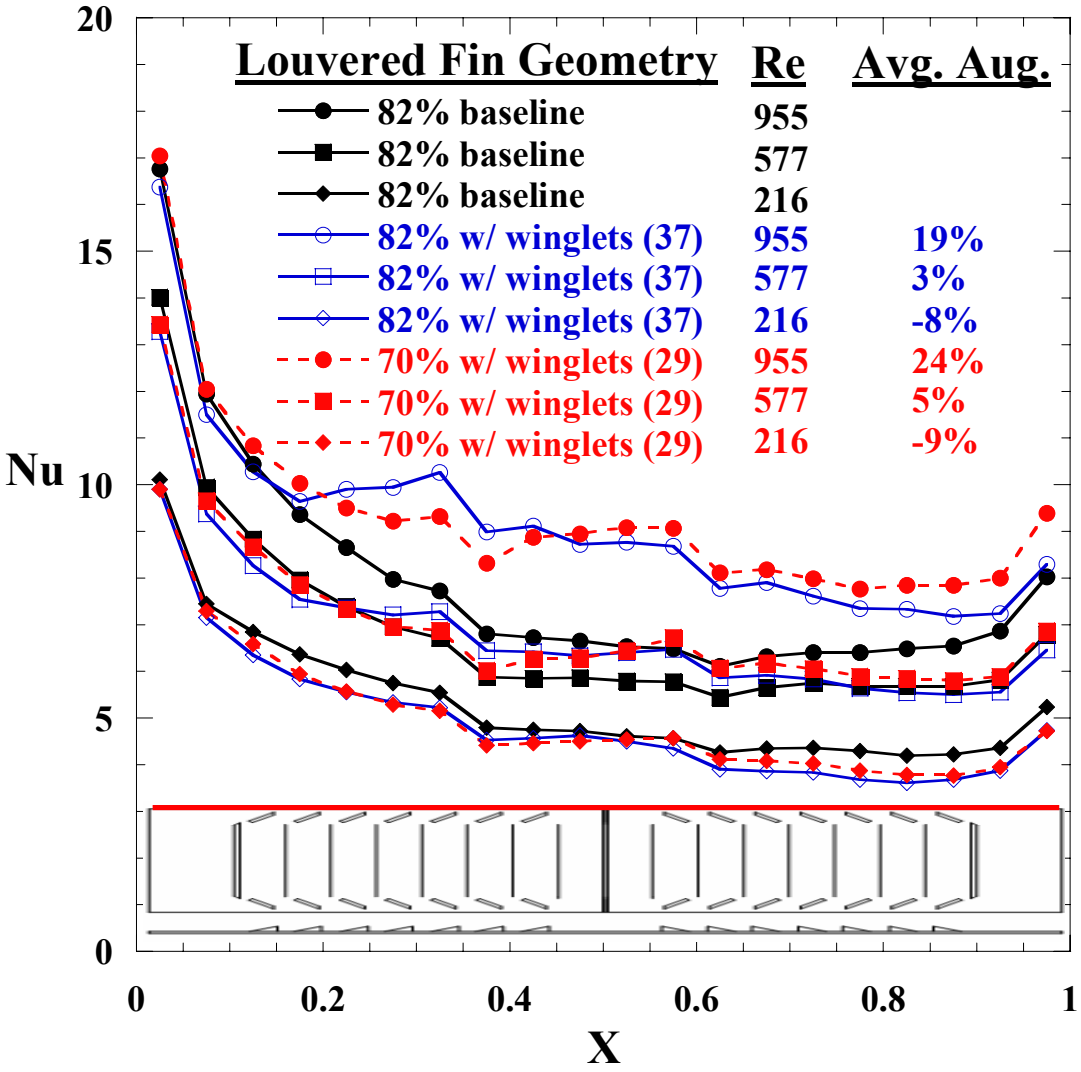

Figure C17. Comparison of heat transfer performance between winglets configurations on fins with different louver lengths using pierced louvered fins.

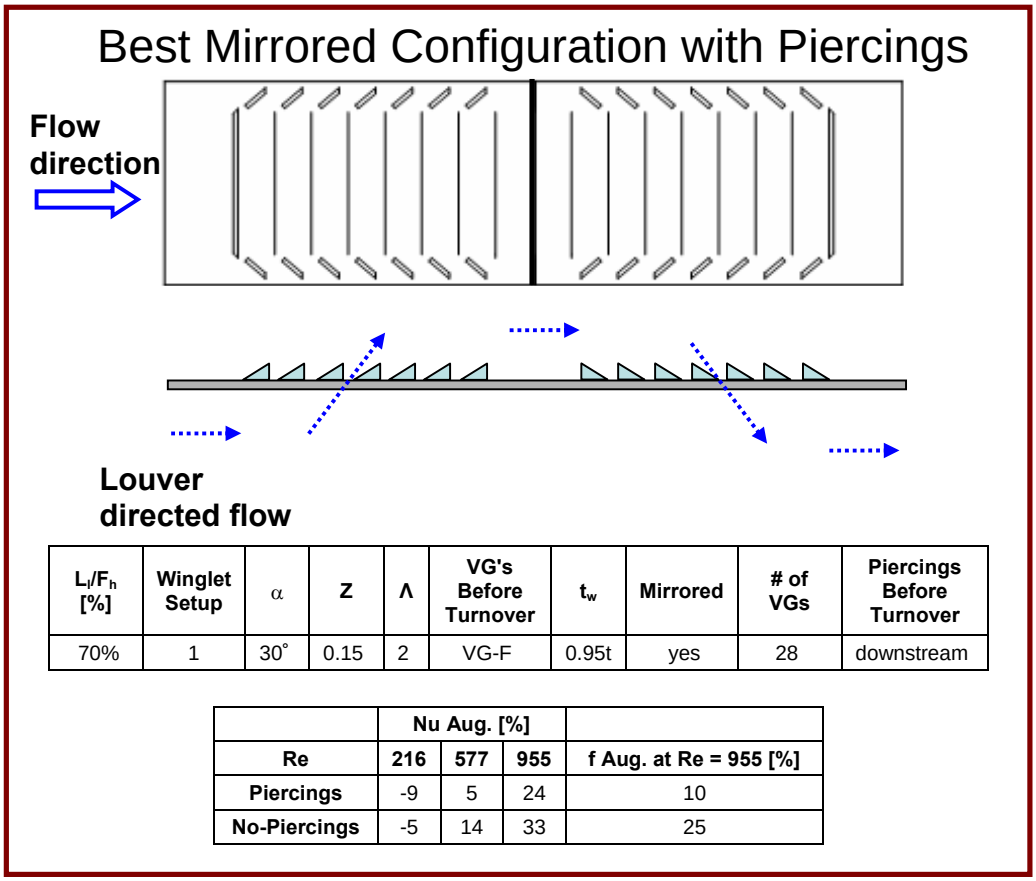

L_l/F_h [%]	Winglet Setup	α	Z	Λ	VG's Before Turnover	t_w	Mirrored	# of VGs	Piercings Before Turnover
70%	1	30°	0.15	2	VG-F	0.95t	yes	28	downstream

	Nu Aug. [%]			
Re	216	577	955	f Aug. at Re = 955 [%]
Piercings	-9	5	24	10
No-Piercings	-5	14	33	25

Figure C18. Best mirrored winglet configuration tested with simulated winglet piercings.

Appendix D
Summary of Findings and Recommendations

D.1 Summary of Findings

This study determined that it is necessary to account for the three-dimensionality of louvered fins to make accurate tube wall heat transfer measurements. Smoke visualization and CFD suggested that the discrepancy between measurements made using two- and three-dimensional geometries was because of the difference in the flow fields along the tube wall. As expected, because of the difference in the flow fields, delta winglets produce different effects on tube wall heat transfer in two- and three- dimensional geometries. For the two-dimensional geometry, delta winglets having the same thickness as the louvered fins produced a maximum of 8% heat transfer augmentation. Augmentation was due to flow redirection and not winglet vortex formation. As seen in Figure D1, winglets formed vortices in a two-dimensional geometry, however, these vortices were not able to propagate and were disrupted by the leading edge of the next louver in the streamwise direction. Piercings in the two-dimensional louvered fins were seen to disrupt vortex formation for winglets with downstream piercings. However, because flow redirection and not vortex propagation was the mechanism of augmenting heat transfer, piercings did not decrease heat transfer and actually caused slightly higher augmentations compared to the solid fin tests.

Winglets implemented along the flat landings of the three-dimensional louvered fins caused heat transfer augmentation of up to 55% along the tube wall, with a corresponding increase of 26% in pressure losses (test 6 in Table C1). Vortices formed by winglets were allowed to propagate in the channel-like flow along the tube wall and were not disturbed by louver effects. Vortex propagation is the reason for the large heat transfer augmentations in the three-dimensional compared to the two-dimensional louvered fin arrays.

Using a manufacturable pierced louvered fin winglet configuration that was mirrored across the turnover louver decreased the average tube wall heat transfer augmentation to 24%, with a corresponding pressure loss increase of 10% (test 29). Piercing the louvered fins and mirroring the winglets caused the large decrease in augmentations compared with non-mirrored solid louvered fin winglet configurations.

D.2 Recommendations and Future Work

The best mirrored winglet configuration tested with piercings using the three-dimensional louvered fins is shown in Figure D2. If the winglet configuration is required to be mirrored because of manufacturing considerations, the configuration in Figure D2 or one similar should be used. This setup produced high heat transfer augmentations of 24%, 5% and -9% at Re = 955, 577, and 216 respectively while causing only a 10% increase in pressure losses at Re = 955. As there was little difference observed between 16 and 28 winglet configurations, either number of winglets would be expected to produce similar results. Also, piercing orientation should not effect performance as the winglet configuration is mirrored and requires there to be upstream and downstream piercings.

Implementing delta winglets into heat exchangers with a three-dimensional pierced louvered fin geometry causes complex near tube wall flow fields. These flow field are not completely understood, therefore, it is difficult to choose an optimal winglet configuration to augment tube wall heat transfer. Due to manufacturing considerations, few non-mirrored winglet configurations were tested using pierced louvered fins. At the time of press however, a movement has begun within industry to manufacture and assemble louvered fin heat exchangers with non-mirrored winglet configurations. If a method of manufacturing non-mirrored configurations is found, more data is needed to choose an optimal winglet and piercing configuration to maximize heat transfer.

Figure D3 presents the pierced louvered fin winglet configuration predicted to causes the largest heat transfer augmentation based on experimental results. This configuration was not tested because it is non-mirrored and was not though to be manufacturable. Piercings should be on the upstream side as data showed this piercing orientation caused larger heat transfer augmentations than downstream piercings. Again, because there was little difference between 16 and 28 winglet configurations, either number of winglets would be expected to produce similar results.

It is important to realize that the data reported in this thesis only considers tube wall heat transfer. The effect winglets and piercings had on other surfaces in the heat exchanger were not considered. Vortices formed in louvered fin heat exchangers will not only contact the tube wall, but will also sweep over other surfaces effecting heat transfer coefficients. Also, piercings in the louvered fins decrease the area available for conduction from the tube wall through the louvered

fins, possibly causing a significant decrease in louver heat transfer. The optimal winglet configuration that maximizes overall heat transfer may therefore not be the configuration that induces the largest tube wall heat transfer. At this point, winglets have been shown to be a promising method of improving overall heat transfer efficiency in louvered fin heat exchangers. For a final determination to be made on the most advantageous winglet and piercing configuration, the impact of louvered fin alterations on other heat exchanger surfaces must be considered.

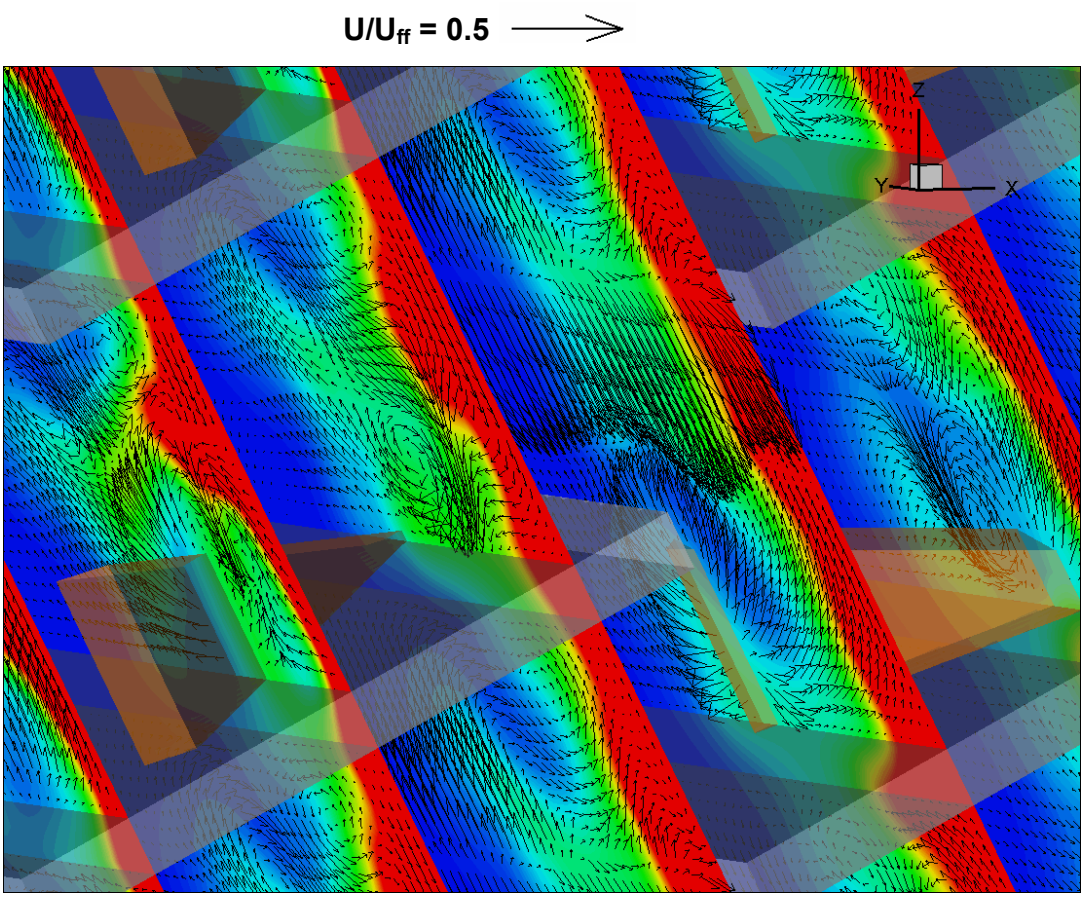

Figure D1. Secondary flow vectors for the two-dimensional louvered fin case with a winglet angled away from the tube wall. The winglet can be seen forming a vortex, but the vortex breaks as it encounters the next louver in the streamwise direction. Flow is from left to right aligned with the louvers.

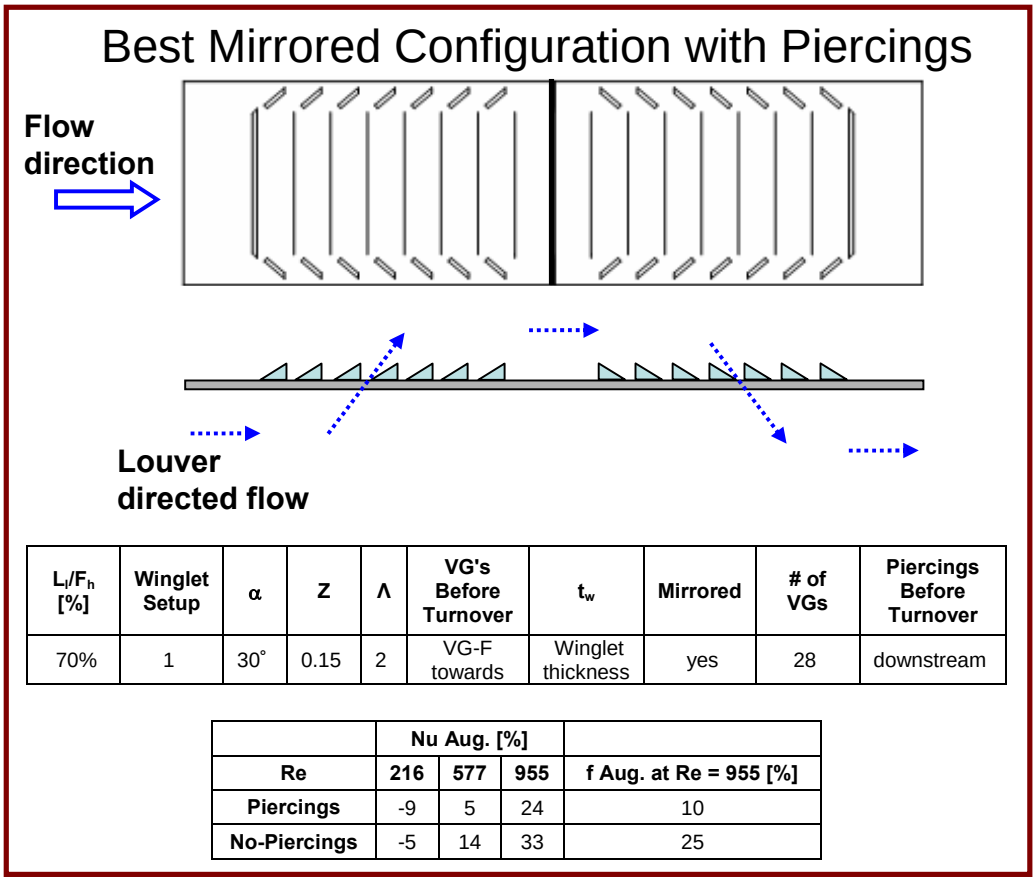

L_l/F_h [%]	Winglet Setup	α	Z	Λ	VG's Before Turnover	t_w	Mirrored	# of VGs	Piercings Before Turnover
70%	1	30°	0.15	2	VG-F towards	Winglet thickness	yes	28	downstream

	Nu Aug. [%]			
Re	**216**	**577**	**955**	**f Aug. at Re = 955 [%]**
Piercings	-9	5	24	10
No-Piercings	-5	14	33	25

Figure D2. Best mirrored pierced louvered fin winglet configuration tested using the three-dimensional louvered fins.

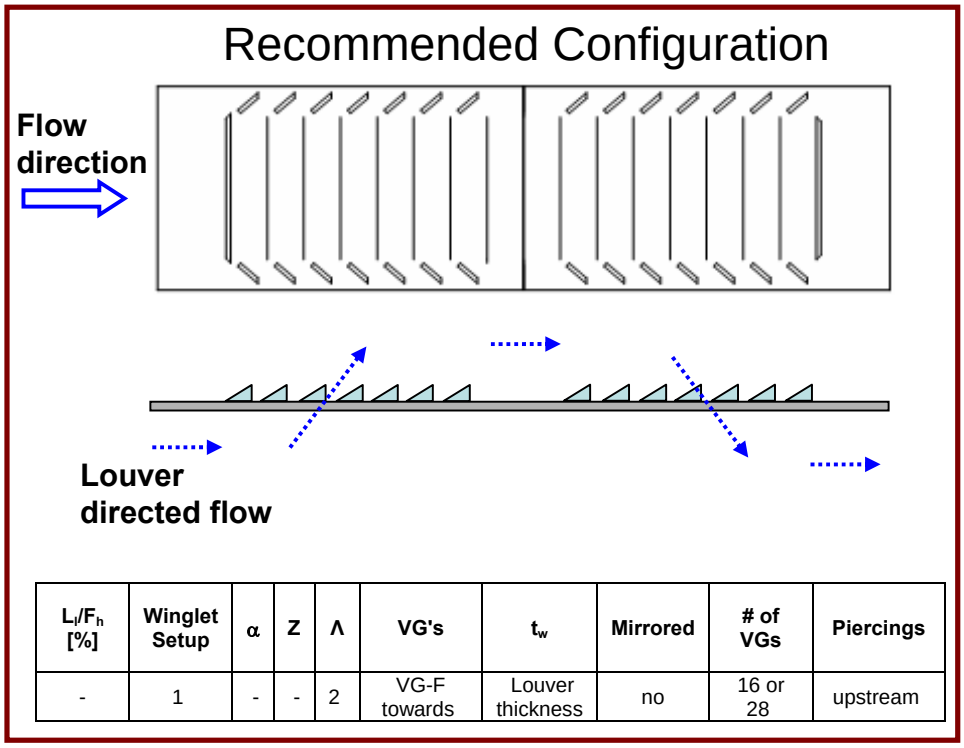

L_l/F_h [%]	Winglet Setup	α	Z	Λ	VG's	t_w	Mirrored	# of VGs	Piercings
-	1	-	-	2	VG-F towards	Louver thickness	no	16 or 28	upstream

FigureD3. Recommended non-mirrored pierced louvered fin winglet configuration to augment heat transfer using the three-dimensional louvered fins.

Appendix E

References

[E.1] Sanders P., 2005, "Effects of Louver Length and Vortex Generators to Augment Tube Wall Heat Transfer in Louvered Fin Heat Exchangers," MSME Thesis, Virginia Tech.

[E.2] Lyman, A. C., Stephan, R. A., Thole, K. A., Zhang, L., Memory, S., 2002, "Scaling of Heat Transfer Coefficients Along Louvered Fins," *Experimental Thermal Fluid Science*, vol. 26, pp. 547-563.

[E.3] Stephan, R. A. and Thole, K. A., 2005, "Optimization Study Relevant to Louvered Fin Heat Exchangers," *International Journal of Heat Exchangers*, vol. 6, pp. 73-92.

[E.4] Ebeling, P. and Thole, K. A., 2004, "Measurements and Predictions of the Heat Transfer at the Tube-Fin Junction for Louvered Fin Heat Exchangers," *International Journal of Compact Heat Exchangers*, vol. 5, pp. 265-286.

[E.5] Sanders, P. and Thole, K. A., 2006, "Effects of Winglets to Augment Tube Wall Heat Transfer in Louvered Fin Heat Exchangers," *International Journal of Heat and Mass Transfer*, (in press).

[E.6] Lyman, A., 2000, "Spatially Resolved Heat Transfer Studies in Louvered Fins for Compact Heat Exchangers," MSME Thesis, Virginia Tech.

[E.7] Modest, M. F., *Radiative Heat Transfer*, 2nd ed., Academic Press, New York, 2003.

[E.8] White, F. M., *Fluid Mechanics*, 4th ed., McGraw-Hill, New York, 1999.